Effect of Full-Chord Porosity on Aerodynamic Characteristics of the NACA 0012 Airfoil

Raymond E. Mineck
Langley Research Center • Hampton, Virginia

Peter M. Hartwich
ViGYAN Inc. • Hampton, Virginia

Summary

A wind tunnel test was conducted on a two-dimensional model of the NACA 0012 airfoil section with either a conventional solid upper surface or a porous upper surface with a cavity beneath for passive venting. The purposes of the test were to investigate the aerodynamic characteristics of an airfoil with full-chord porosity and to assess the ability of porosity to provide a multipoint or self-adaptive design. The tests were conducted in the Langley 8-Foot Transonic Pressure Tunnel over a Mach number range from 0.50 to 0.82 at chord Reynolds numbers of 2×10^6, 4×10^6, and 6×10^6. The angle of attack was varied from $-1°$ to $6°$ in $1°$ increments. The porous surface nominally extended over the entire upper surface. The porosity was zero at the leading and the trailing edges and was distributed by using a square-root-sine function with a maximum value of 2.44 percent at the model midchord. The average porosity (ratio of total hole area to total porous surface area) of the upper surface was 1.08 percent.

In general, full-chord porosity reduces the lift curve slope and increases the drag at a given section normal force coefficient. At lower Mach numbers, porosity leads to a dependence of the drag on the normal force. At subcritical conditions, porosity tends to flatten the pressure distribution, which reduces the suction peak near the leading edge and increases the suction over the middle of the chord. At supercritical conditions, the compression region on the porous upper surface is spread over a longer portion of the chord. In all cases, the pressure coefficient in the cavity beneath the porous surface is fairly constant with a very small increase over the rear portion. For the porous upper surface, the trailing edge pressure coefficients exhibit a creep at the lower section normal force coefficients, which suggests that the boundary layer on the rear of the airfoil is significantly thickening with increasing normal force coefficient. Porous airfoils exhibit an adaptive characteristic in that the thickness and the leading edge radius of an equivalent solid airfoil decrease with increasing Mach number, thus making the porous NACA 0012 airfoil perform more like a high-speed airfoil.

Introduction

For supercritical flow over a solid surface airfoil, the supersonic zone may be terminated by a strong normal shock. In addition to causing wave drag, the pressure rise across the shock may lead to boundary layer separation, which further increases the total drag. Narrow porous surface strips with cavities beneath the surface of transonic airfoils have been proposed to delay the drag rise that is associated with the energy losses due to shocks and shock-induced boundary layer separation (refs. 1 to 6). The principle underlying this passive drag reduction technique, often referred to as shock venting, is presented in figure 1(a).

By placing a porous strip on the surface over a cavity beneath the foot of the shock, a secondary flow is induced into and out of the cavity. The velocities through the surface and the velocities in the cavity are relatively small by design. Since the velocity of the flow in the cavity is small, the pressure gradient in the cavity is also small. The pressure level in the cavity can be considered nearly constant with a value between the minimum and the maximum pressures on the porous surface. The pressure rise associated with the shock above the porous surface creates a chordwise pressure gradient. Aft of the shock, the pressure on the porous surface is greater than the pressure in the cavity, so the secondary flow goes into the cavity. The secondary flow travels upstream in the cavity and exits through the porous surface upstream of the shock, where the pressure on the porous surface is less than that in the cavity. This secondary flow proceeds downstream over the porous surface. The resulting bubble of recirculating flow acts like a bump on the airfoil surface, which leads to an oblique compression wave (which can be isentropic) that forms the upstream edge of a lambda shock. To be effective, the porous strip must be located beneath the shock for the operating Mach number and lift coefficient.

Flow visualization studies (refs. 1 and 2) show that a porous strip placed beneath a shock does lead to a weaker lambda shock system. Data from exploratory experiments (refs. 1 to 3) indicate that, at supercritical conditions with a strong shock, a narrow porous strip reduces the drag, may increase the lift, and increases the buffet boundary. At subcritical conditions, the porous strip increases the drag (ref. 1).

Computational studies of solutions to the full potential flow, the Euler, and even the Navier-Stokes equations have simulated the flow over an airfoil with a porous strip (refs. 4 to 7). Calculated results agree with the experimental data in that a porous strip can increase the lift and reduce the wave drag. The results also show the formation of the lambda shock system over the porous strip. Calculations with viscous effects show that a porous strip can suppress transonic shock-induced oscillations causing buffet (ref. 7). When the addition of a porous strip leads to more negative pressure coefficients on surfaces with downstream-directed, outward normal vectors, the calculated pressure drag will increase. Viscous calculations indicate that porosity can lead to a separated flow region downstream of the porous strip and to an increase in the viscous drag. Increases in the pressure and the viscous drag offset to some degree the reduction of the wave drag. As a result, the net drag

increases when there is either a weak shock or no shock and the net drag decreases when there is a strong shock.

A pressure gradient along the length of a porous surface creates a secondary flow field that acts like a bump or a local increase in thickness. By locating a porous strip on the forward portion of the airfoil, the increase in local thickness can increase the effective leading edge radius and can improve the performance of the airfoil at high incidence angles, which produces a self-adaptive airfoil (ref. 8). Results from an Euler study (ref. 9) show that porosity that covers almost the entire chord (fig. 1(b)) not only delays the drag divergence, but also produces surface pressure distributions, which suggest that full-chord porosity might provide a means for achieving multipoint design for transonic airfoils.

The purpose of this report is to present experimental surface static pressure and wake total pressure distributions so that the effect of full-chord porosity on airfoil aerodynamic characteristics is better understood. The results are also used to determine whether the delay in drag divergence and the multipoint design capability predicted in the Euler study reported in reference 9 can be achieved. The experimental study presented herein was conducted in the Langley 8-Foot Transonic Pressure Tunnel (ref. 10) with a two-dimensional model that incorporated the NACA 0012 airfoil section.

Two upper surfaces were tested: one with full-chord porosity and the other with no porosity (solid surface). The lower surface of the model was solid. Measurements were obtained over a Mach number range from 0.50 to 0.82, an angle-of-attack range from $-1°$ to $6°$, and chord Reynolds numbers of 2×10^6, 4×10^6, and 6×10^6. Chordwise static pressure distributions were measured on the upper and the lower exterior surfaces of the airfoil and along the bottom of the cavity. Total pressure distributions were measured across the airfoil wake. These pressure data, as well as the integrated force and moment coefficients, are used to study the effect of porosity on the airfoil aerodynamic characteristics. Equivalent solid airfoils were defined by an inverse design method and the porous upper surface pressure distributions to assess any multipoint design characteristics in the porous airfoil results.

Symbols

The results are presented in coefficient form with the moment reference center at the quarter-chord. All experimental measurements and calculations were made in U.S. customary units.

b	model span, 83.9 in.
C_p	pressure coefficient
$C_{p,te}$	pressure coefficient near the trailing edge ($x/c = 0.99$)
C_p^*	pressure coefficient at local sonic conditions
c	model chord, 25.00 in.
c_d	section drag coefficient
c_m	section pitching moment coefficient resolved about the quarter-chord
c_n	section normal force coefficient
M_∞	free-stream Mach number
p_t	local total pressure in wake, psi
$p_{t,\infty}$	free-stream total pressure, psi
R_c	Reynolds number based on model chord and free-stream conditions
r_{le}	airfoil leading edge radius, in.
t_{max}	airfoil maximum thickness, in.
x	chordwise distance from the leading edge, positive downstream, in.
y	normal distance from the chord line or rake tube location, positive up, in.
z	spanwise distance, positive out the right wing, in.
α	angle of attack, positive leading edge up, deg
Δy	measured normal distance $-$ design normal distance from the chord line, in.
η	nondimensional spanwise location, $\dfrac{z}{b/2}$
σ	surface permeability parameter

Subscript:

max	maximum value

Wind Tunnel

The investigation was conducted in the Langley 8-Foot Transonic Pressure Tunnel (8-ft TPT). Information about the wind tunnel may be found in reference 10. The tunnel is a single-return, fan-driven, continuous-operation pressure tunnel. The top and the bottom walls are slotted and the sidewalls are solid. The test section is 160 in. long with an 85.5-in-square cross section at the beginning of the slots. The cross-sectional area of the test section is equivalent to the cross-sectional area of an 8-ft-diameter circle. A photograph of an airfoil model installed in the test section is presented in figure 2(a). The empty test section Mach number is continuously variable from about 0.20 to 1.30. Stagnation pressure can be varied from 0.25 atm to 2.00 atm. Air dryers are used to control the dew point. A heat exchanger located upstream of the settling chamber controls the stagnation temperature. Five turbulence reduction screens are

located just downstream of the heat exchanger. An arc-sector model support system with an angle range from −12.5° to 12.5° is located in the high-speed diffuser. For this test, a wake rake was installed on the model support system. The whole arc sector was translated longitudinally to position the wake rake at the desired test section station.

Model

An unswept, two-dimensional airfoil model was used for this investigation. Photographs of the model are presented in figure 2 and sketches are presented in figure 3. The model spanned the width of the tunnel at a vertical station 1.4 in. above the tunnel centerline. The model chord was 25.00 in., which yields an aspect ratio of 3.36 and a ratio of tunnel height to model chord of 3.42. The angle of attack was set manually by rotating the model about pivots in the angle-of-attack plates mounted on the tunnel sidewalls. (See figs. 2(a) and 3(a).) Fixed pivot settings provided an angle-of-attack range from −1.00° to 6.00° in increments of 0.25°; however, only 1° increments were used.

The model was fabricated in two parts: a main spar and an interchangeable center insert. (See figs. 3(a) and 3(b).) The upper and the lower surfaces of the outer portions of the main spar were solid and followed the contour of the NACA 0012 airfoil section. The center portion of the main spar was also solid and the lower surface followed the contour of the NACA 0012 airfoil. The interchangeable insert, installed over the center portion of the main spar, defined the leading and the trailing edges of the lower surface, as well as the entire upper surface of the center portion of the wing. (See fig. 3(b).) The upper surface of the interchangeable insert was porous and the lower surface was solid. The model shape was measured at three spanwise stations and the deviation of the measured airfoil shape from the desired shape is presented in figure 4. The solid lower surface was very close to the desired contour, with the maximum deviation less than $0.0002c$. The porous upper surface, with a maximum deviation of $0.0009c$, did not follow the desired contour as closely as the lower surface.

The interchangeable center insert was machined with 46 chordwise cavities, each 0.94 in. wide and spaced at 1.00 in. intervals. (See figs. 3(b) and 3(c).) The remaining 0.06 in. between the cavities formed ribs to support the porous surface. The maximum cavity depth of 0.75 in. was maintained from near the nose to the $0.5c$ location. The depth decreased linearly from that location to zero at the trailing edge.

The porous surface was a perforated titanium sheet, 0.020 in. thick. (See figs. 2(b) and 3(c).) The porous sheet had 368 chordwise rows with 440 holes in each row. The holes were laser drilled with a diameter of $0.010 \pm .001$ in. The porous sheet was bonded to the ribs with epoxy resin. Near the trailing edge, where the cavity was shallow, the perforated plate was bonded to the solid lower surface, which eliminated the porosity there. The chordwise rows were spaced 0.125 in. apart so that there were 8 rows over each cavity. The chordwise distribution of the porosity is defined by

$$\sigma = \sigma_{max}\sqrt{\sin(\pi\,x/c)} \tag{1}$$

This distribution and the value $\sigma_{max} = 0.6$ were selected to be consistent with the Euler study of reference 9. This distribution was implemented by varying the spacing of the holes along the length of the chord. Determination of the chordwise spacing of the holes is presented in the appendix. The average porosity (ratio of total hole area to total porous surface area) was 1.08 percent and the peak porosity was 2.44 percent.

A single chordwise row of pressure orifices was installed on the upper surface and the lower surface near the model centerline. Two spanwise rows of pressure orifices were installed on the upper surface and the lower surface. A single chordwise row was installed on the bottom of the cavity just to the right of the model centerline. A sketch of the locations of the pressure orifices is presented in figure 3(a) and a listing is presented in table 1. The orifices were installed normal to the local surface and had a diameter of 0.020 in. For the chordwise row, the upper surface orifices were located on the centerline (except for the two orifices at $x/c = 0$ and $x/c = 0.0029$). The lower surface orifices were located 1.5 in. to the right of the centerline. There were 49 orifices on the upper surface that extended from the leading edge back to $0.99c$ and 47 orifices on the lower surface that extended from $0.0068c$ back to $0.99c$. The orifices were concentrated near the leading edge. In the cavity, the orifices were located along the center of the cavity bottom, 0.5 in. from the model centerline. (See fig. 3(c).) There were 13 cavity orifices that extended from $0.033c$ to $0.923c$ and spaced at approximately $0.07c$ intervals. The two spanwise rows on each surface were located at $0.80c$ and $0.90c$.

Wake Rake

A wake rake was mounted vertically on the model support system to survey the total and the static pressure distributions in the model wake on the tunnel centerline. The rake was pitched on the model support system to align the maximum total pressure loss with the rake centerline. Except where noted otherwise, the wake rake streamwise location was fixed at 37.50 in. downstream of the model trailing edge. A sketch of the wake rake is presented in figure 5 and a photograph is presented in

figure 6. The rake tube locations are listed in table 2. The wake rake had 61 total pressure tubes located between 17.685 in. above and 17.685 in. below the rake center-line. The inside of each total pressure tube was flattened into an oval shape 0.02 in. high and 0.07 in. wide. The tubes were concentrated near the center of the rake where the total pressure gradient was expected to be the largest. In addition, there were 7 static pressure probes installed between 10.015 in. above and 10.015 in. below the rake centerline in a vertical plane 0.50 in. from the plane of the rake total pressure tubes.

Instrumentation

The test section total and static pressures were mea-sured with quartz Bourdon tube differential pressure transducers referenced to a vacuum. Each transducer had a range from ±30 psid and a quoted accuracy from the manufacturer of ±0.003 psid. The test section stagnation temperature was measured with a thermocouple mounted in the settling chamber. The wing static pressures and the wake rake static and total pressures were measured with an electronically scanned pressure measurement system with a transducer dedicated to each orifice. Each trans-ducer had a range of ±5 psid and a quoted accuracy from the manufacturer of ±0.005 psid. The model angle of attack was determined by a pinhole selected to fix the model attitude on the angle-of-attack plates.

Tests and Procedures

The model angle of attack was set manually. The angles used for this test ranged from −1° to 6° in 1° increments. At each angle of attack, the free-stream Mach number was varied from 0.50 to 0.82 at Reynolds numbers of 2×10^6, 4×10^6, and 6×10^6 based on a model chord of 25.00 in. The nominal test conditions are presented in table 3. All tests were conducted at a stagna-tion temperature of 100°F. At each test condition, the model support system (and consequently the wake rake) angle was adjusted so that the location of the maximum loss in total pressure coincided with the center tube of the wake rake. This ensured that the portion of the wake with the largest total pressure gradient was measured by that portion of the rake with the closest total pressure tube spacing. Normally, the total pressure tubes on the wake rake were positioned $1.5c$ (37.5 in.) downstream of the model trailing edge at an angle of attack of 0°. A limited number of measurements were obtained with the wake rake positioned $1.0c$ (25.0 in.) downstream of the model. A comparison of the results obtained with the wake rake at these two locations, presented in figure 7, shows no significant effects from the wake rake location on the integrated force and moment coefficients.

Boundary layer transition was fixed for all tests with a 0.1-in.-wide strip of number 80 carborundum grit on both the upper and the lower surfaces. The strip on each surface began 1.25 in. back ($x/c = 0.05$) from the leading edge. The grit size was determined by using the tech-nique described in reference 11.

The section normal force and pitching moment coef-ficients were obtained by numerically integrating (with the trapezoidal method) the local pressure coefficient at each orifice multiplied by an area weighting function. (The area weighting function is determined by the loca-tion of the surface pressure orifices.) The section drag coefficient was obtained by numerically integrating (with the trapezoidal method) the point drag coefficient calcu-lated at each rake total pressure tube by using the proce-dure of Baals and Mourhess (ref. 12).

No corrections were applied to the model angle of attack or to the free-stream Mach number for the effects of top and bottom wall interference or to the Mach num-ber for sidewall interference. Corrections to the porous airfoil results should be similar to the corrections to the solid airfoil results at similar test conditions. Therefore, comparisons of porous and solid airfoil results at similar test conditions should provide reasonable values for the effects of porosity.

A single porous insert with 0.75-in-deep cavities was tested. The solid surface results were obtained from the model with the porous insert covered with an impervious tape. The tape, which was 0.002 in. thick, covered the exterior of the model from the location of the transition strip on the lower surface, extending around the leading edge, and continuing back to the upper surface trailing edge. By using the same upper surface shape for both the solid and the porous surface tests, the effect of changes in the shape between the solid and the porous surface tests should be minimized.

Data Quality

As noted previously, the upper surface shape devi-ated slightly from the design shape. To evaluate the effect of the difference, the results from the current test are compared in figure 8 with results obtained previously on an NACA 0012 airfoil section in the 8-ft TPT (ref. 13). For the tests reported in reference 13, the Reynolds number was smaller and the grit size (number 54 carborundum grit) used to fix transition was larger than that used in the current test.

The comparison shows good agreement at a Mach number of 0.50 except for the angle of zero normal force coefficient and some small scatter in the drag data for the current test. These results suggest a model misalignment

of $-0.10°$ in the current test that could be due to flow angularity and/or the actual model attitude at $\alpha = 0°$. The difference between the section normal force coefficients is larger at a Mach number of 0.70, but the drag coefficients are in good agreement at normal force coefficients below the break in the drag polar. At a Mach number of 0.80, there is a sizable difference of 0.0020 in the drag coefficients at zero normal force.

Although there are differences between the results from the current test and those from the test reported in reference 13 because of the difference in the transition grit, Reynolds number, and surface shape, the current test is consistent (i.e., same transition grit, Reynolds number, and surface shape were used for the solid and the porous surface tests).

The porous upper surface extended from a non-dimensional spanwise location, $\eta = z/(b/2)$, of about $\eta = -0.6$ to $\eta = 0.6$. Since the flow over the central porous surface will be different from that over the outer solid surface, the spanwise extent of two-dimensional flow will be smaller for the porous surface than for the solid surface. The spanwise rows of pressure orifices were used to assess the extent of the two-dimensional flow.

The spanwise pressure distributions at $x/c = 0.8$ on the upper surface are presented in figure 9 at the lowest, an intermediate, and the highest test Mach numbers for both the solid and the porous upper surfaces. For the solid surface, there is no significant spanwise variation in the pressure coefficient at these three Mach numbers. For the porous surface, there is no significant spanwise variation at the lowest Mach number. At the intermediate and the highest Mach numbers, spanwise gradients develop at stations outboard of $\eta = 0.12$ and $\eta = -0.34$, which indicates the presence of three-dimensional flow for those test conditions. However, there is still a region with little spanwise pressure gradient around the model centerline so that there is a region of two-dimensional flow about the model centerline from the lowest to the highest test Mach numbers. Thus, the flow at the model centerline can be assumed to be two-dimensional for the conditions encountered in this test.

The model with the porous upper surface was retested at an angle of attack of $0°$ during the test and the results are presented in figure 10. Although there are only a limited number of repeat points, the data repeatability is excellent.

Presentation of Results

The results from this investigation are presented with transition fixed on both surfaces at $x/c = 0.05$. The moment reference center was $0.25c$. The results are presented in the following figures:

Discussion of Results

Airfoil Surface Pressure Distributions

Comparisons of the chordwise pressure coefficient distributions for the solid and the porous airfoils at the same angle of attack are presented in figures 11 to 19 for Mach numbers from 0.50 to 0.82 at a chord Reynolds number of 4×10^6 over the angle-of-attack range. It should be noted that, although the comparisons are presented at the same angle of attack, the section normal force and the drag coefficients are different. Thus, there may be small differences in the wall interference for the two points compared in each plot. For those cases with supersonic flow, the pressure coefficient for sonic flow is noted on the plot by C_p^*. No data were obtained for the solid upper surface airfoil model at an angle of attack of $-1°$. Assuming that the model is symmetric and that the tunnel upwash can be neglected, results from the lower surface of the solid airfoil at an angle of attack of $1°$ can be compared to the results from the upper surface of the porous airfoil at $-1°$. Therefore, results from the model with the solid surface at an angle of attack of $1°$ are plotted with the results from the porous surface at an angle of attack of $-1°$.

The pressure coefficient along the length of the cavity is, in general, fairly constant with a small positive gradient toward the rear part of the cavity for some cases. The constant pressure level indicates that the flow in the cavity is small, which validates the assumption of constant cavity pressure used in reference 9. The pressure coefficient in the cavity is about the same as the pressure coefficient on the upper surface just aft of the midchord location.

If the addition of porosity to the upper surface does not significantly change the pressure coefficient at the trailing edge, the flow along the lower surface should not be changed by the addition of porosity. This is indeed the case as shown by the measured chordwise pressure distributions. The lower surface pressure distribution is the same with and without upper surface porosity when there is no change in the trailing edge pressure coefficient. (See $\alpha = 2°$ in fig. 14.) However, if the addition of porosity reduces the pressure coefficient at the trailing edge, the change will be felt upstream on the lower surface since the pressure reduction will hinder the flow from approaching stagnation conditions at the trailing edge. The pressure coefficients on the lower surface are indeed reduced when porosity reduces the trailing edge pressure coefficient, which is an indication of a significantly thickened upper surface boundary layer and possible separation. (See $\alpha = 4°$ in fig. 14.)

For the solid airfoil at subcritical conditions, the flow accelerates over the forward portion of the upper surface, which creates a leading edge suction peak at higher angles of attack. Aft of the initial acceleration, the pressure coefficient increases. Over the forward portion of the porous airfoil, where the surface static pressure coefficient is less than the cavity pressure, flow will be drawn out of the cavity. Over the rear portion of the porous airfoil, where the surface pressure coefficient is greater, flow will be drawn into the cavity. This secondary flow through the porous surface tends to flatten (or reduce the gradient in) the upper surface chordwise pressure distribution over the midchord region. The leading edge suction peak (when present) is reduced, the suction over the forward portion of the airfoil is reduced, and the suction over the central portion of the airfoil is increased (e.g., compare pressure distributions with and without porosity for $\alpha = 5°$ in fig. 12).

For the solid airfoil at supercritical conditions, the accelerated flow region on the upper surface is terminated by a shock. For the porous airfoil, flow is drawn out of the cavity on the forward portion of the upper surface and forced into the cavity on the aft portion. The flow induced through the porous surface spreads the compression region over a longer portion of the chord, which replaces the sharp compression associated with a shock on the solid upper surface (e.g., see pressure distributions for $\alpha = 0°$ in fig. 18). The compression on the porous upper surface becomes steeper, suggesting the formation of a weak shock, as the angle of attack (and section normal force coefficient) increases (e.g., compare pressure gradients near $x/c = 0.20$ for $\alpha = 2°$ and $\alpha = 4°$ in fig. 18). However, this steepening is reduced when compared with that experienced by the shock on the solid surface airfoil, which results in a reduction of the wave drag portion of the total drag.

The effects of porosity on the chordwise surface pressure distributions at a nominal section normal force coefficient of 0.3 are presented in figure 20. For the subcritical case, the results are presented at the same angle of attack. Porosity reduces the leading edge suction peak on the upper surface, reduces the suction over the front of the upper surface, and increases the suction over the middle of the upper surface, which results in a redistribution of the pressure loading on the forward portion of the airfoil. There is only a little change in the lower surface pressure distributions. For the supercritical cases, the angle of attack for the model with the porous upper surface must be increased to match the section normal force coefficient. As the Mach number increases, the acceleration over the forward portion of the porous upper surface increases, sometimes exceeding the suction pressure coefficients for the solid upper surface. The compression region on the porous upper surface is spread over a longer portion of the chord. The compression does become steeper as the Mach number increases. For these

cases, the trailing edge pressure does not recover to the same level found for the solid upper surface. The lower surface pressure coefficient distributions over the forward portion of the chord differ because of the difference in the angles of attack and the change in the trailing edge pressure coefficient due to porosity.

As previously indicated, porosity affects the growth of the upper surface boundary layer, and consequently, affects the pressure coefficient near the trailing edge. A comparison of the pressure coefficients near the upper surface trailing edge (x/c = 0.99) is presented in figure 21. For the Mach numbers presented, the trailing edge pressure coefficient for the solid upper surface is relatively constant until trailing edge separation begins. With separation, the trailing edge pressure coefficient becomes less positive (more negative). For the porous upper surface, the trailing edge pressure coefficients exhibit a creep at the lower section normal force coefficients suggesting that the boundary layer on the rear portion of the airfoil is significantly thickening with increasing normal force coefficient. The trailing edge pressure coefficient for the porous surface also exhibits a rapid decrease at the higher normal force coefficients.

Wake Pressure Distributions

The shape of the total pressure profile in the airfoil wake can be used to assess the viscous and the wave drag contributions to the total drag. Comparisons of the wake total pressure ratio distributions for three angles of attack are presented in figure 22 for selected Mach numbers from 0.50 to 0.80 at a chord Reynolds number of 4×10^6. The profile below the peak total pressure loss is nearly the same for the solid and the porous surfaces. This profile is consistent with the similar lower surface chordwise pressure distributions found for the solid and the porous surfaces. At subcritical conditions, the peak total pressure loss and the thickness of the wake are larger for the porous surface. This difference indicates greater losses for the porous upper surface, probably due to increased viscous losses (increased skin friction) and losses associated with decelerating the flow into the cavity and accelerating the flow out of the cavity. Measurements at a Reynolds number of about 3×10^6 on a smooth solid and a smooth porous cylinder indicate that the skin friction for the porous wall is about 30 percent larger than that for the smooth wall (ref. 14). Thus, porosity significantly increases the viscous contribution to the total drag. At supercritical conditions, the wake profiles for the solid surface show an additional triangular region of total pressure loss from the upper surface associated with the wave drag due to the presence of shocks. Most of the wake profiles for the porous surface do not show the additional triangular region (e.g., see α = 2° in fig. 22(d)). Examination of the associated chordwise pressure distributions

(α = 2° in fig. 16) show a shock on the solid upper surface, but no shock on the porous upper surface. The chordwise pressure distributions and wake profiles associated with the porous surface for more extreme cases (higher angles of attack and Mach numbers) show that porosity does not always eliminate the shock or wave drag. (See α = 4° in figs. 18 and 22(e).) Porosity reduces the contribution of wave drag to the total drag.

Integrated Force and Moment Coefficients

Effect of Mach number. The effect of Mach number on the integrated force and moment coefficients for the airfoil with the solid upper surface and the porous upper surface is presented in figure 23. Results for the model with the solid upper surface (fig. 23(a)) follow the expected trends. For the lower Mach numbers, the drag coefficient is independent of the section normal force coefficient over the linear portion of the normal force curves. At transonic Mach numbers, increasing shock strength and wave drag with increasing normal force coefficient leads to increasing drag. The positive slope of the pitching moment coefficient curve indicates that the aerodynamic center is slightly forward of the moment reference center ($0.25c$). The slope of the section normal force curves increases with increasing Mach number. As the Mach number increases, the normal force curve becomes nonlinear at progressively smaller angles of attack.

Results for the model with the porous upper surface (fig. 23(b)) do not follow all of the same trends. As was found for the solid surface, at subcritical conditions, the normal force curve slope at zero normal force increases with increasing Mach number. Unlike the results for the solid surface, at the lower Mach numbers the drag coefficient for the porous surface increases with increasing normal force coefficient and increasing Mach number, which is a direct result of losses through the porous surface. At supercritical conditions, the normal force coefficient at an angle of attack of 0° becomes more negative with increasing Mach number.

Effect of Reynolds number. The effect of Reynolds number on the integrated force and moment coefficients for the model with the solid upper surface is presented in figure 24 and for the model with the porous upper surface in figure 25. The effect of Reynolds number on the porous surface is similar to that for the solid surface. Increasing the Reynolds number generally reduces the turbulent skin friction, and therefore, reduces the drag coefficient at a given normal force coefficient. It has little effect on the linear portion of the normal force or on the pitching moment curves.

Effect of porosity. The effect of porosity on the integrated force and moment coefficients is presented in figure 26. In general, upper surface porosity reduces the normal force curve slope and increases the drag at a given section normal force coefficient. The loss in normal force at a given angle of attack arises from the reduction in the pressure over the forward portion of the airfoil discussed previously. The increased drag arises from the increased viscous drag noted in the wake pressure distributions. At the lower Mach numbers, porosity leads to a dependence of the drag on the normal force. As the angle of attack and the normal force increase, the difference between the cavity pressure and the airfoil surface pressure increases and the flow through the porous surface increases. The chordwise component of this flow must be decelerated to zero and turned as the flow enters the cavity and accelerated and turned as the flow exits the cavity. The force required to decelerate and accelerate the flow increases the drag. Since the flow increases with normal force, the drag also increases with normal force. At supercritical conditions, the normal force curves for the airfoil with the porous upper surface develop a second, nearly linear segment (e.g., see $\alpha > 3°$ in fig. 26(e)). The start of this second segment appears to correlate with the formation of the localized steeper pressure gradient associated with the presence of a weak shock and wave drag noted in the discussion of the pressure distributions.

The effect of porosity on the variation of the section drag coefficient with the free-stream Mach number at two section normal force coefficients is presented in figure 27. For this study, drag divergence is defined as the point on the drag coefficient versus Mach number curve where $dc_d/dM_\infty = 0.1$. The solid surface exhibits a small amount of drag creep at subcritical Mach numbers with a dramatic increase at the transonic Mach numbers. The porous surface exhibits a higher level of drag, a higher drag creep, and a reduced drag divergence Mach number. For example at $c_n = 0$ and $M_\infty = 0.5$, the drag coefficient on the solid surface was 0.0085 and the drag coefficient on the porous surface was 0.0121. The Mach number associated with drag divergence decreased from about 0.78 for the solid surface to about 0.77 for the porous surface. Similarly at $c_n = 0.3$ and $M_\infty = 0.5$, the drag coefficient on the solid surface was 0.0086 and the drag coefficient on the porous surface was 0.0156. The Mach number associated with drag divergence decreased from about 0.74 for the solid surface to about 0.70 for the porous surface. For these conditions, the increased viscous losses, pressure drag, and momentum losses associated with the secondary flow into and out of the cavity arising from the porous surface are larger than the wave drag reduction from the porous surface.

Effective Airfoil Shape

The pressure distribution obtained from the airfoil with the porous upper surface could also be obtained from an equivalent solid airfoil with a different upper surface shape. The measured porous airfoil upper surface pressure distribution was used as input to the Direct Iterative Surface Curvature (DISC) method described in reference 15 coupled to the Euler solver described in reference 16 to obtain the new solid surface. Viscous effects were modeled with the boundary layer displacement thickness by using a modified theory of Stratford and Beavers (ref. 17). This particular combination of a design algorithm and a flow solver was experimentally verified in reference 18.

The airfoil design program should calculate the actual upper surface shape from the measured solid upper surface pressure distribution. A comparison of the baseline NACA 0012 airfoil upper surface shape with the resulting equivalent solid upper surface shape is presented in figure 28. The equivalent solid shapes are in good agreement with each other and with the NACA 0012 upper surface shape, thus validating the design process.

Next, the design program was used to generate equivalent solid upper surface shapes that correspond to the measured pressure distributions from the porous upper surface. Equivalent upper surface shapes with a closed trailing edge could not be generated for test conditions in which the upper surface trailing edge pressure coefficients indicated significant separation. These separated flows were beyond the capability of the flow solver with the attached-boundary-layer model.

A comparison of the equivalent solid upper surface shapes generated from the porous upper surface pressure distributions at constant angles of attack is presented in figure 29 for several Mach numbers. At the lowest Mach number, the addition of porosity at $\alpha = 0°$ leads to an airfoil that is thicker than the NACA 0012 airfoil section across the midchord region but has a reduced leading edge radius. The maximum airfoil thickness and the leading edge radius decrease as the Mach number increases at both of the angles of attack presented. The equivalent upper surface shape falls below that of the NACA 0012 over the forward portion of the chord at the higher Mach numbers. Porosity leads to a desirable self-adaptive feature of decreasing effective thickness with increasing Mach number. A comparison of the equivalent solid upper surface shapes generated from the porous upper surface pressure distributions at constant Mach numbers is presented in figure 30 for several angles of attack. At both Mach numbers presented, the maximum thickness and the leading edge radius decrease as the angle of

attack increases. Thus, porosity bestows a self-adaptive quality to the airfoil, albeit at a penalty of increased drag due to the venting losses.

Conclusions

A wind tunnel investigation was conducted on a two-dimensional airfoil model of an NACA 0012 airfoil section with a conventional solid upper surface and a porous upper surface. The purpose of the investigation was to study the effects of porosity on aerodynamic characteristics and to assess the ability of porosity to provide a multipoint or self-adaptive design. The tests were conducted in the Langley 8-Foot Transonic Pressure Tunnel over a Mach number range from 0.50 to 0.82 at chord Reynolds numbers of 2×10^6, 4×10^6, and 6×10^6. The angle of attack was varied from $-1°$ to $6°$. The porous surface nominally extended over the entire upper surface. When compared to the solid surface airfoil, the conclusions from this investigation are

1. At subcritical conditions, porosity tends to flatten the pressure distribution, which reduces the suction peak near the leading edge and increases the suction over the middle portion of the chord.

2. At supercritical conditions, the compression region on the porous upper surface is spread over a longer portion of the chord.

3. At supercritical conditions, for the porous upper surface, the trailing edge pressure coefficients exhibit a creep at the lower section normal force coefficients, which suggests that the boundary layer on the rear portion of the airfoil is significantly thickening with increasing normal force coefficient.

4. The pressure coefficient in the cavity is fairly constant with a very small increase over the rear portion, which indicates that the flow in the cavity is small.

5. Porosity reduces the lift curve slope and increases the drag at a given section normal force coefficient.

6. At the lower Mach numbers, porosity leads to a dependence of the drag on the normal force and the Mach number.

7. Porous airfoils exhibit an adaptive characteristic in that the thickness and the leading edge radius of an equivalent solid airfoil decrease with increasing Mach number, albeit at a penalty of increased drag.

NASA Langley Research Center
Hampton, VA 23681-0001
February 2, 1996

Appendix A

Determination of Chordwise Spacing of Holes on Porous Surface

Symbols

b	width of porous patch
D	hole diameter
l	length of porous patch
$\dot{m}$	mass flow rate
N	number of holes through porous patch
R	unit Reynolds number based on free-stream conditions
v_n	equivalent normal transpiration velocity
$\bar{v}$	average velocity through hole in porous surface
V_∞	free-stream velocity
Δp	pressure difference across porous surface
μ_∞	free-stream viscosity
ρ_∞	free-stream density
ρ	local density
σ	permeability parameter
σ_{max}	maximum value of permeability parameter
τ	thickness of porous surface

Determination of Spacing

The porous upper surface of the model was drilled with 368 chordwise rows of holes. The effect of the discrete regions of flow into and out of the cavity through this surface is modeled by an equivalent normal transpiration velocity. Darcy's law is used to relate the equivalent normal transpiration velocity to the pressure difference across the porous surface:

$$v_n = \frac{\sigma}{\rho_\infty V_\infty} \cdot \Delta p \qquad (A1)$$

The flow through an individual hole can be estimated with the Hagen-Poiseuille solution for fully developed, viscous flow through a circular pipe:

$$\bar{v} = \frac{D^2}{32\mu_\infty} \frac{\Delta p}{\tau} \qquad (A2)$$

If a porous patch of length l, width b, and N holes is selected, the mass flow through the N individual holes must equal the mass flow from the equivalent transpiration velocity over the patch of area $l \cdot b$. Assuming that the selected porous patch is small enough that the pressure difference can be assumed constant, the equivalence of the mass flow rates through the surface for the two representations can be expressed as

$$\dot{m} = \rho\bar{v}\frac{\pi D^2}{4}N = \rho v_n lb \qquad (A3)$$

Upon substituting the expressions for v_n from equation (A1) and the expression for $\bar{v}$ from equation (A2) into equation (A3), an expression is obtained that relates the geometric characteristics of the porous surface to the permeability:

$$\frac{\pi D^4}{128\mu_\infty}\frac{N}{\tau} = \frac{\sigma}{\rho_\infty V_\infty}lb \qquad (A4)$$

Substituting for the unit Reynolds number produces

$$\frac{\pi D^4}{128}\frac{RN}{\tau} = \sigma lb \qquad (A5)$$

For this study, the porous surface parameters were $\tau = 0.020$ in. and $D = 0.010$ in. The design was done at a unit Reynolds number R of 2×10^6/ft. A modified sine distribution was chosen for the surface permeability distribution:

$$\sigma = \sigma_{max}\sqrt{\sin(\pi x/c)} \qquad (A6)$$

For this study, $\sigma_{max} = 0.6$. The modified sine distribution and the value of σ_{max} were selected to be consistent with the computational study in reference 9.

The chordwise spacing of the holes can be determined by selecting a section of the porous surface that contains one hole ($N = 1$). Since there are 8 longitudinal rows per inch, the width of the section b would be 0.125 in. The length of the section l would be the unknown chordwise spacing. Solving equation (A5) for l and substituting the value of the surface permeability σ from equation (A6) for the desired chordwise location will yield the chordwise spacing at the selected chordwise location:

$$l = \frac{N\pi D^4 R}{128\tau b\sigma} \qquad (A7)$$

References

1. Bahi, L.; Ross, J. M.; and Nagamatsu, H. T.: Passive Shock Wave/Boundary Layer Control for Transonic Airfoil Drag Reduction. AIAA-83-0137, Jan. 1983.

2. Nagamatsu, H. T.; Trilling, T. W.; and Bossard, J. A.: Passive Drag Reduction on a Complete NACA 0012 Airfoil at Transonic Mach Numbers. AIAA-87-1263, June 1987.

3. Thiede, P.; Krogmann, P.; and Stanewsky, E.: Active and Passive Shock/Boundary Layer Interaction Control on Supercritical Airfoils. *Improvement of Aerodynamic Performance Through Boundary Layer Control and High Lift Systems*, AGARD CP-365, Aug 1984. (Available from DTIC as AD A147 396.)

4. Chen, C.-L.; Chow, C.-Y.; Holst, T. L.; and Van Dalsem, W. R.: Numerical Simulation of Transonic Flow Over Porous Airfoils. AIAA-85-5022, Oct. 1985.

5. Hsieh, Sheng-Jii; and Lee, Lung-Cheng: Numerical Simulation of Transonic Porous Airfoil Flows. *Proceedings of the Fifth International Symposium on Numerical Methods in Engineering—Volume 1,* R. Gruber, J. Periaux, R. P. Shaw, eds., 1990, pp. 601–608.

6. Chen, Chung-Lung; Chow, Chuen-Yen; Van Dalsem, William R.; and Holst, Terry L.: Computation of Viscous Transonic Flow Over Porous Airfoils. AIAA-87-0359, Jan. 1987.

7. Gillian, Mark A.: Computational Analysis of Drag Reduction and Buffet Alleviation in Viscous Transonic Flow Over Porous Airfoils. AIAA-93-3419, Aug. 1993.

8. Musat, Virgil M.: Permeable Airfoils in Incompressible Flow. *J. Aircr.*, vol. 30, no. 3, May 1992, pp. 419–421.

9. Hartwich, Peter M.: Euler Study on Porous Transonic Airfoils With a View Toward Multipoint Design. AIAA-91-3286, Sept. 1991.

10. Brooks, Cuyler W., Jr.; Harris, Charles D.; and Reagon, Patricia G.: *The NASA Langley 8-Foot Transonic Pressure Tunnel Calibration.* NASA TP-3437, 1994.

11. Braslow, A. L.; and Knox, E. C.: *Simplified Method for Determination of Critical Height of Distributed Roughness Particles for Boundary-Layer Transition at Mach Numbers From 0 to 5.* NACA TN-4363, 1958.

12. Baals, Donald D.; and Mourhess, Mary J.: *Numerical Evaluation of the Wake-Survey Equations for Subsonic Flow Including the Effect of Energy Addition.* NACA WR L-5 H27, 1945.

13. Harris, Charles D.: *Two-Dimensional Aerodynamic Characteristics of the NACA 0012 Airfoil in the Langley 8-Foot Transonic Pressure Tunnel.* NASA TM-81927, 1981.

14. Kong, Fred Y.; Schetz, Joseph A.; and Collier, Fayette: *Turbulent Boundary Layer Over Solid and Porous Surfaces With Small Roughness.* NASA CR-3612, 1982.

15. Campbell, Richard L.: *An Approach to Constrained Aerodynamic Design With Application to Airfoils.* NASA TP-3260, 1992.

16. Hartwich, Peter M.: Fresh Look at Floating Shock Fitting. *AIAA J.*, vol. 29, no. 7, July 1991, pp. 1084–1091.

17. Stratford, B. S.; and Beavers, G. S.: *The Calculation of the Compressible Turbulent Boundary Layer in an Arbitrary Pressure—A Correlation of Certain Previous Methods.* R. & M. No. 3207, British Aeronautical Research Council, 1961.

18. Mineck, Raymond E.; Campbell, Richard L.; and Allison, Dennis O.: *Application of Two Procedures for Dual-Point Design of Transonic Airfoils.* NASA TP-3466, 1994.

Table 1. Pressure Orifice Locations

(a) Chordwise rows

Upper surface x/c			Lower surface x/c			Cavity x/c
0.0001	0.3503	0.7200		0.3500	0.7200	0.033
0.0029	0.3802	0.7401		0.3799	0.7400	0.105
0.0062	0.4102	0.7601	0.0068	0.4099	0.7599	0.176
0.0133	0.4352	0.7801	0.0136	0.4349	0.7799	0.246
0.0212	0.4601	0.8001	0.0216	0.4600	0.8000	0.315
0.0305	0.4801	0.8200	0.0306	0.4800	0.8200	0.384
0.0404	0.5002	0.8400	0.0398	0.5000	0.8401	0.452
0.0604	0.5202	0.8600	0.0599	0.5199	0.8601	0.520
0.0804	0.5400	0.8800	0.0799	0.5399	0.8795	0.587
0.1004	0.5602	0.8998	0.1000	0.5600	0.9007	0.654
0.1252	0.5802	0.9201	0.1249	0.5801	0.9209	0.721
0.1504	0.6001	0.9399	0.1500	0.6000	0.9408	0.789
0.1803	0.6201	0.9598	0.1799	0.6200	0.9609	0.856
0.2153	0.6401	0.9746	0.2150	0.6400	0.9759	0.923
0.2502	0.6601	0.9899	0.2500	0.6600	0.9908	
0.2853	0.6801		0.2850	0.6800		
0.3202	0.6999		0.3200	0.7000		

(b) Spanwise rows

Upper surface η at—		Lower surface η at—	
$x/c = 0.8$	$x/c = 0.9$	$x/c = 0.8$	$x/c = 0.9$
−0.468	−0.456	−0.456	−0.456
−0.350	−0.340	−0.340	−0.340
−0.234	−0.222	−0.222	−0.222
−0.116	−0.106	−0.106	−0.106
0.116	0.106	0.106	0.106
0.234	0.222	0.222	0.222
0.350	0.340	0.340	0.340
0.468	0.456	0.456	0.456

Table 2. Wake Rake Pressure Tube Locations

(a) Total pressure tubes

		z, in.		
17.685	2.295	0.540	−0.540	−2.295
15.885	2.475	0.450	−0.630	−2.475
14.085	1.935	0.360	−0.720	−2.655
12.285	1.755	0.270	−0.810	−3.285
10.485	1.575	0.180	−0.900	−4.365
8.685	1.395	0.090	−1.035	−5.445
6.885	1.215	0.000	−1.215	−6.885
5.445	1.035	−0.090	−1.395	−8.685
4.365	0.900	−0.180	−1.575	−10.485
3.285	0.810	−0.270	−1.755	−12.285
2.655	0.720	−0.360	−1.935	−14.085
2.475	0.630	−0.450	−2.115	−15.885
				−17.685

(b) Static pressure tubes

z, in.
10.015
4.015
1.665
0.000
−1.665
−4.015
−10.015

Table 3. Nominal Test Conditions

	R_c		
M_∞	2×10^6	4×10^6	6×10^6
0.50	X	X	X
0.60	X	X	X
0.65	X	X	X
0.70	X	X	X
0.74		X	X
0.76		X	X
0.78		X	X
0.80		X	X
0.82		X	X
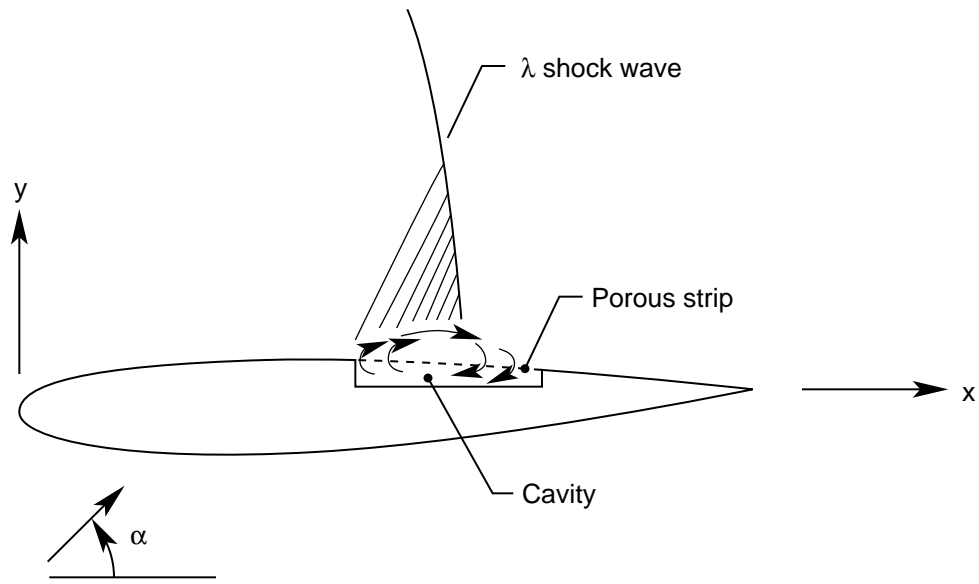
(a) Narrow porous strip for shock venting.
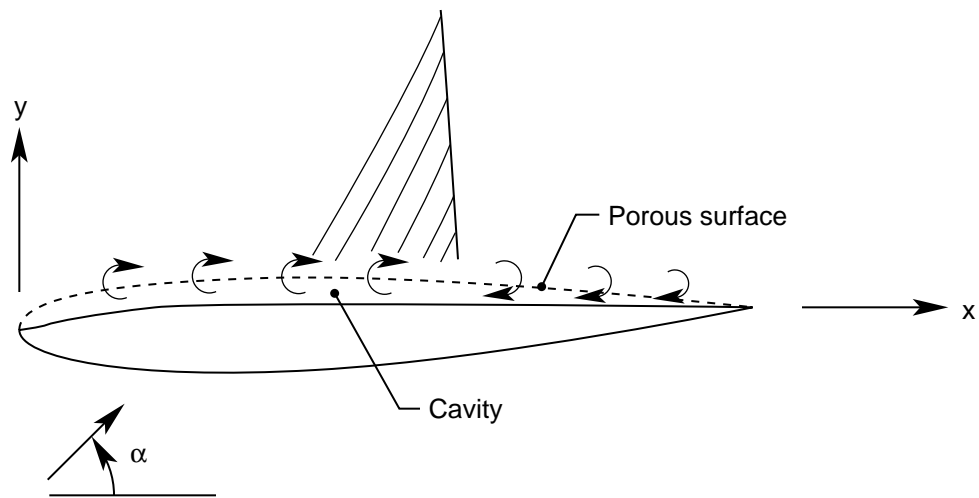
(b) Full chord porous upper surface.

Figure 1. Airfoil with porous surface in transonic flow.

Labels on figure:
- Wake rake
- Angle-of-attack plate
- Main spar
- Porous insert
- Flow
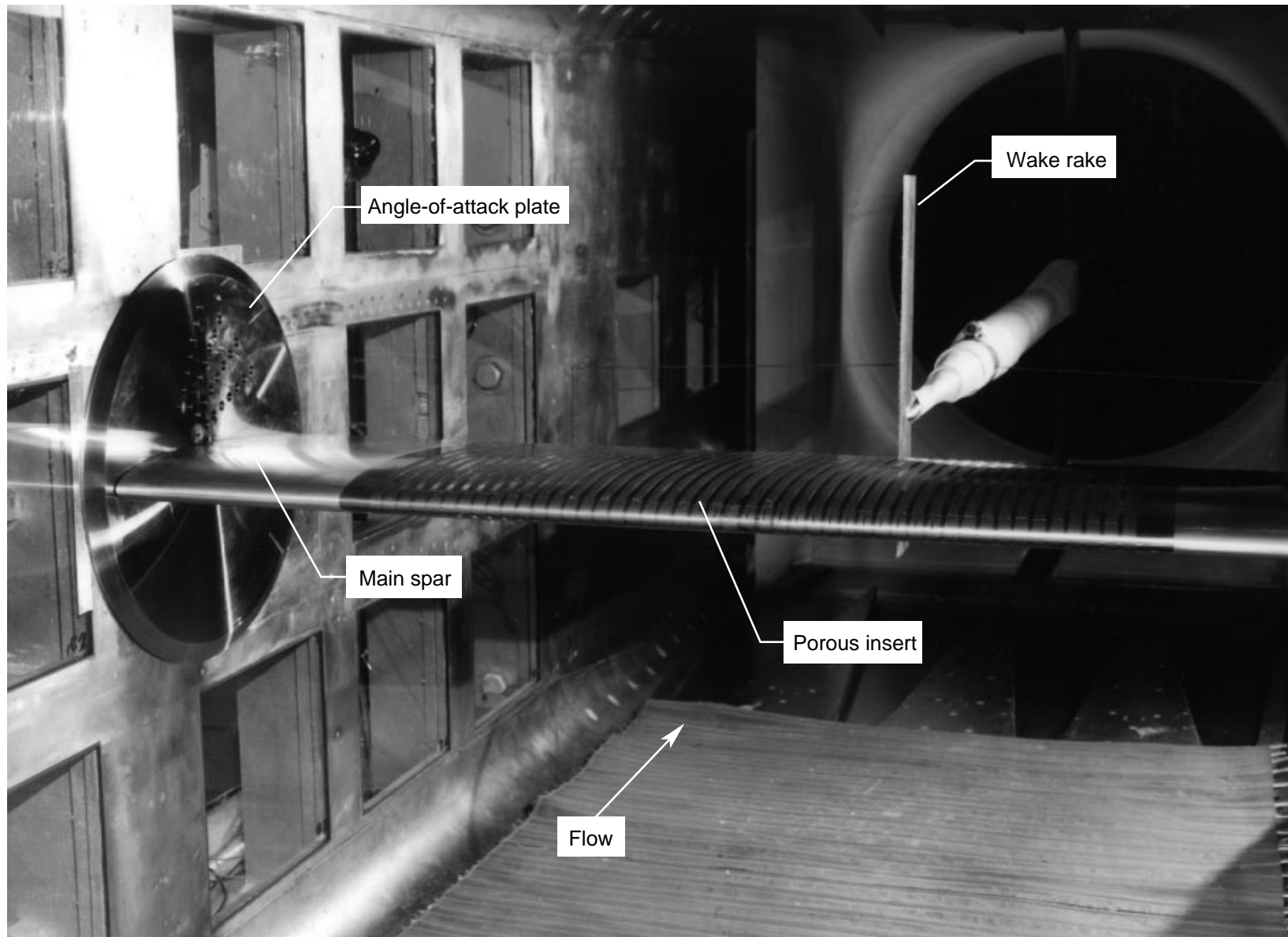
L-93-00490

(a) Model installation.

Figure 2. Photographs of model in 8-ft TPT.

Flow
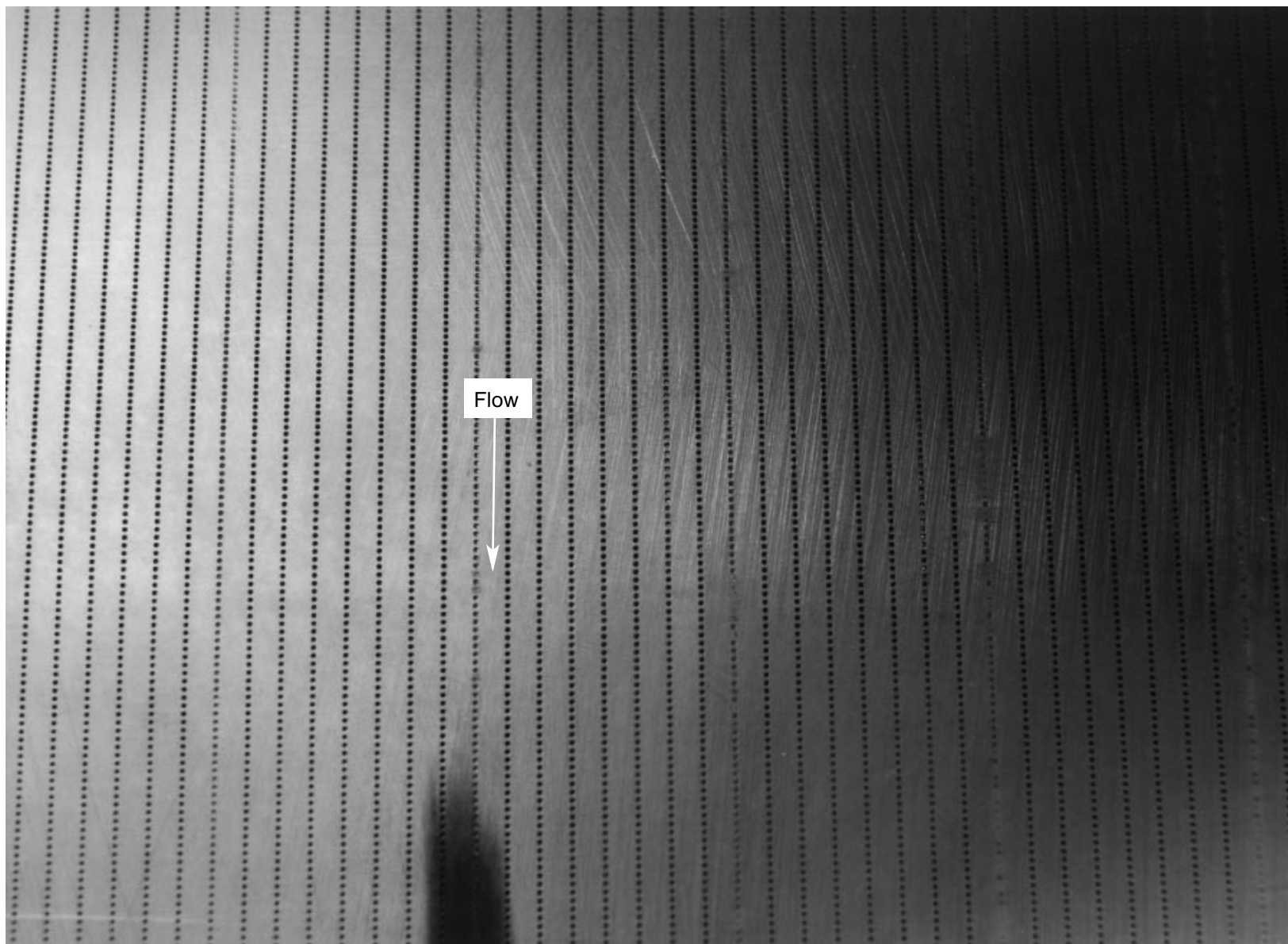
L-93-00491

(b) Close-up of porous surface.

Figure 2. Concluded.
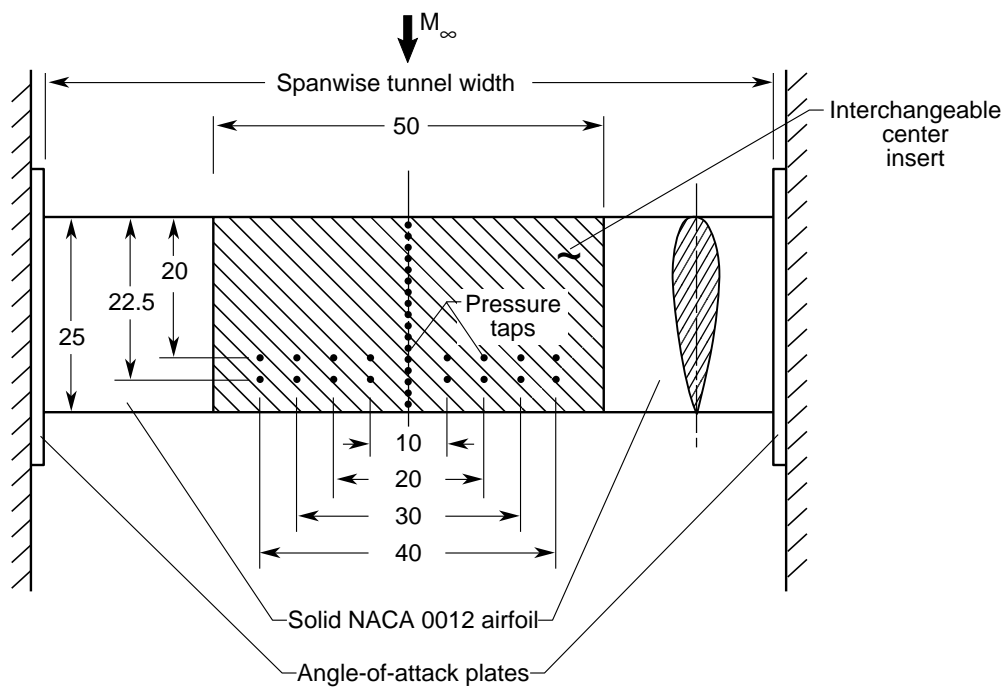
(a) Top view of model.
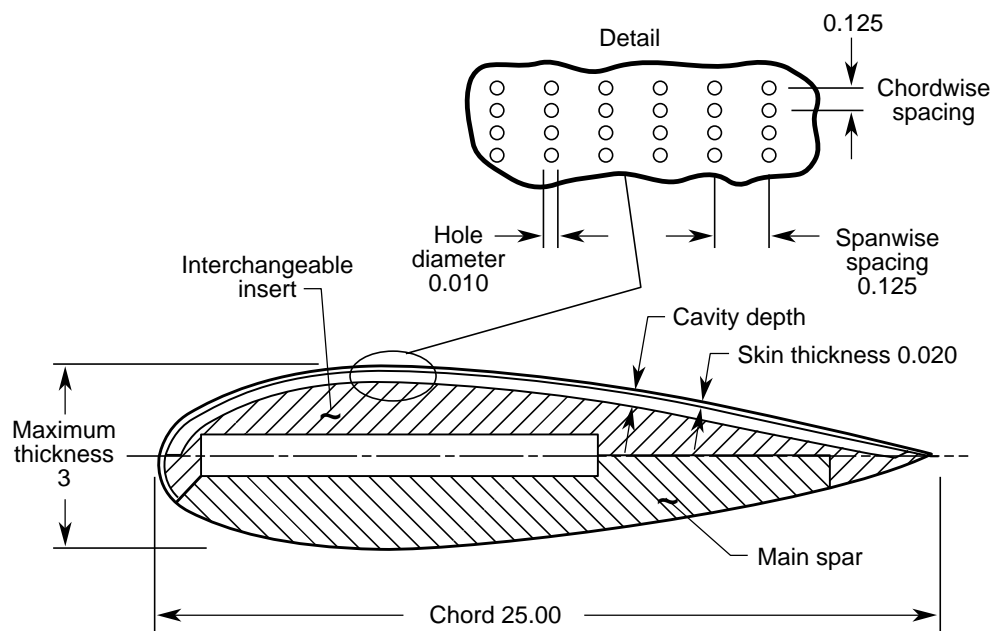
(b) Cross section of model.

Figure 3. Details of model. All dimensions are in inches.
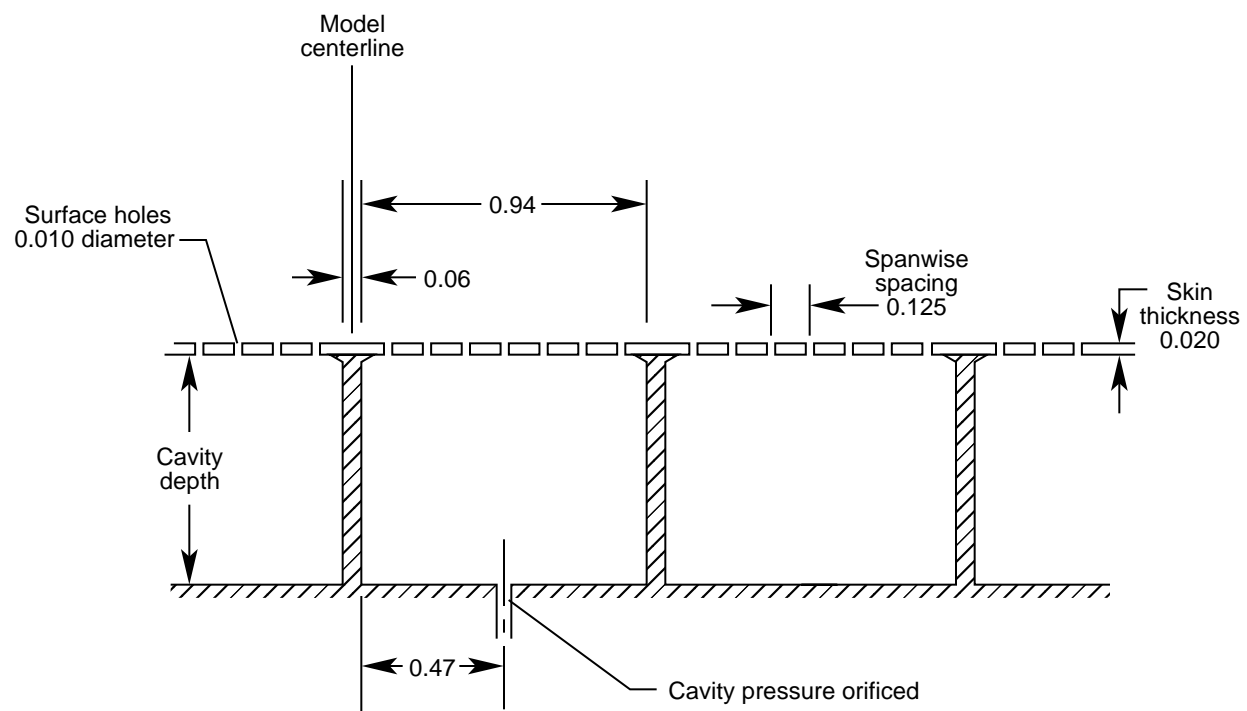
(c) Cross section of cavities.

Figure 3. Concluded.
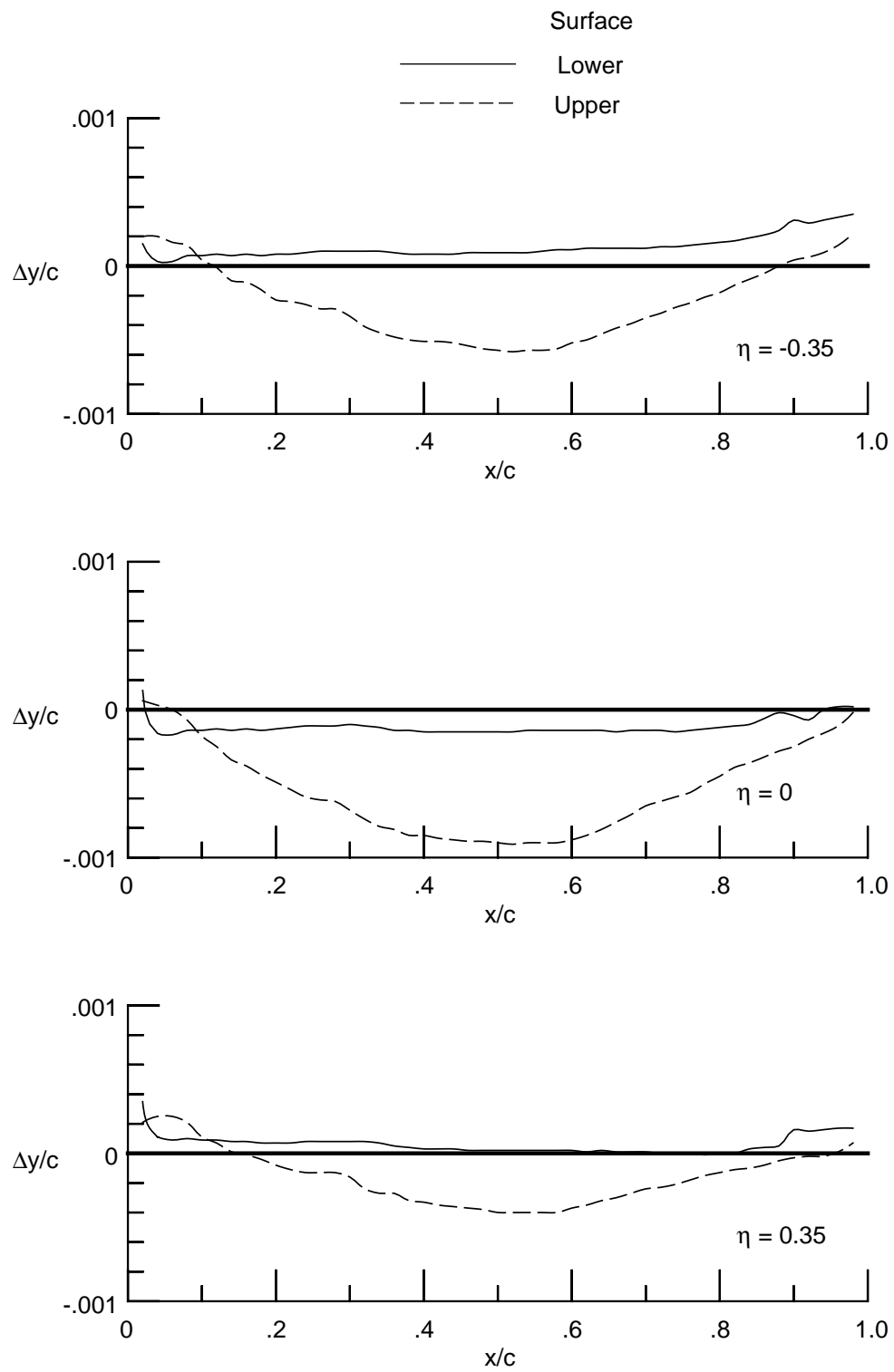
Figure 4. Deviation of model shape from design NACA 0012 shape.
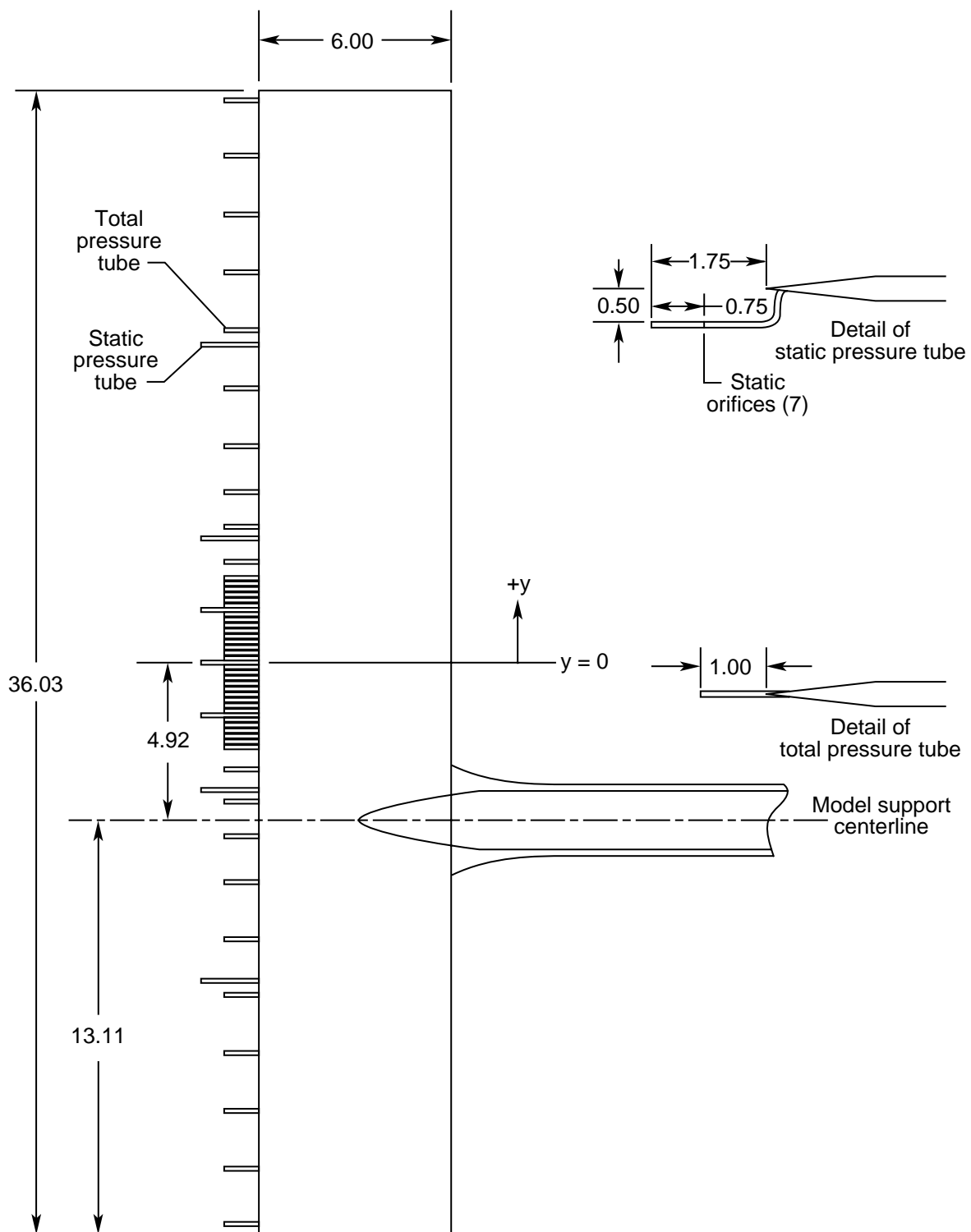
Figure 5. Details of wake rake. All dimensions in inches.
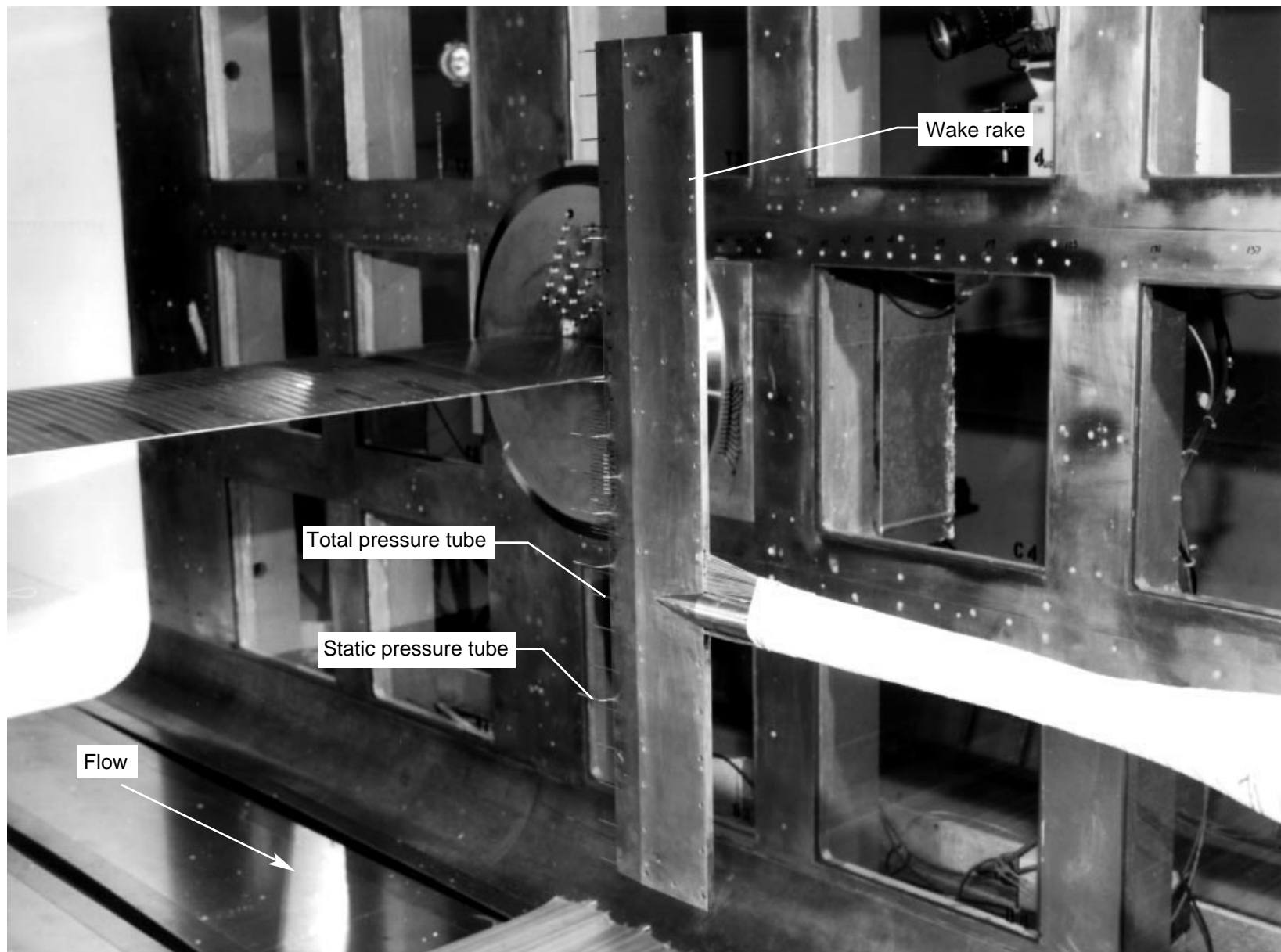
Figure 6. Photograph of wake rake in 8-ft TPT.

L-93-00493
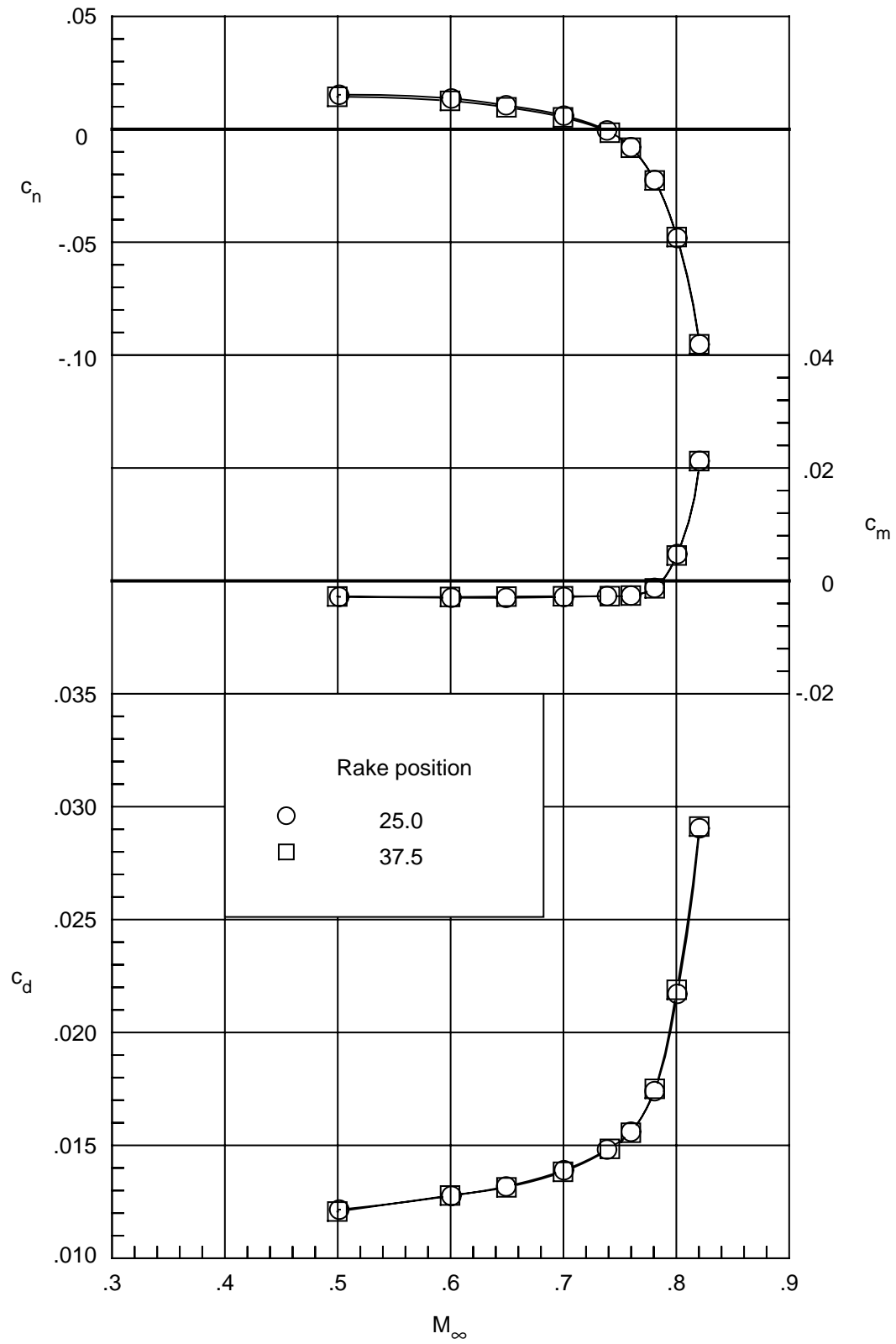
(a) $R_c = 4 \times 10^6$.

Figure 7. Effect of rake position on integrated force and moment coefficients of baseline porous airfoil. $\alpha = 0°$.
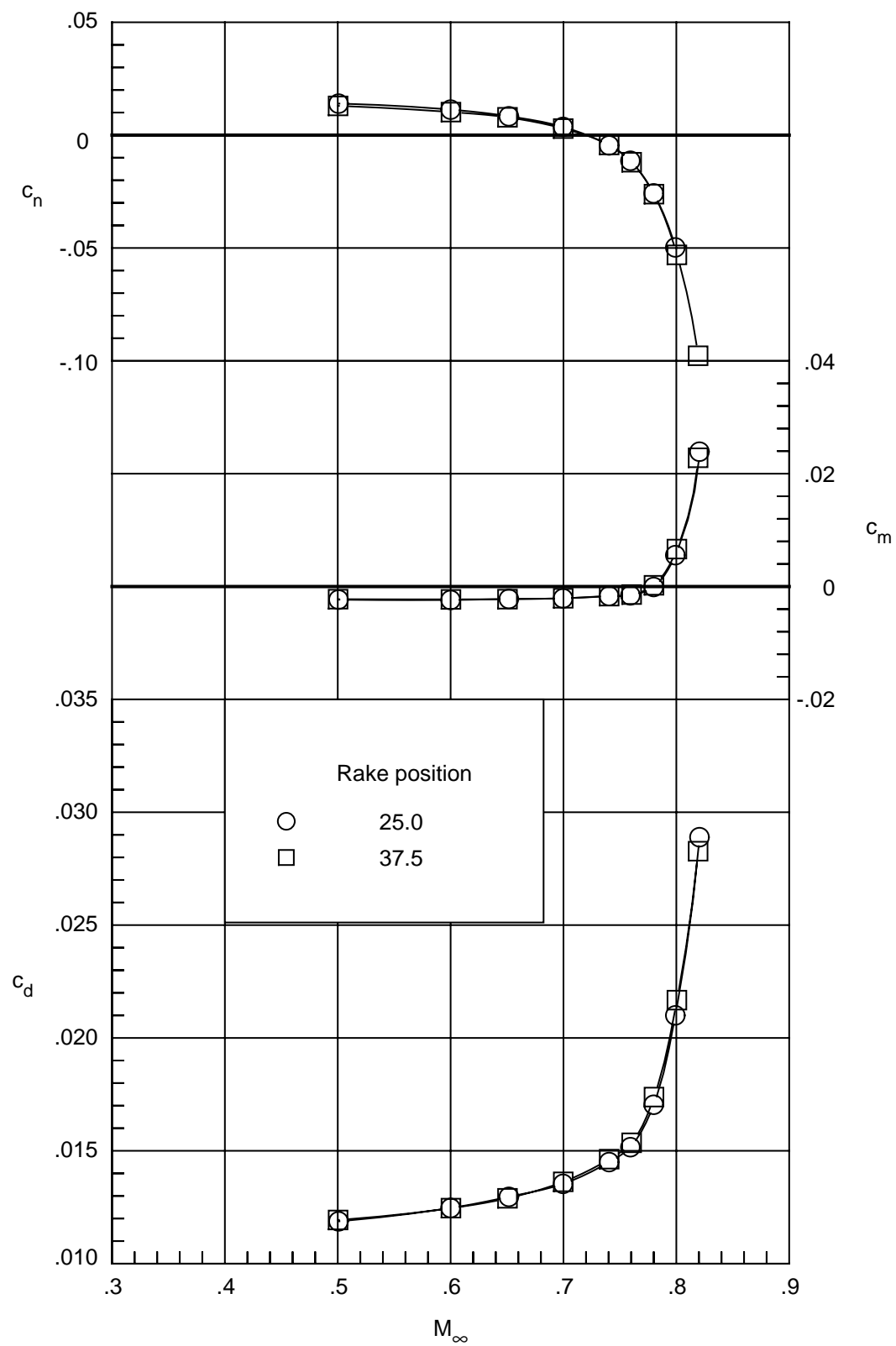
(b) $R_c = 6 \times 10^6$.

Figure 7. Concluded.
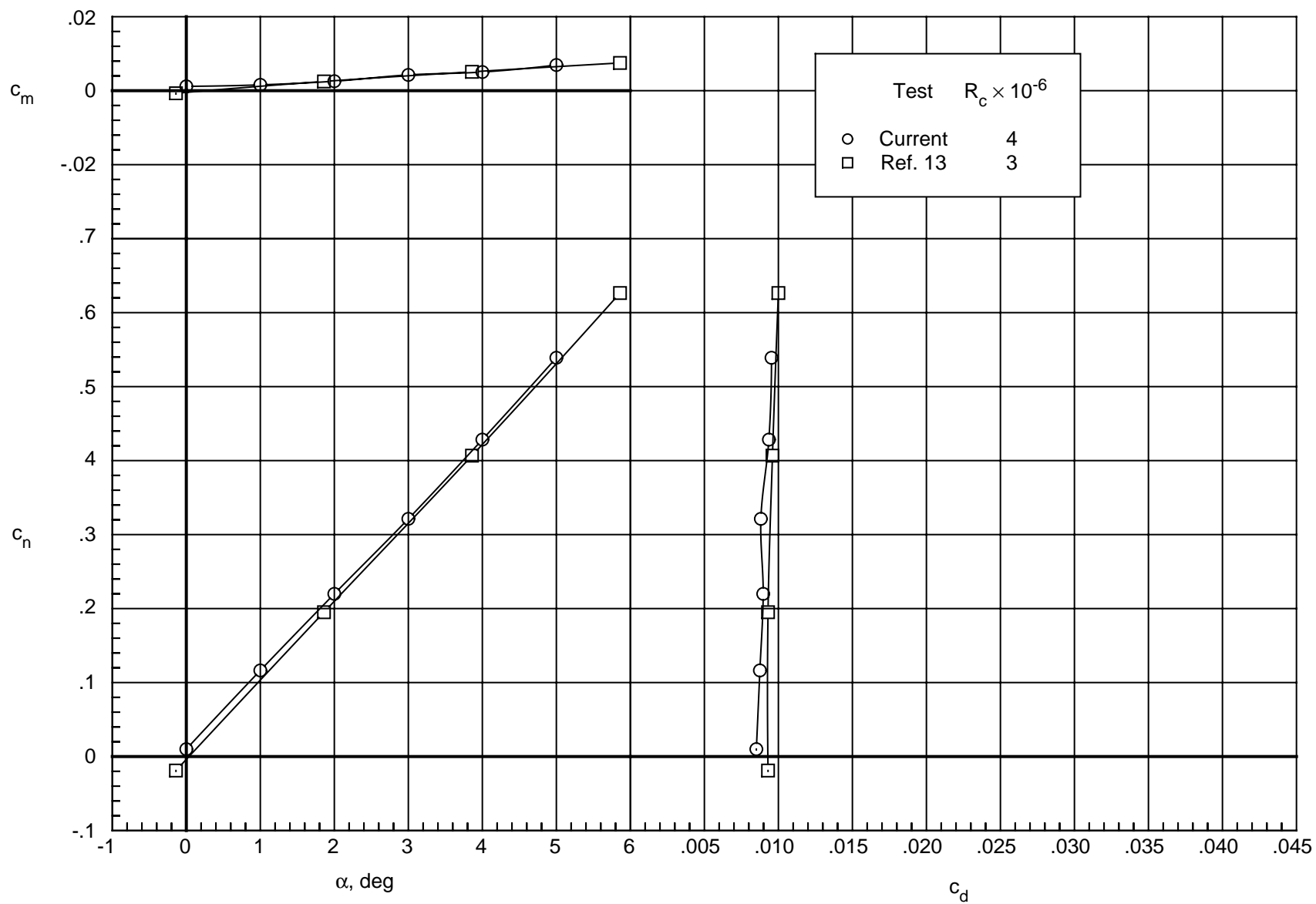
(a) $M_\infty = 0.50$.

Figure 8. Comparison of integrated force and moment coefficients with previous test results for solid surface.
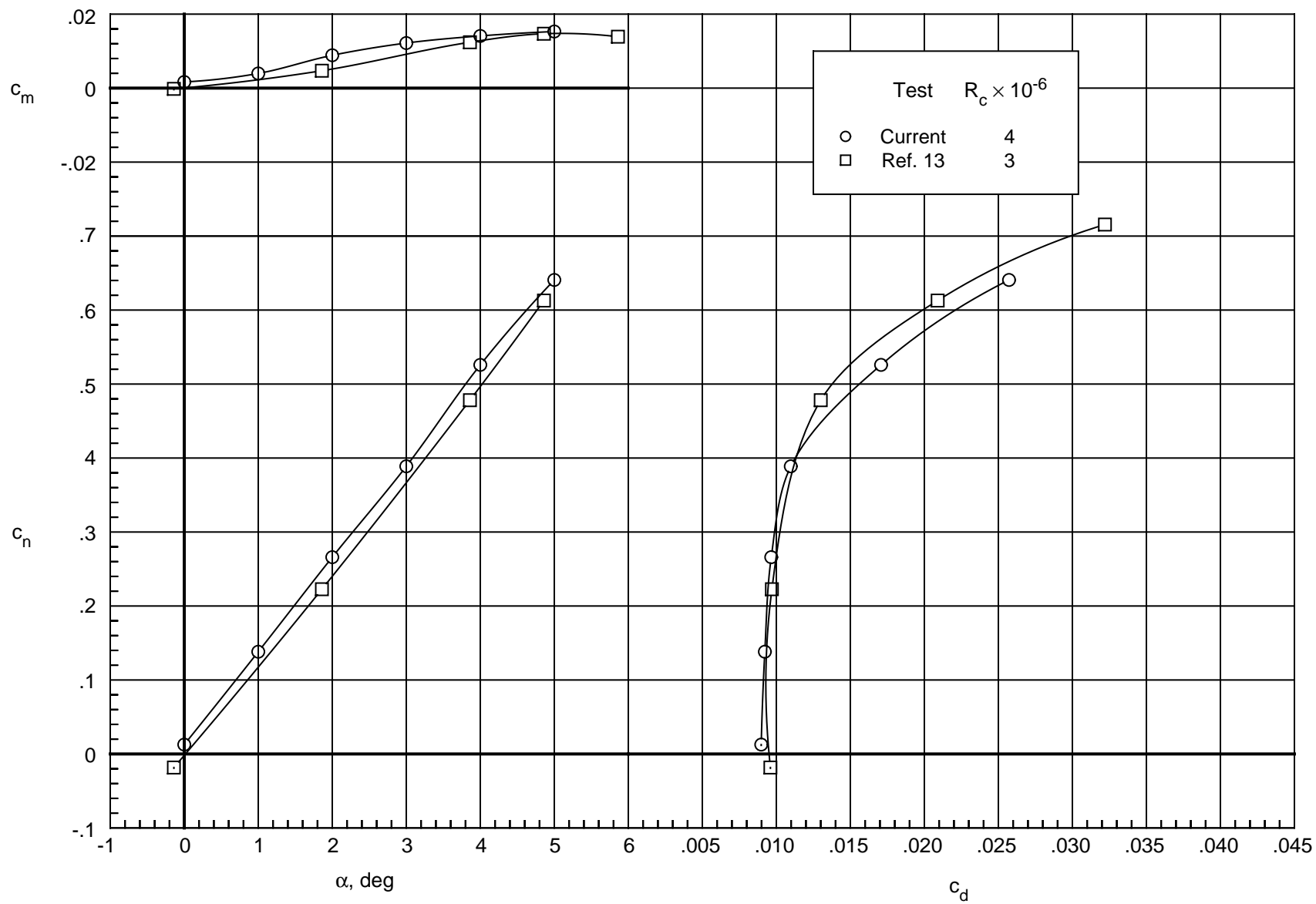
(b) $M_\infty = 0.70$.

Figure 8. Continued.
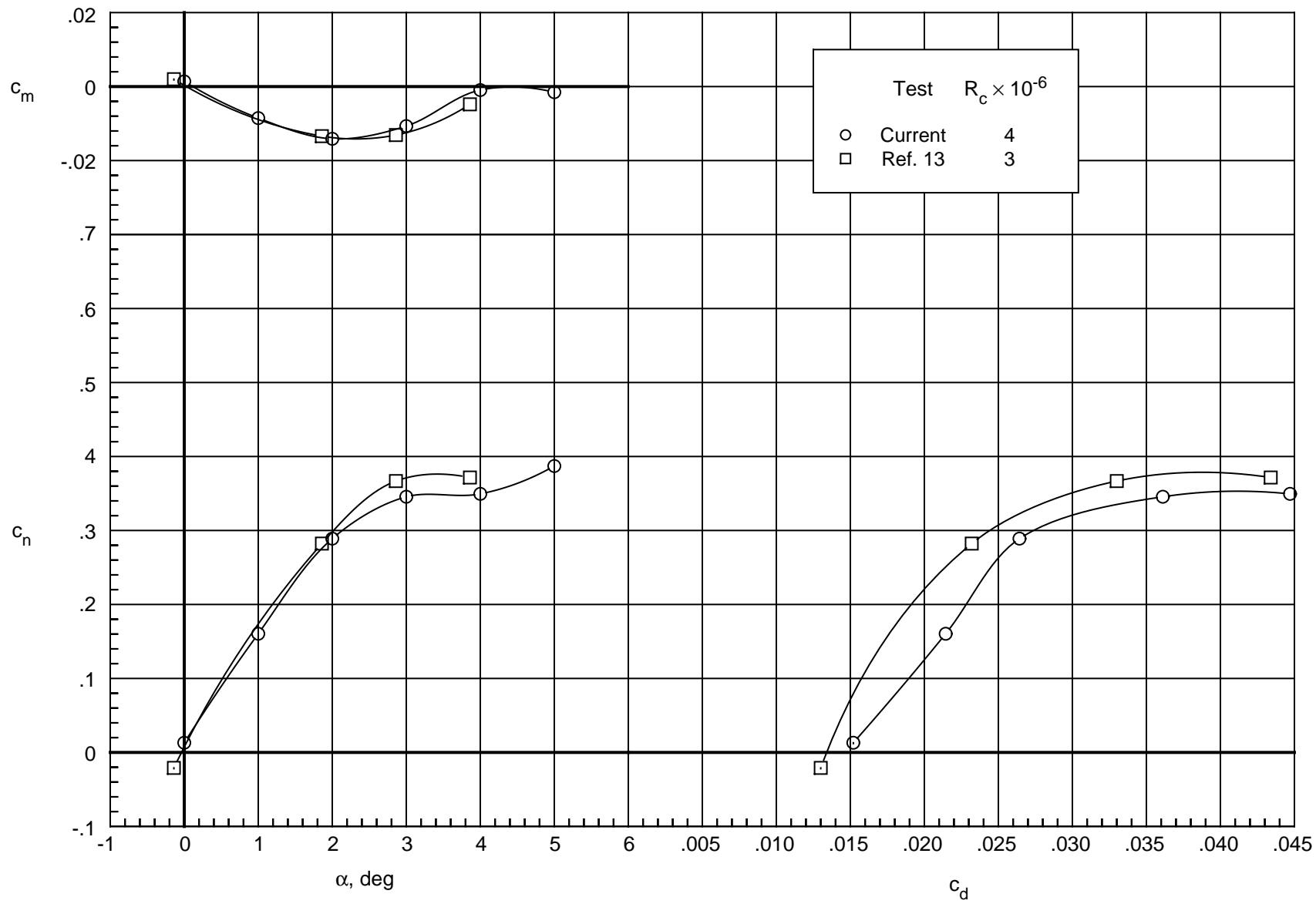
(c) $M_\infty = 0.80$.

Figure 8. Concluded.
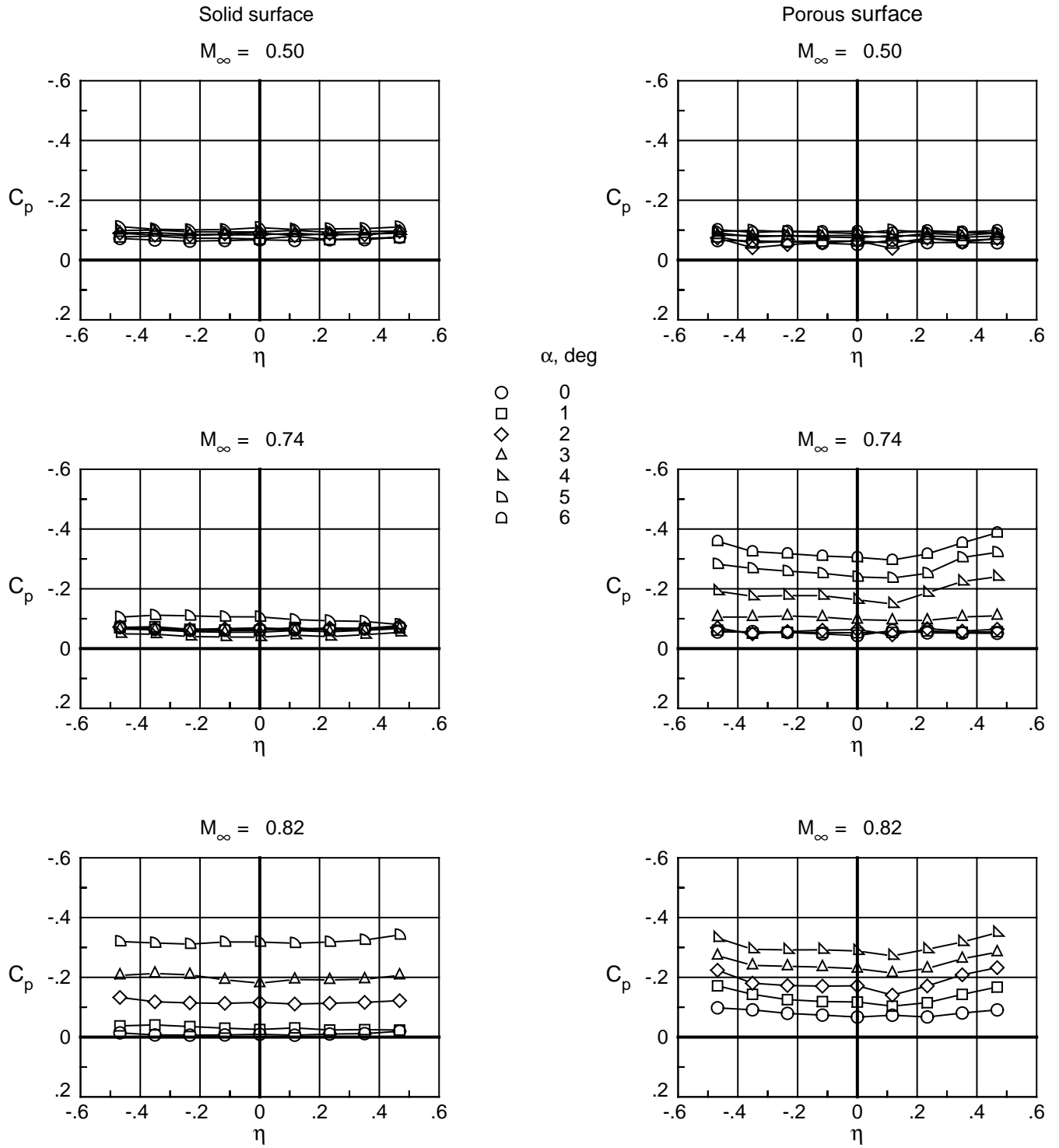
Figure 9. Spanwise surface pressure coefficient distributions for upper surface. $x/c = 0.8$; $R_c = 4 \times 10^6$.
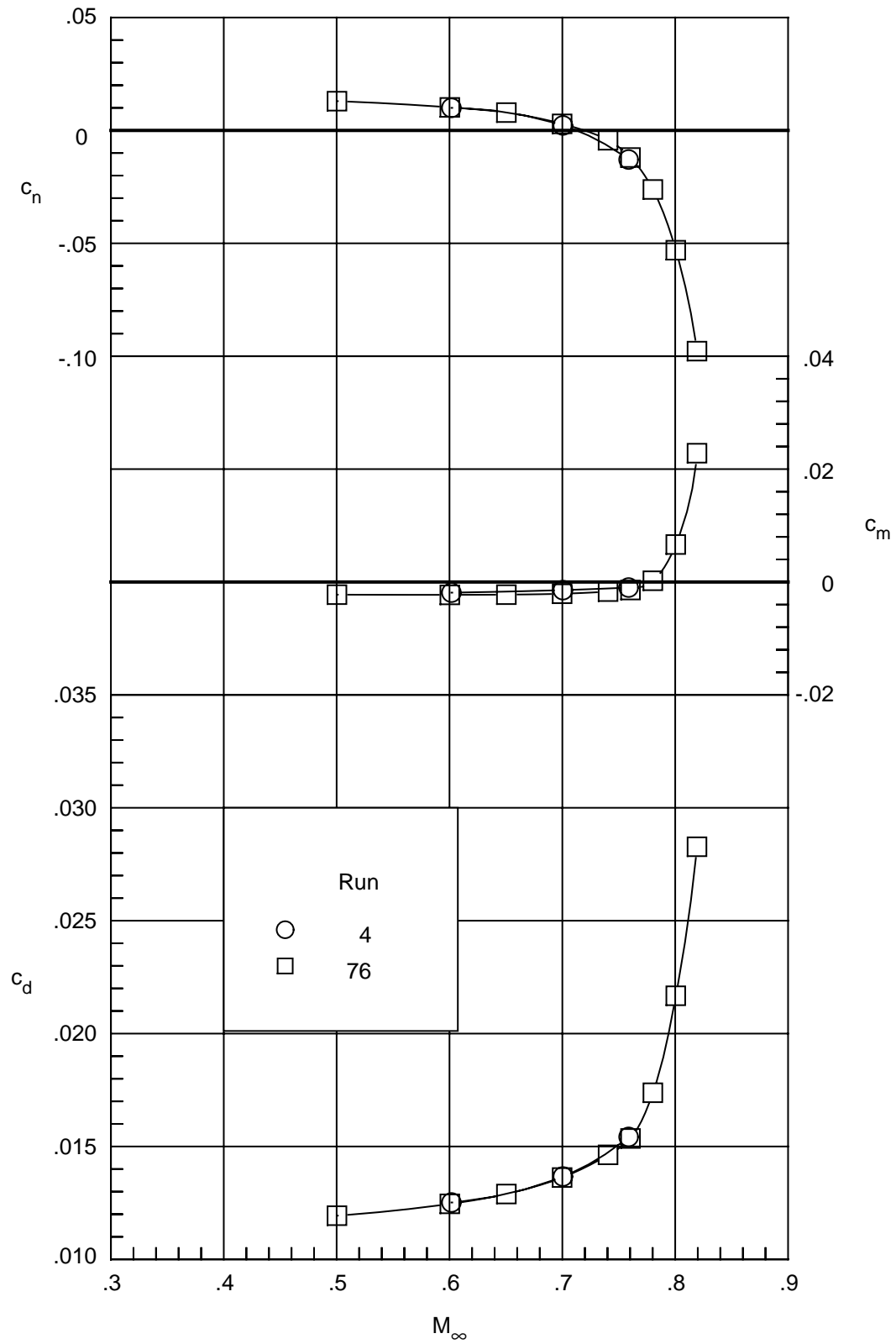
Figure 10. Repeatability of integrated force and moment coefficients of porous airfoil. $\alpha = 0°$; $R_c = 6 \times 10^6$.
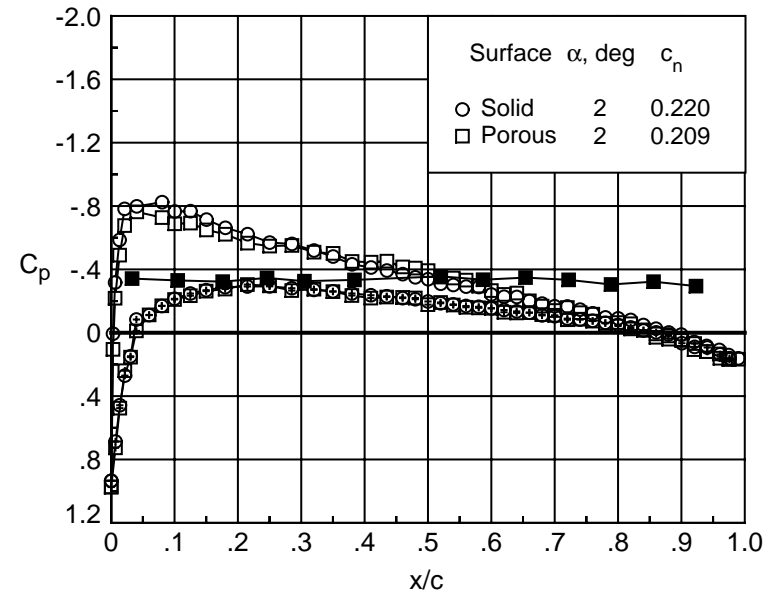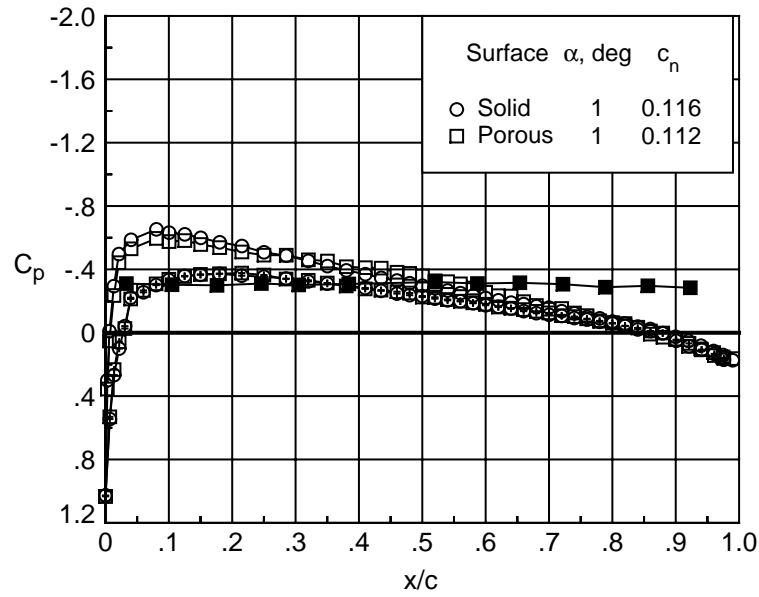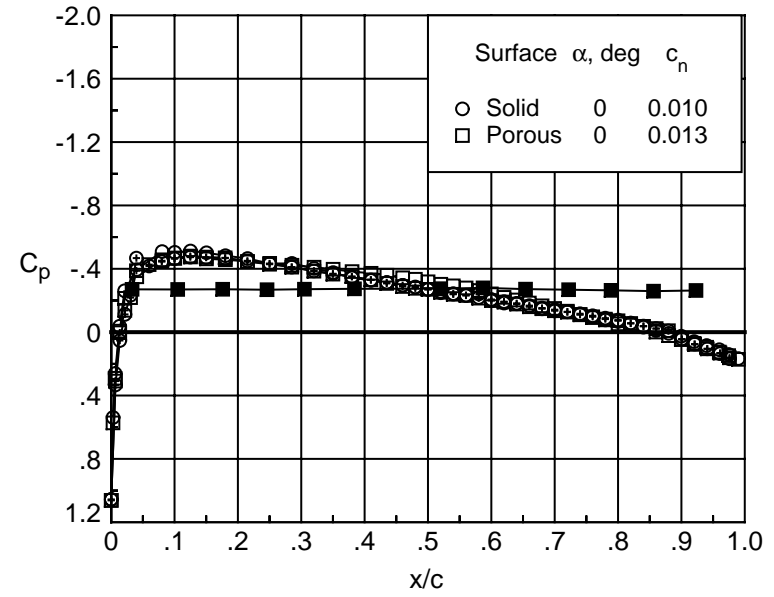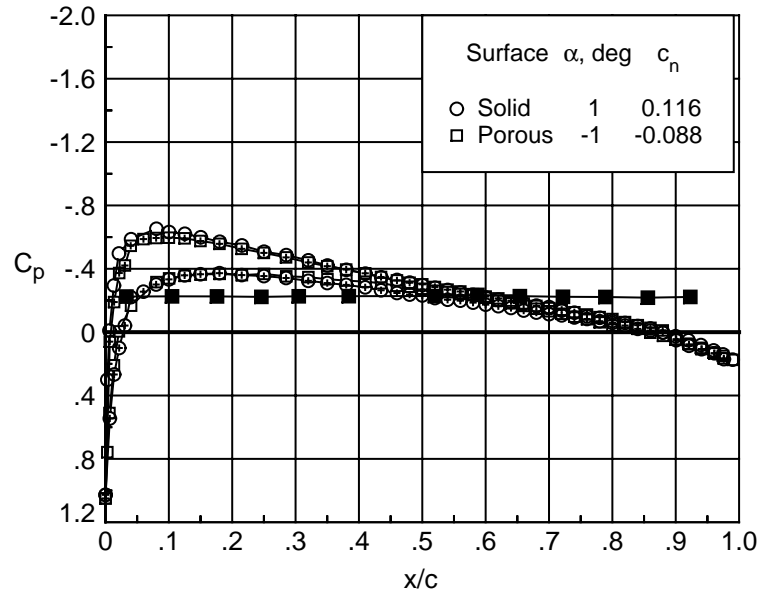
Figure 11. Chordwise surface and cavity pressure coefficient distributions on NACA 0012 with solid and porous upper surface. $M_\infty = 0.50$; $R_c = 4 \times 10^6$. Open symbol denotes upper surface, '+' in symbol denotes lower surface, and solid symbol denotes cavity.
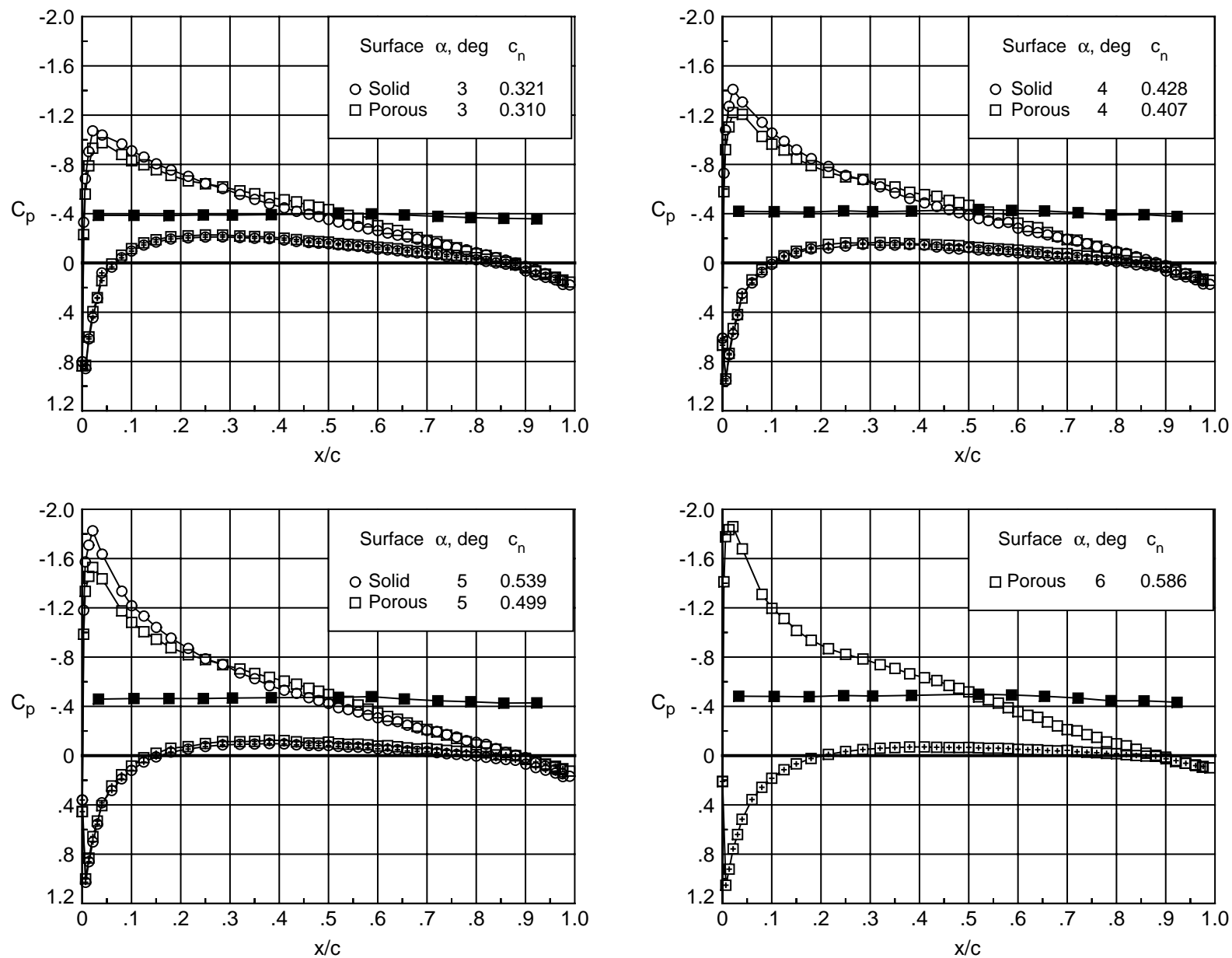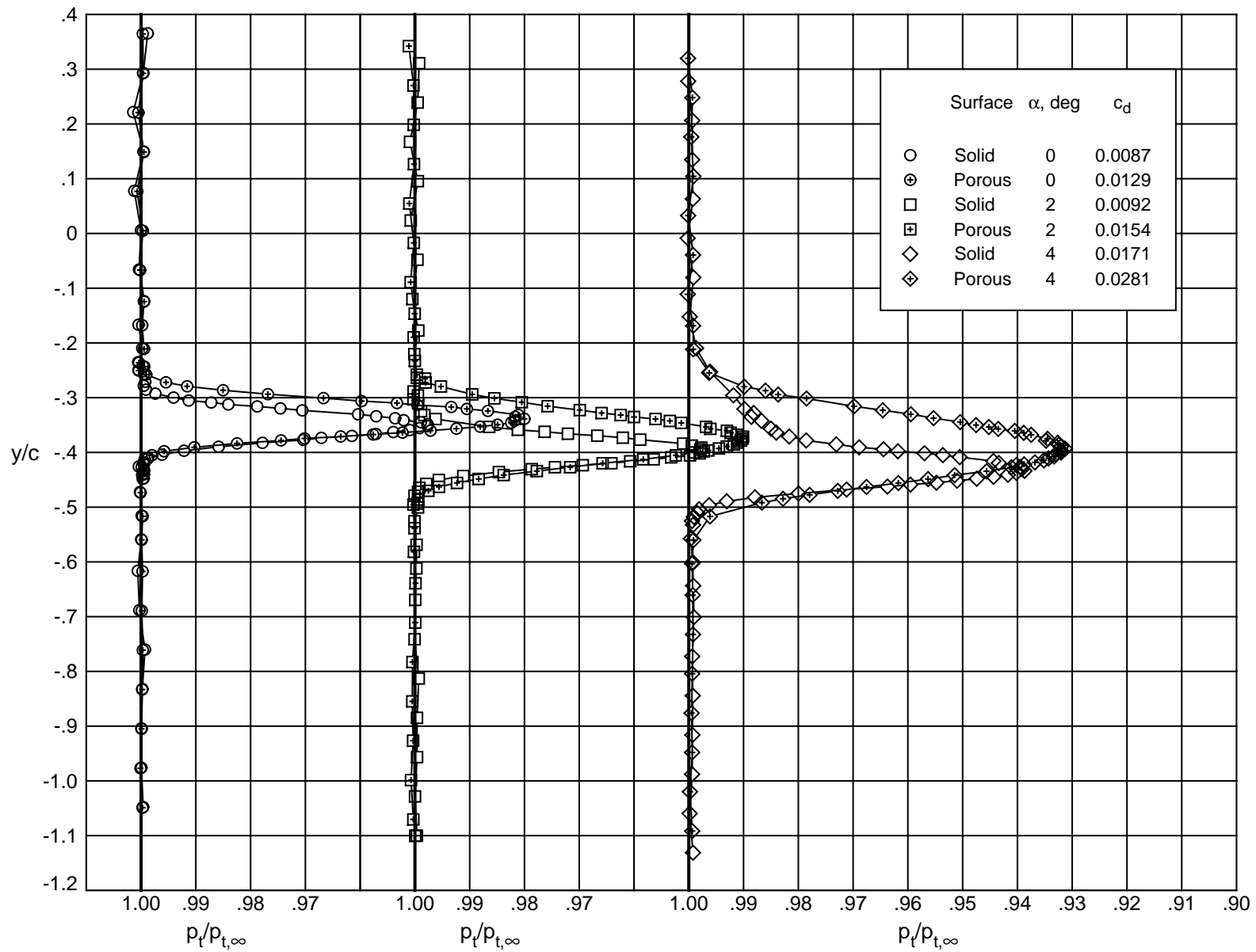
Figure 11. Concluded.
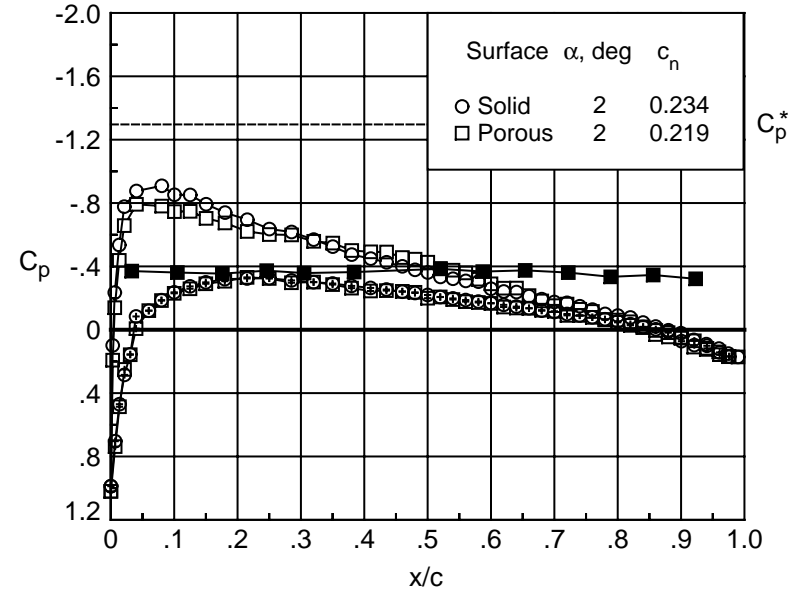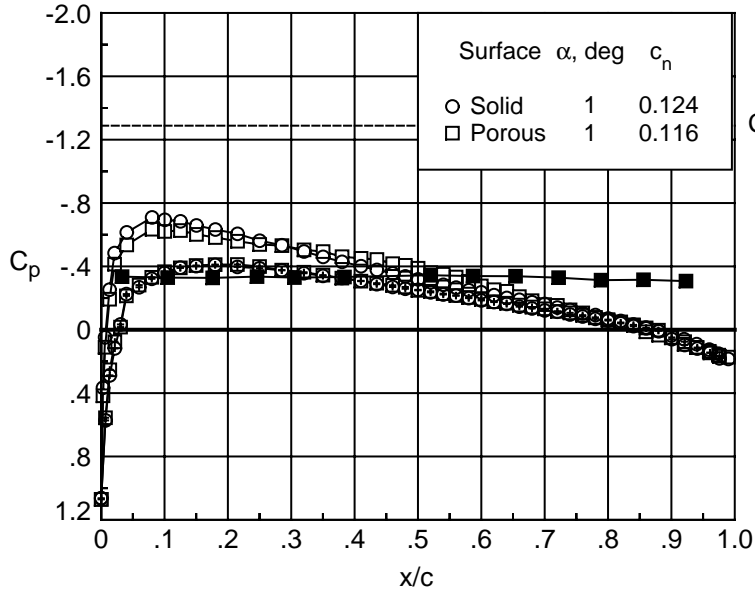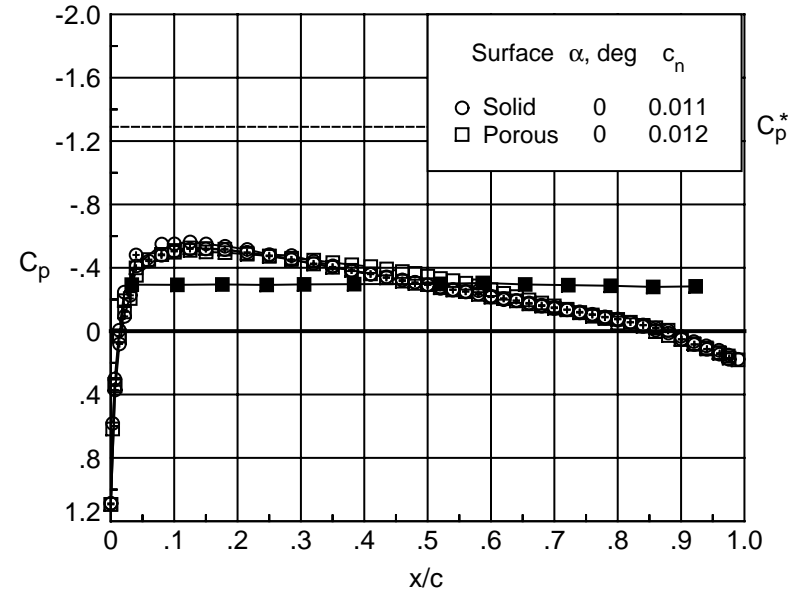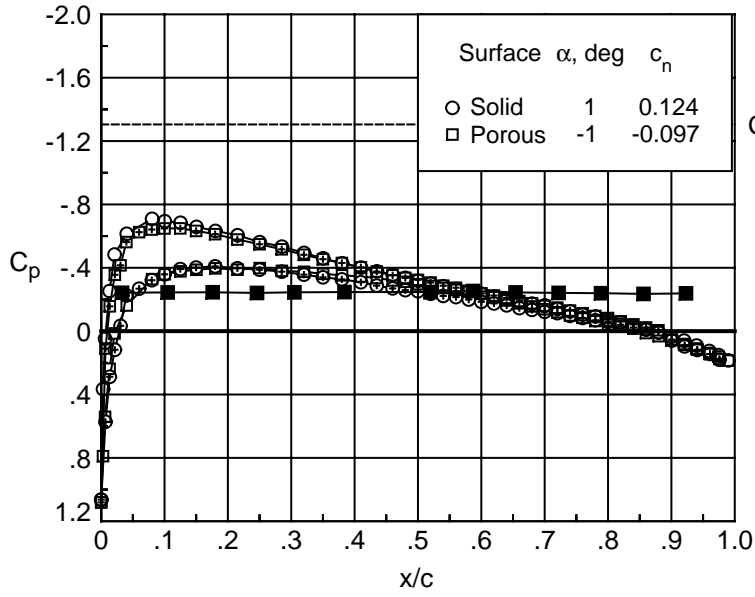
Figure 12. Chordwise surface and cavity pressure coefficient distributions on NACA 0012 with solid and porous upper surface. $M_\infty = 0.60$; $R_c = 4 \times 10^6$. Open symbol denotes upper surface, '+' in symbol denotes lower surface, and solid symbol denotes cavity.
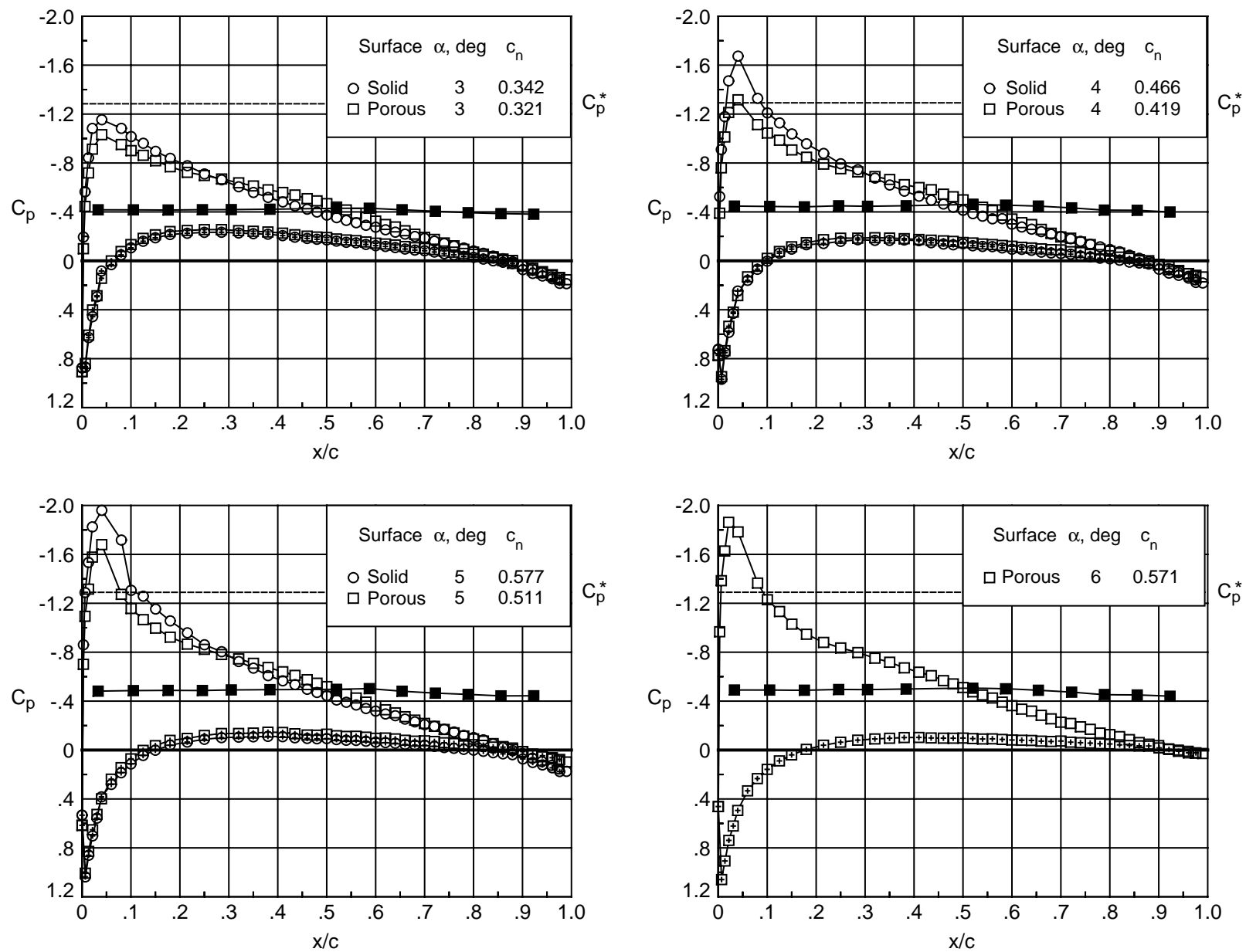
Figure 12. Concluded.
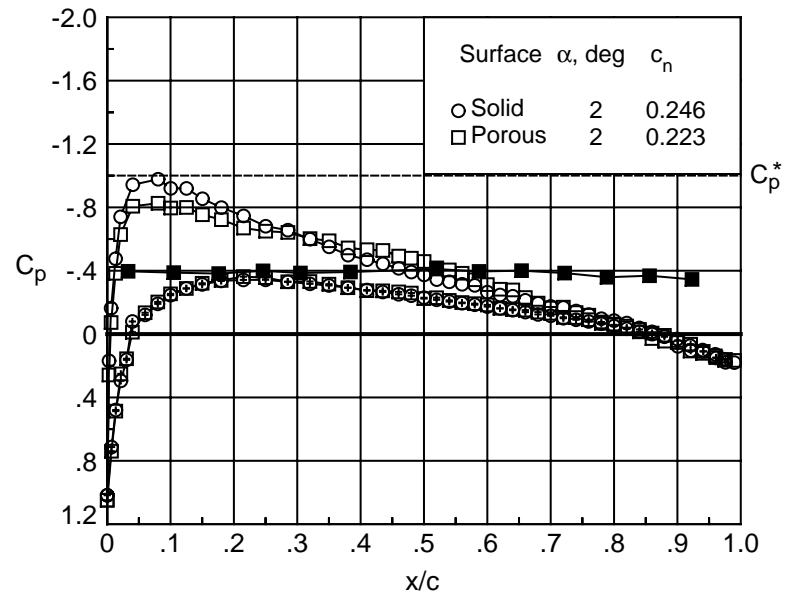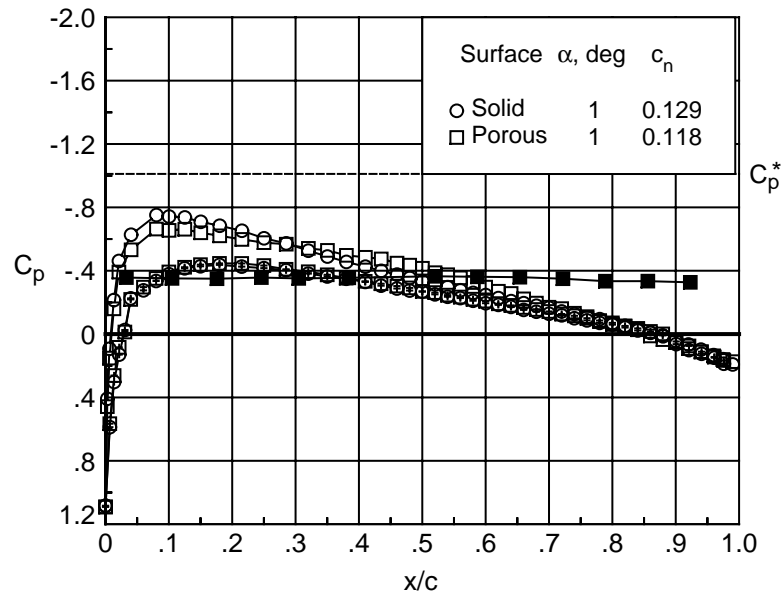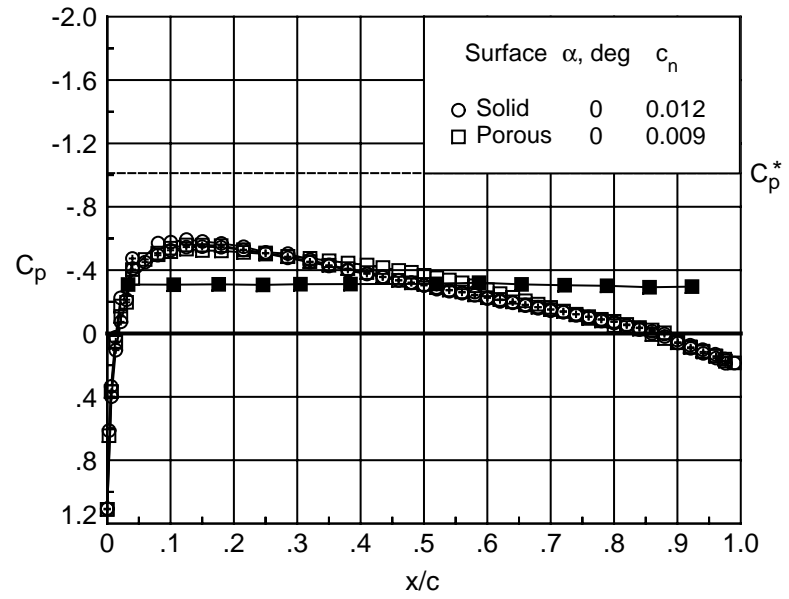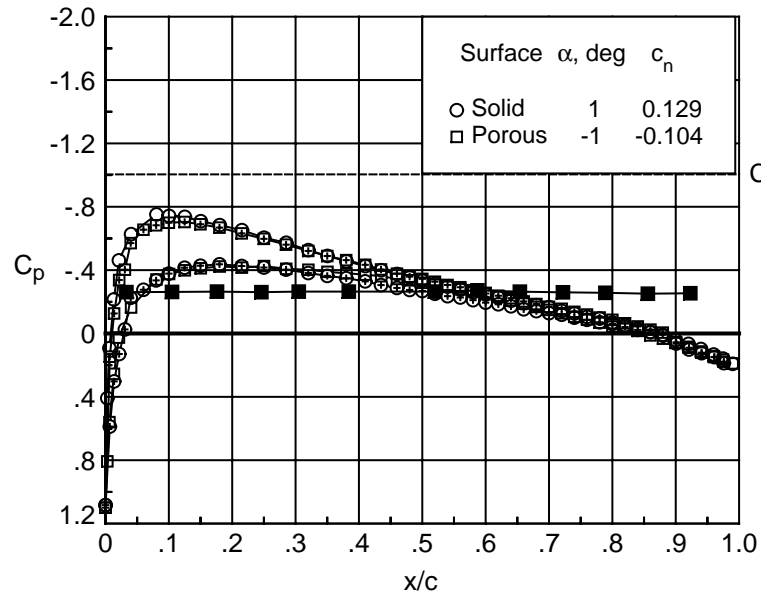
Figure 13. Chordwise surface and cavity pressure coefficient distributions on NACA 0012 with solid and porous upper surface. $M_\infty = 0.65$; $R_c = 4 \times 10^6$. Open symbol denotes upper surface, '+' in symbol denotes lower surface, and solid symbol denotes cavity.
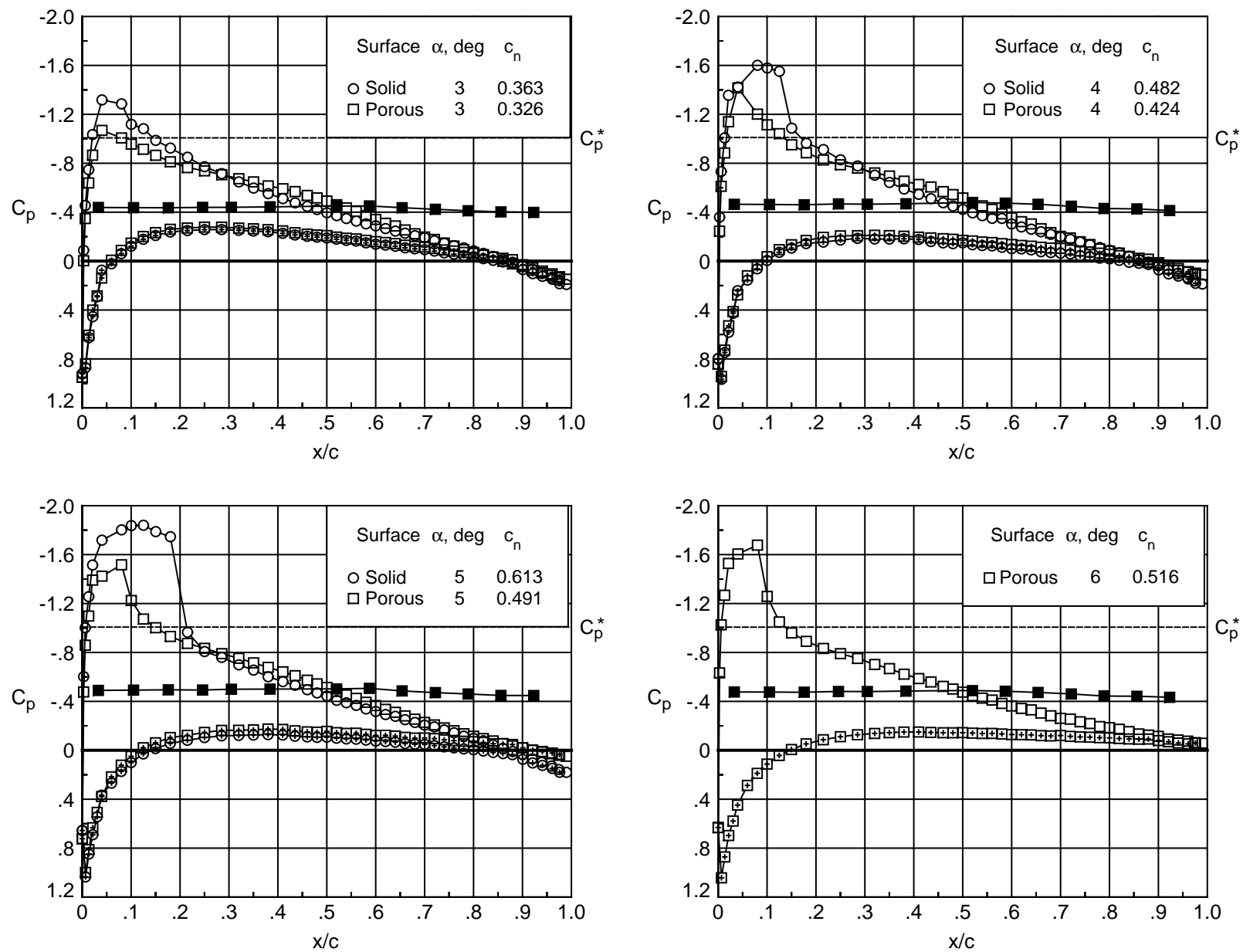
Figure 13. Concluded.
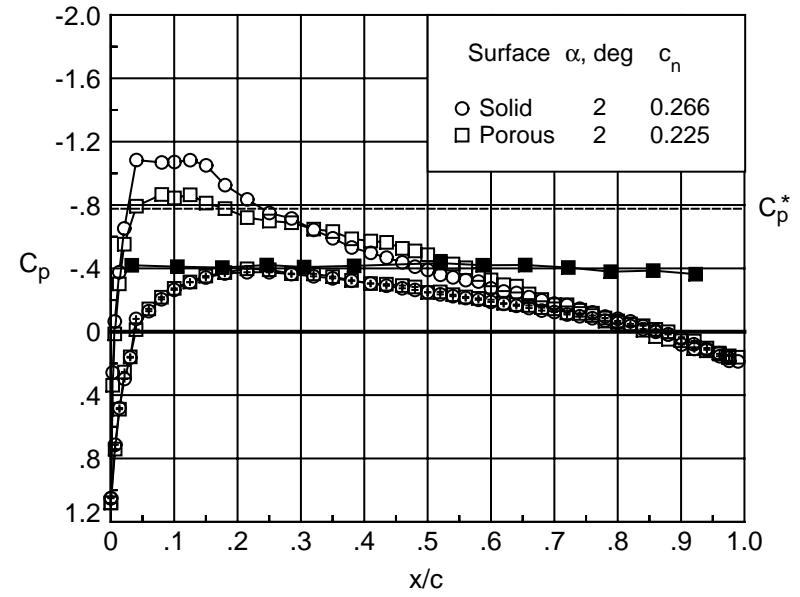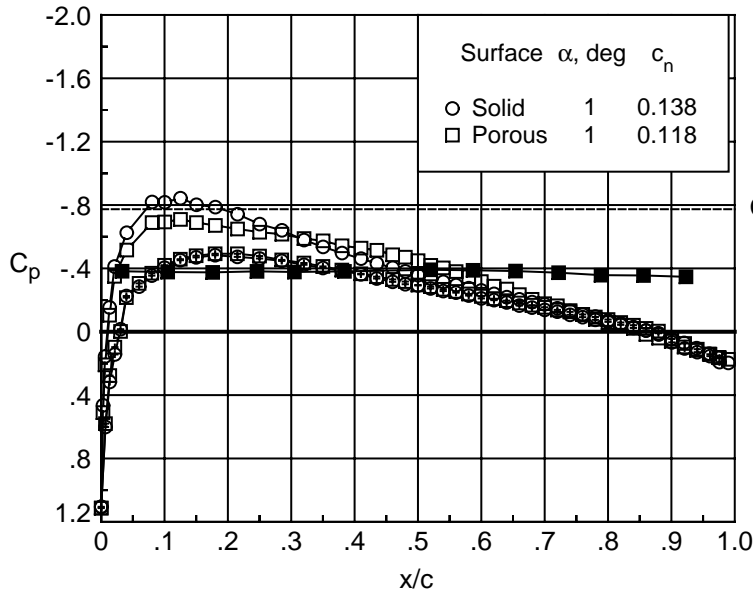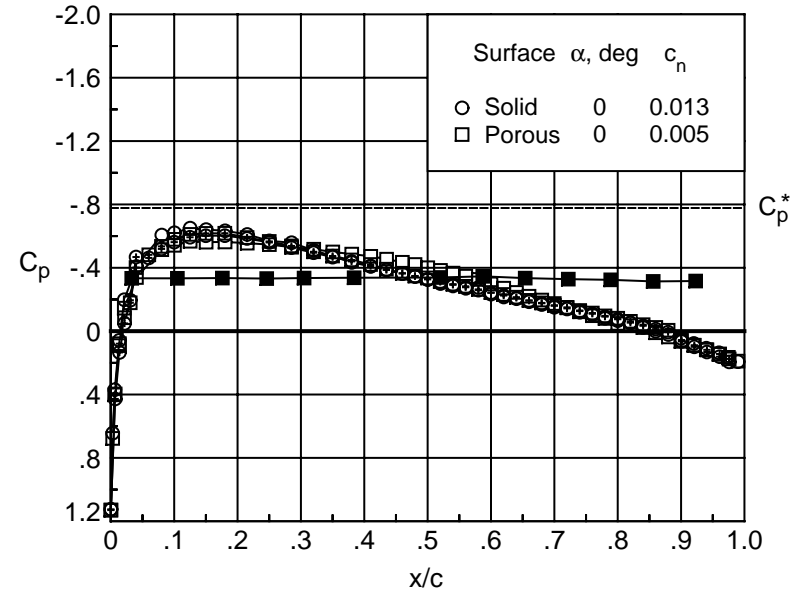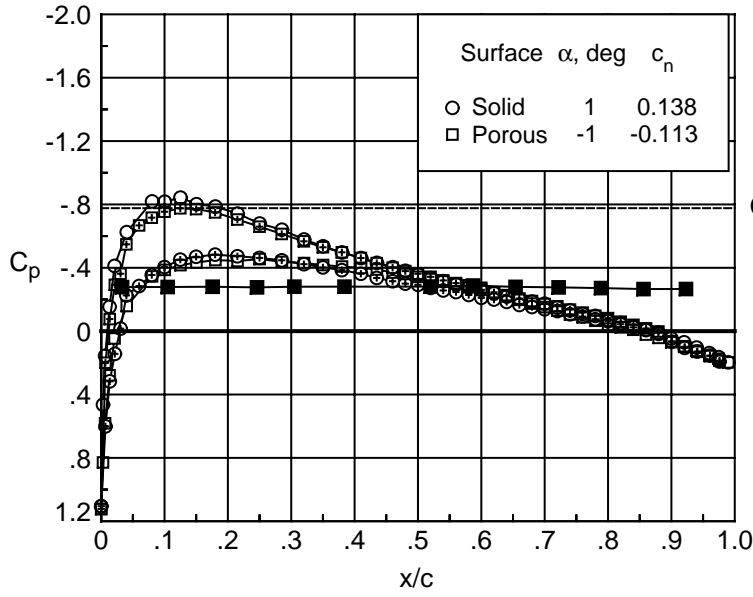
Figure 14. Chordwise surface and cavity pressure coefficient distributions on NACA 0012 with solid and porous upper surface. $M_\infty = 0.70$; $R_c = 4 \times 10^6$. Open symbol denotes upper surface, '+' in symbol denotes lower surface, and solid symbol denotes cavity.
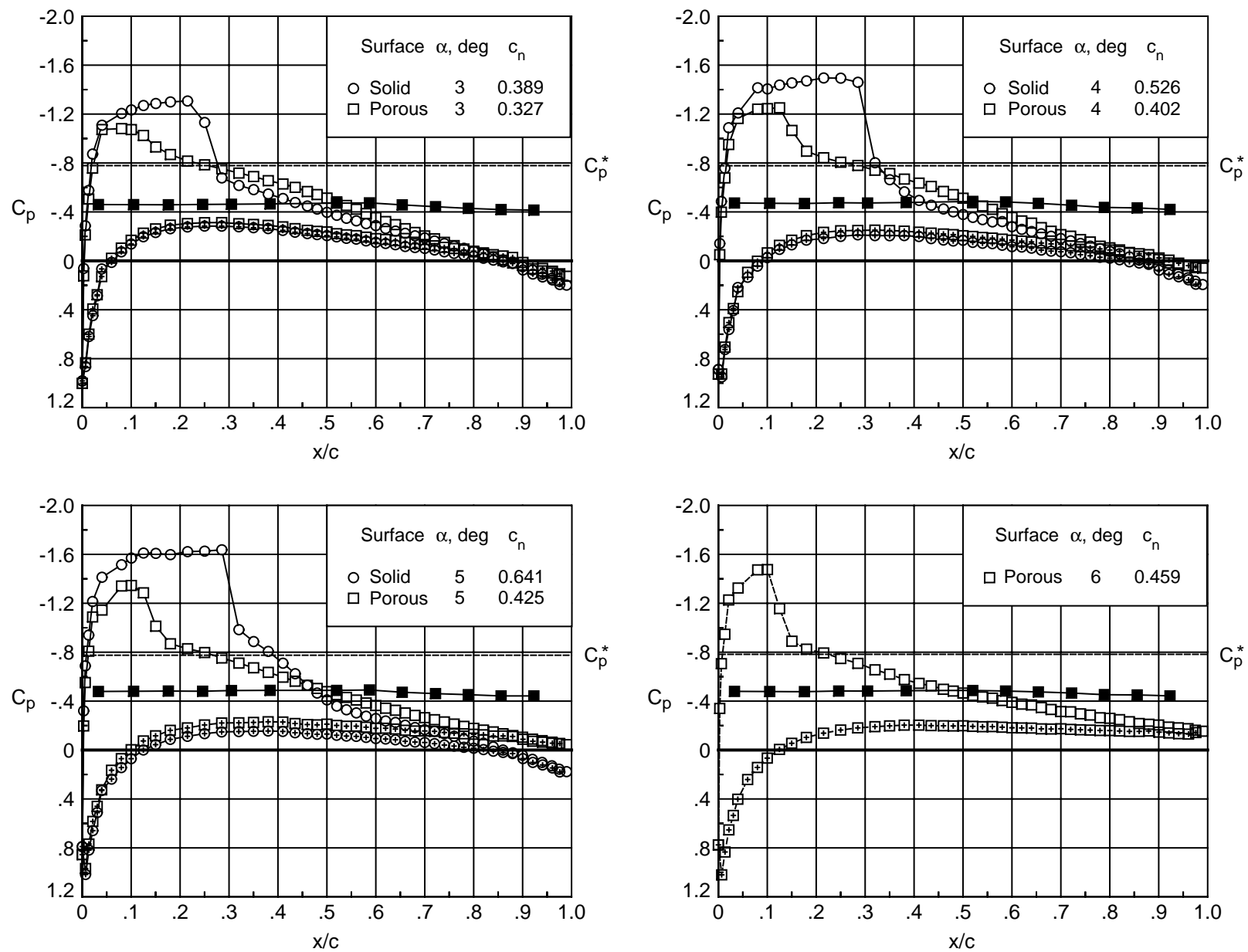
Figure 14. Concluded.
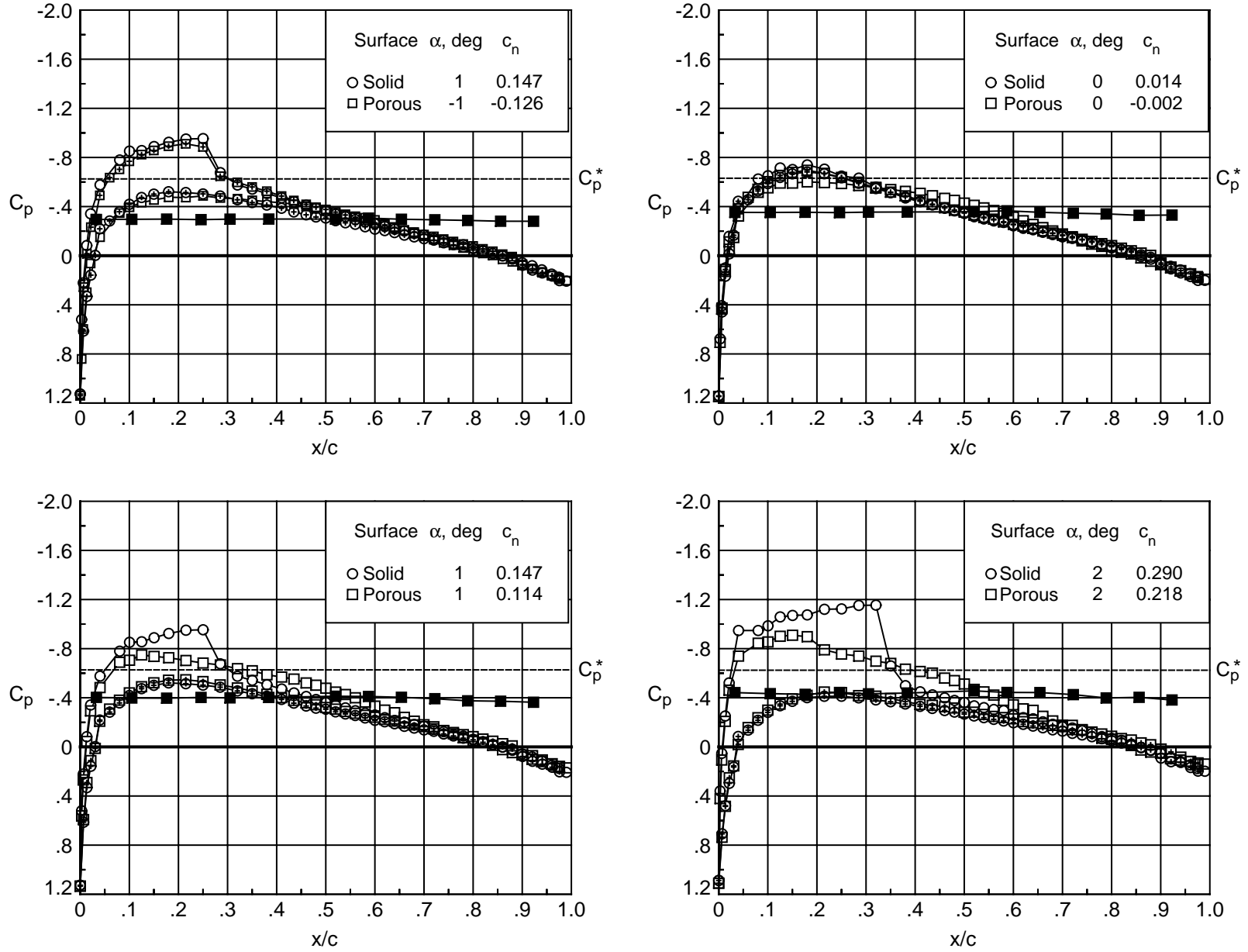
Figure 15. Chordwise surface and cavity pressure coefficient distributions on NACA 0012 with solid and porous upper surface. $M_\infty = 0.74$; $R_c = 4 \times 10^6$. Open symbol denotes upper surface, '+' in symbol denotes lower surface, and solid symbol denotes cavity.
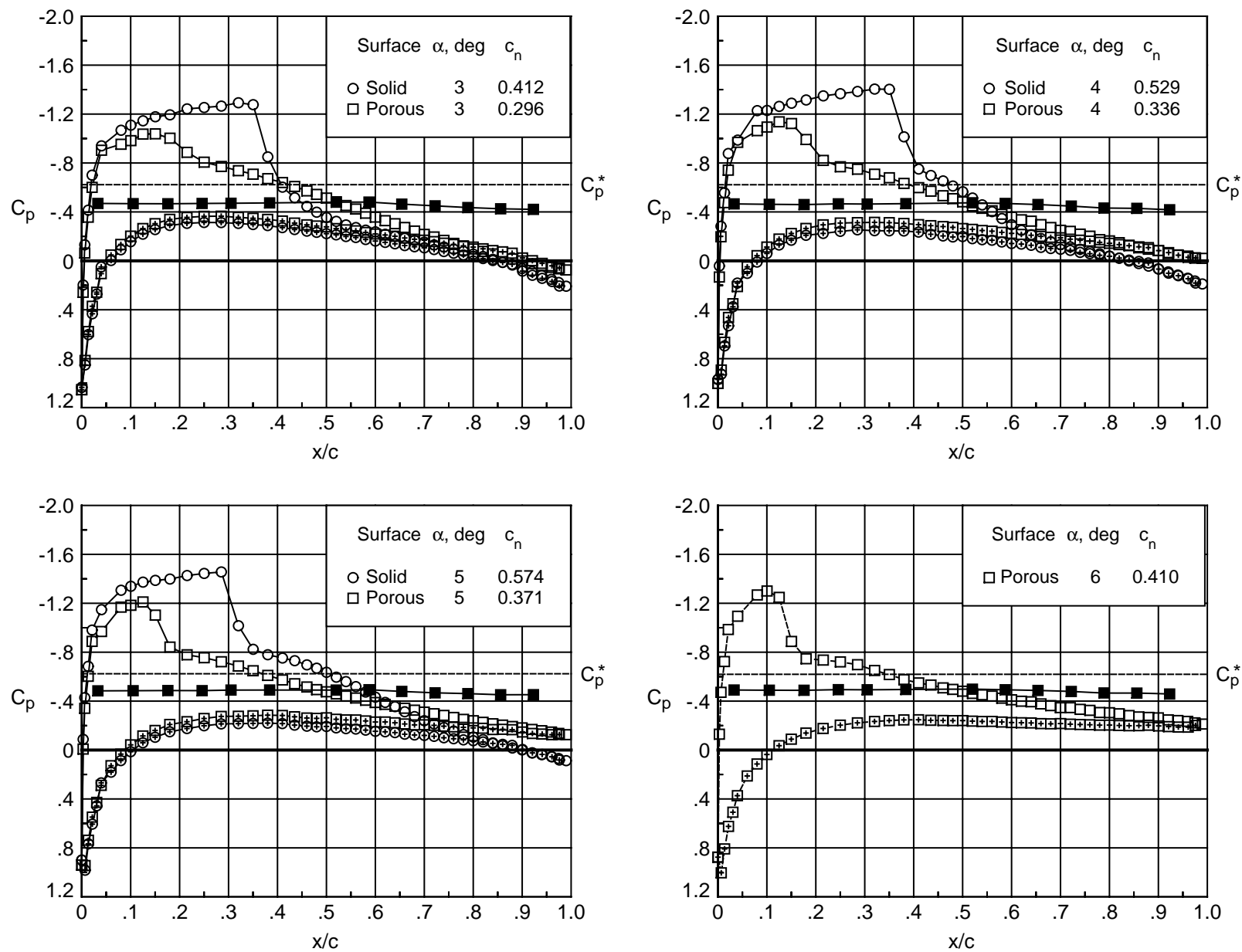
Figure 15. Concluded.
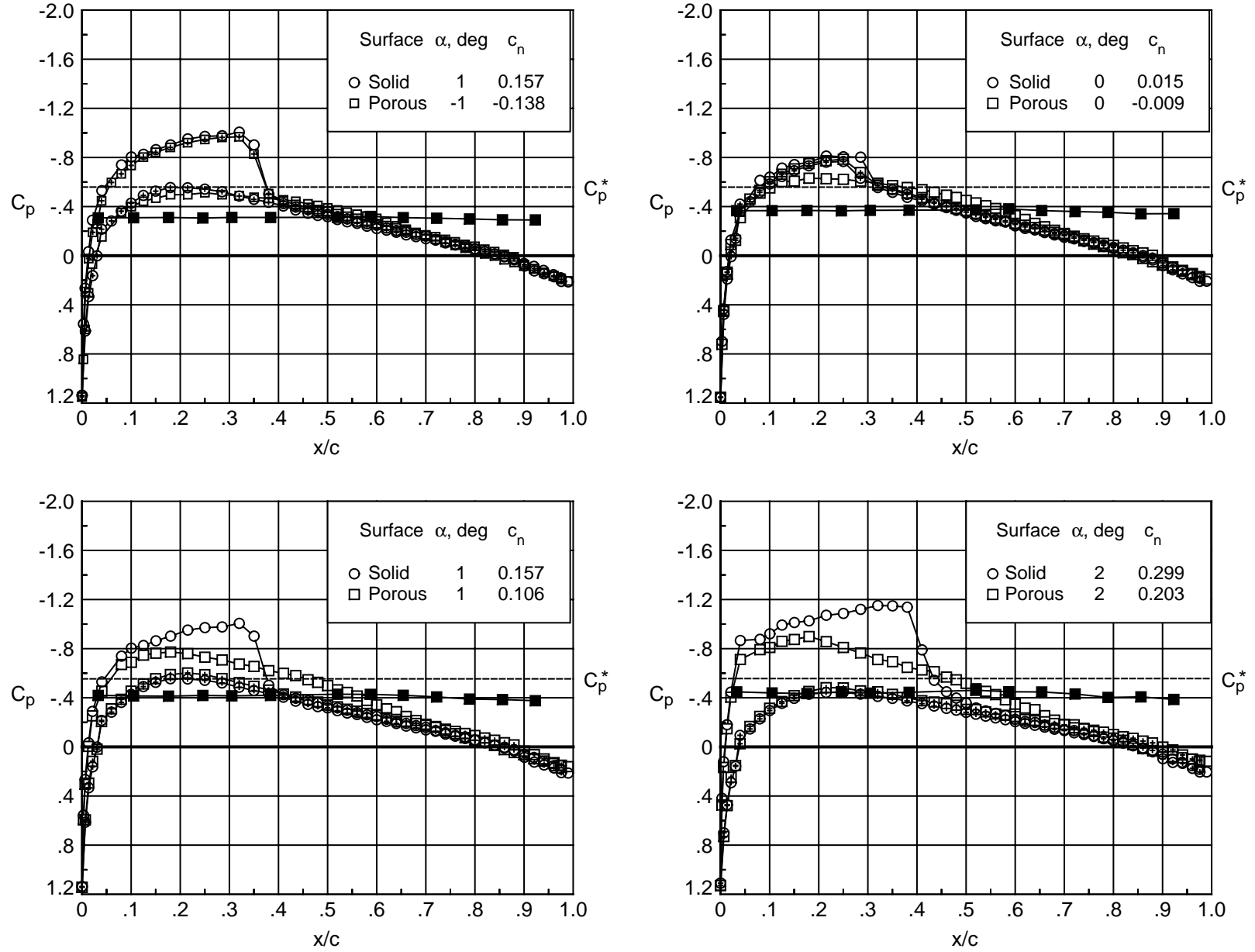
Figure 16. Chordwise surface and cavity pressure coefficient distributions on NACA 0012 with solid and porous upper surface. $M_\infty = 0.76$; $R_c = 4 \times 10^6$. Open symbol denotes upper surface, '+' in symbol denotes lower surface, and solid symbol denotes cavity.
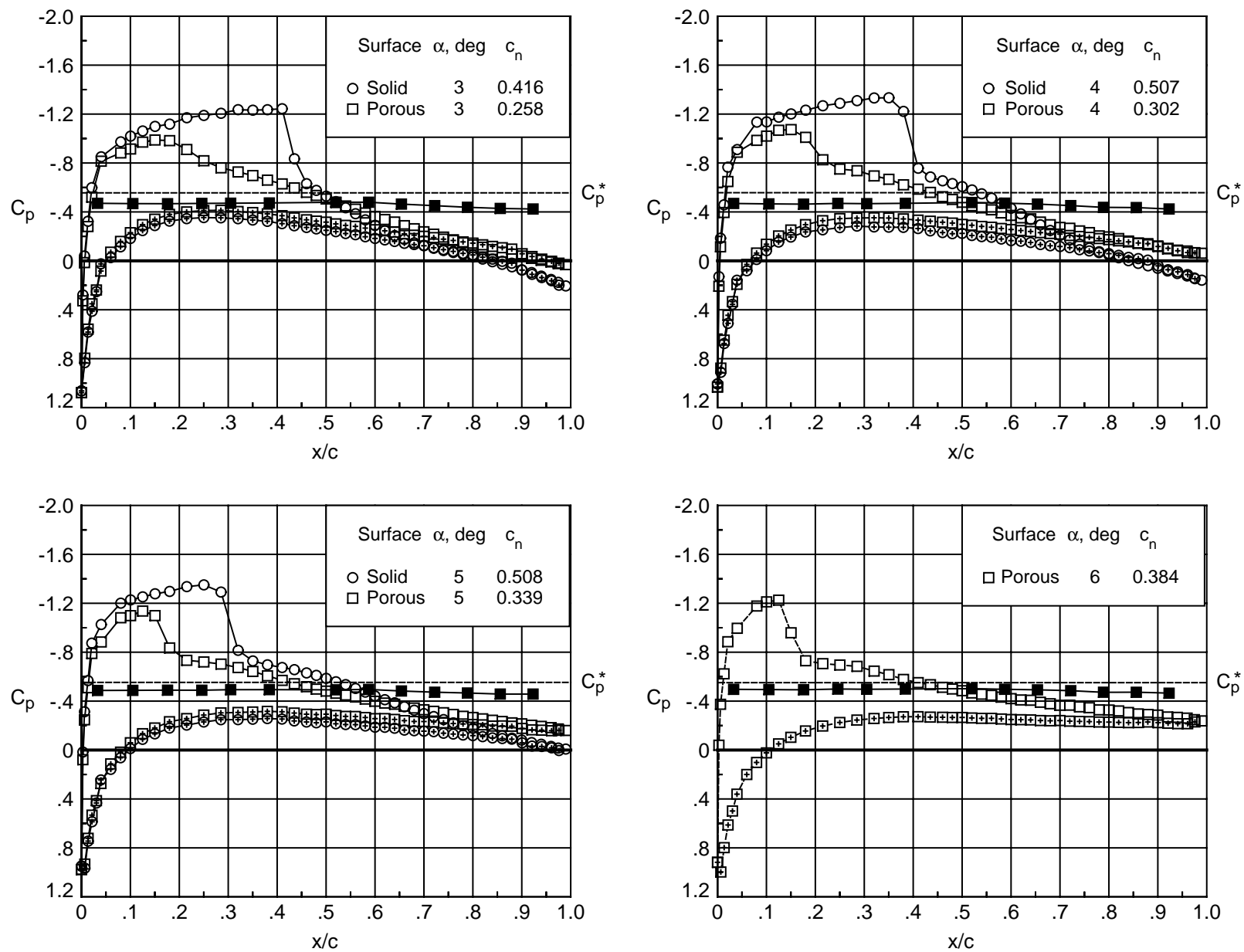
Figure 16. Concluded.
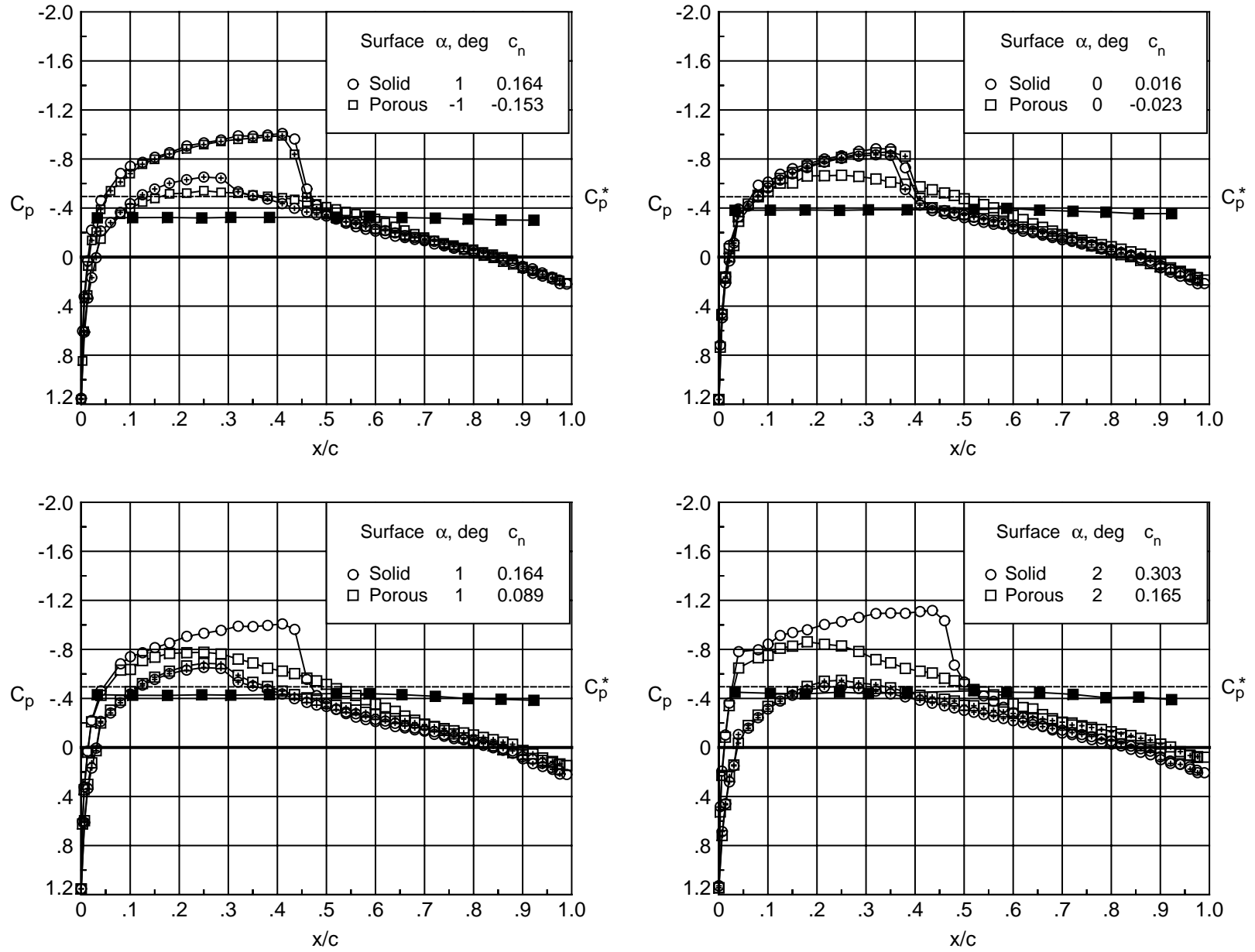
Figure 17. Chordwise surface and cavity pressure coefficient distributions on NACA 0012 with solid and porous upper surface. $M_\infty = 0.78$; $R_c = 4 \times 10^6$. Open symbol denotes upper surface, '+' in symbol denotes lower surface, and solid symbol denotes cavity.
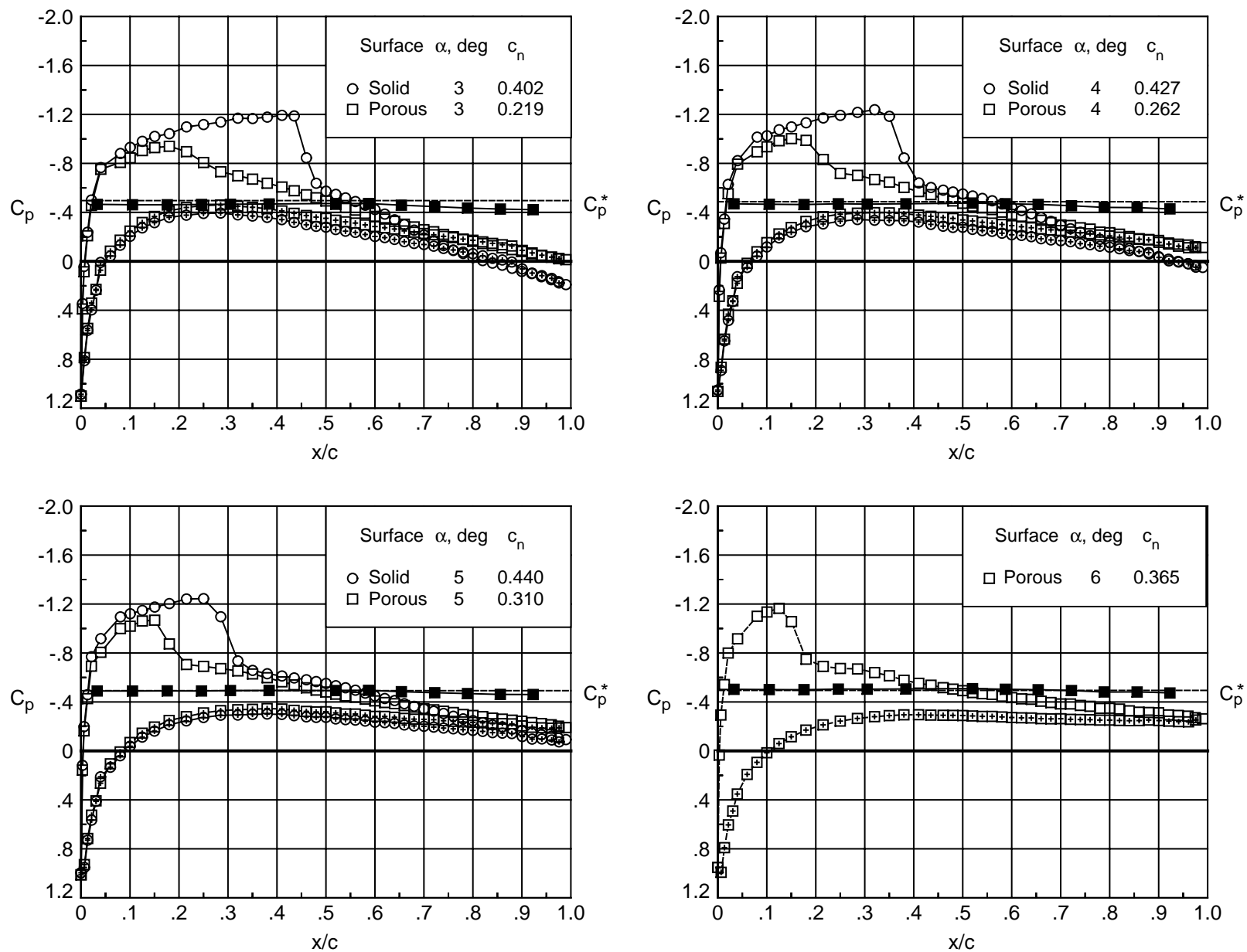
Figure 17. Concluded.
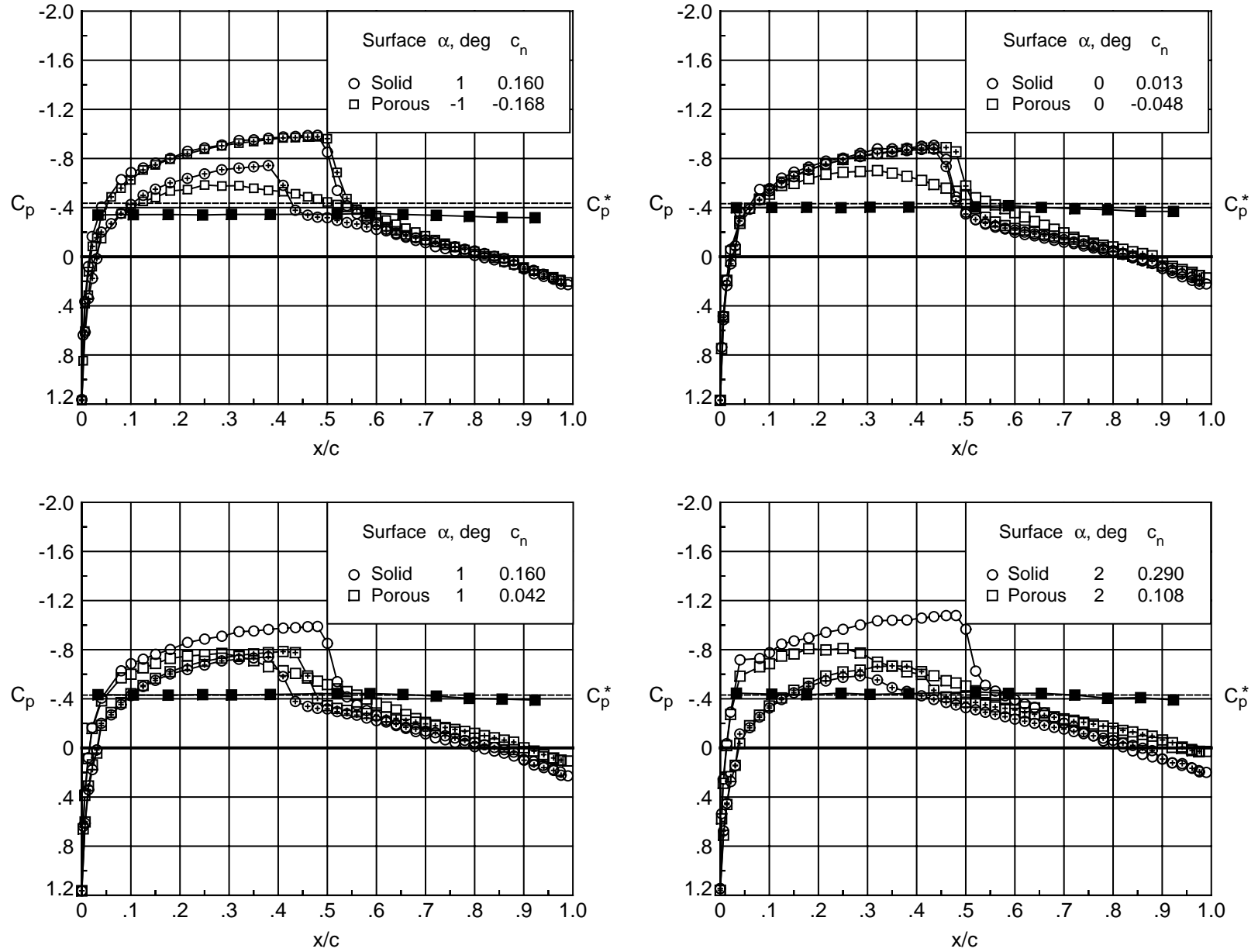
Figure 18. Chordwise surface and cavity pressure coefficient distributions on NACA 0012 with solid and porous upper surface. $M_\infty = 0.80$; $R_c = 4 \times 10^6$. Open symbol denotes upper surface, '+' in symbol denotes lower surface, and solid symbol denotes cavity.
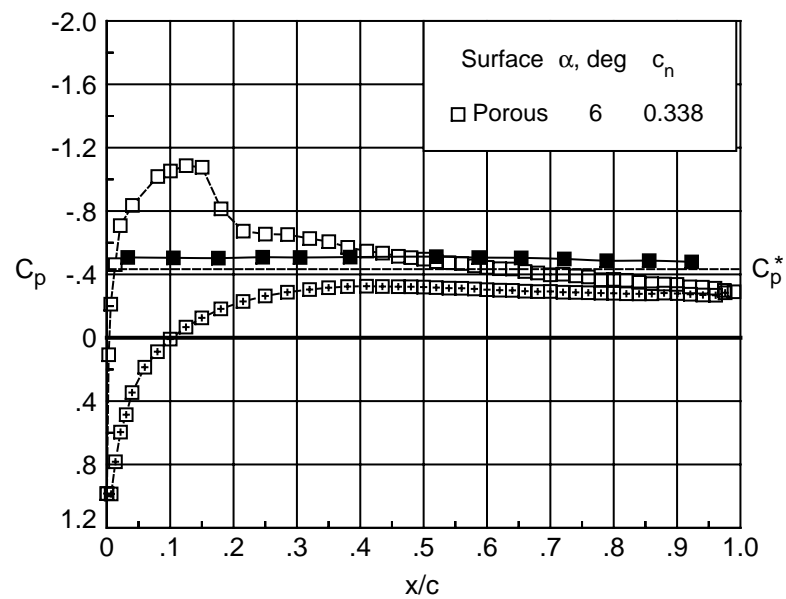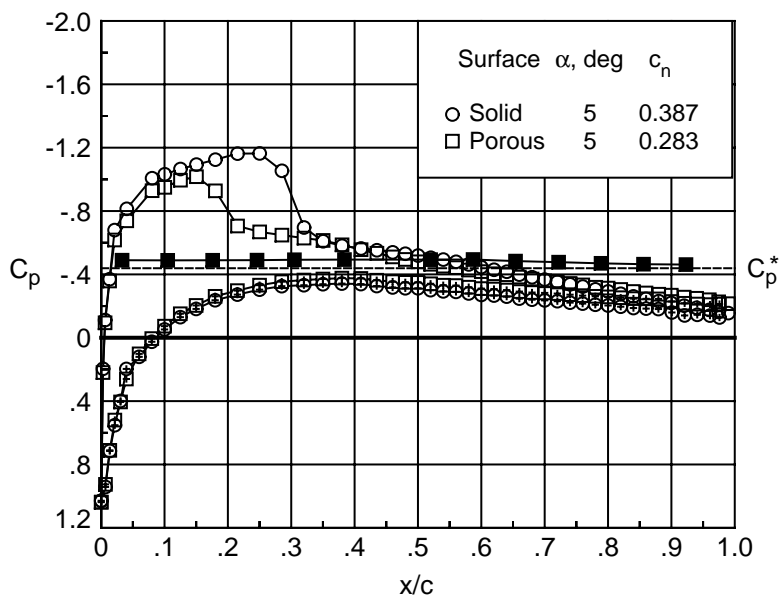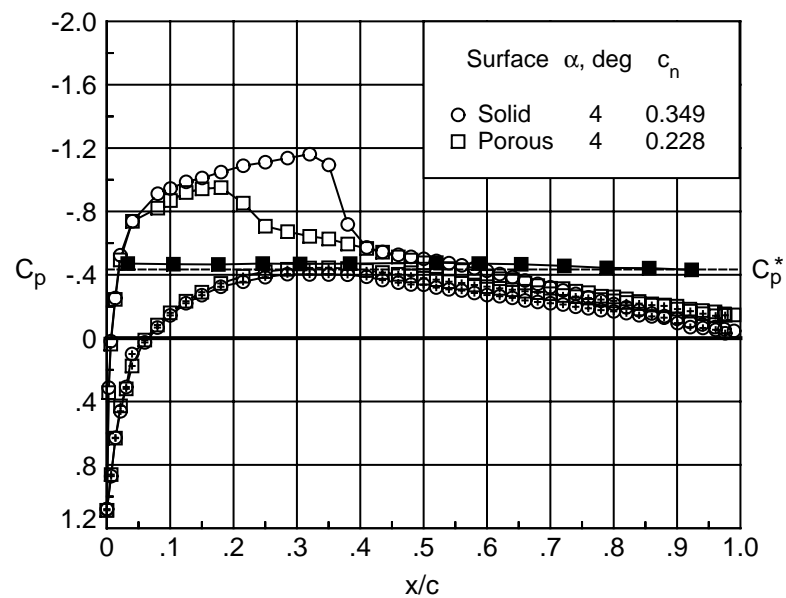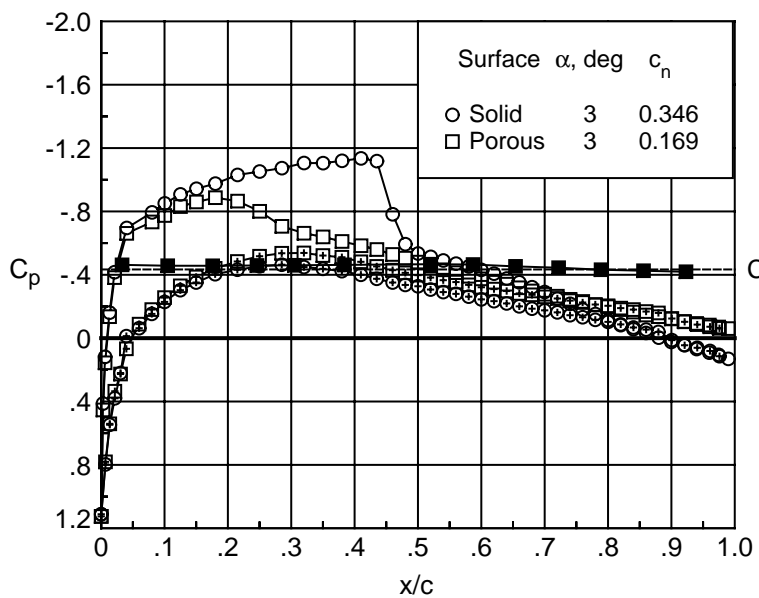
Figure 18. Concluded.
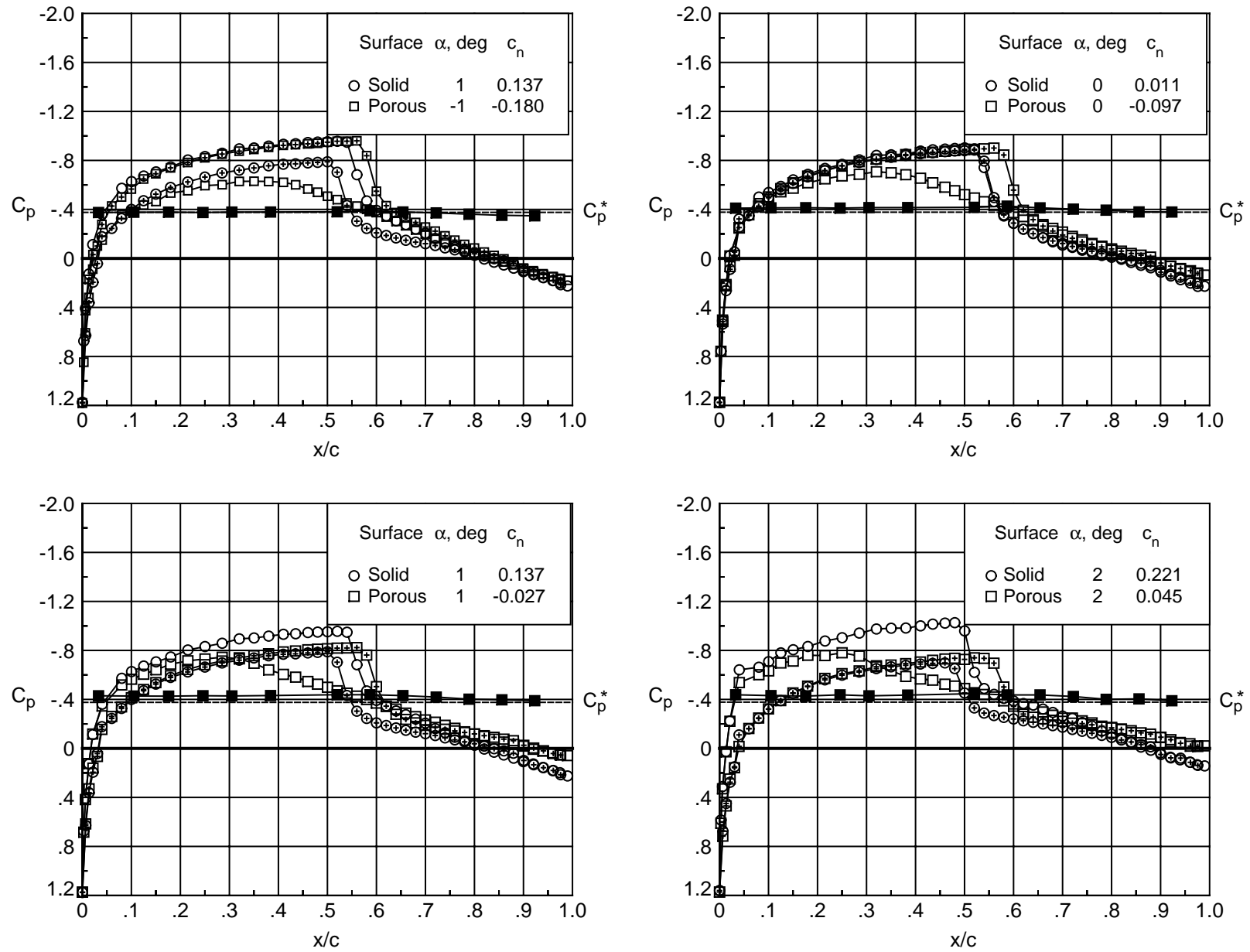
Figure 19. Chordwise surface and cavity pressure coefficient distributions on NACA 0012 with solid and porous upper surface. $M_\infty = 0.82$; $R_c = 4 \times 10^6$. Open symbol denotes upper surface, '+' in symbol denotes lower surface, and solid symbol denotes cavity.
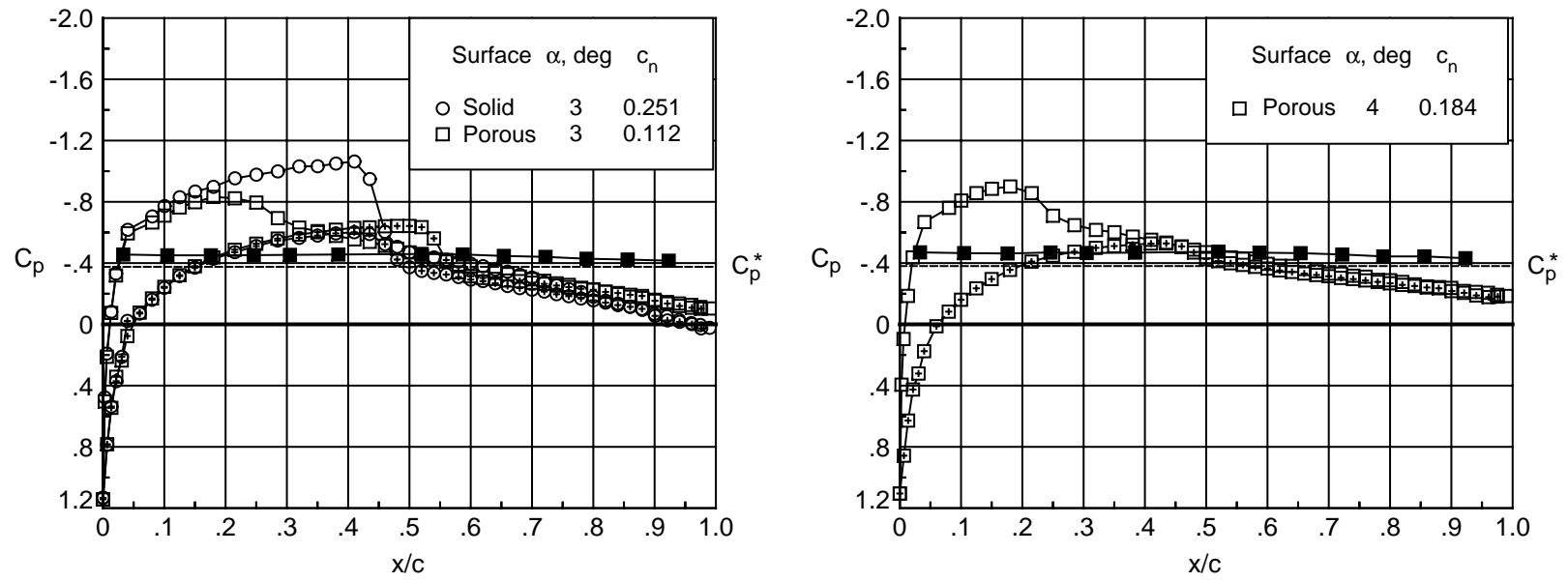
Figure 19. Concluded.
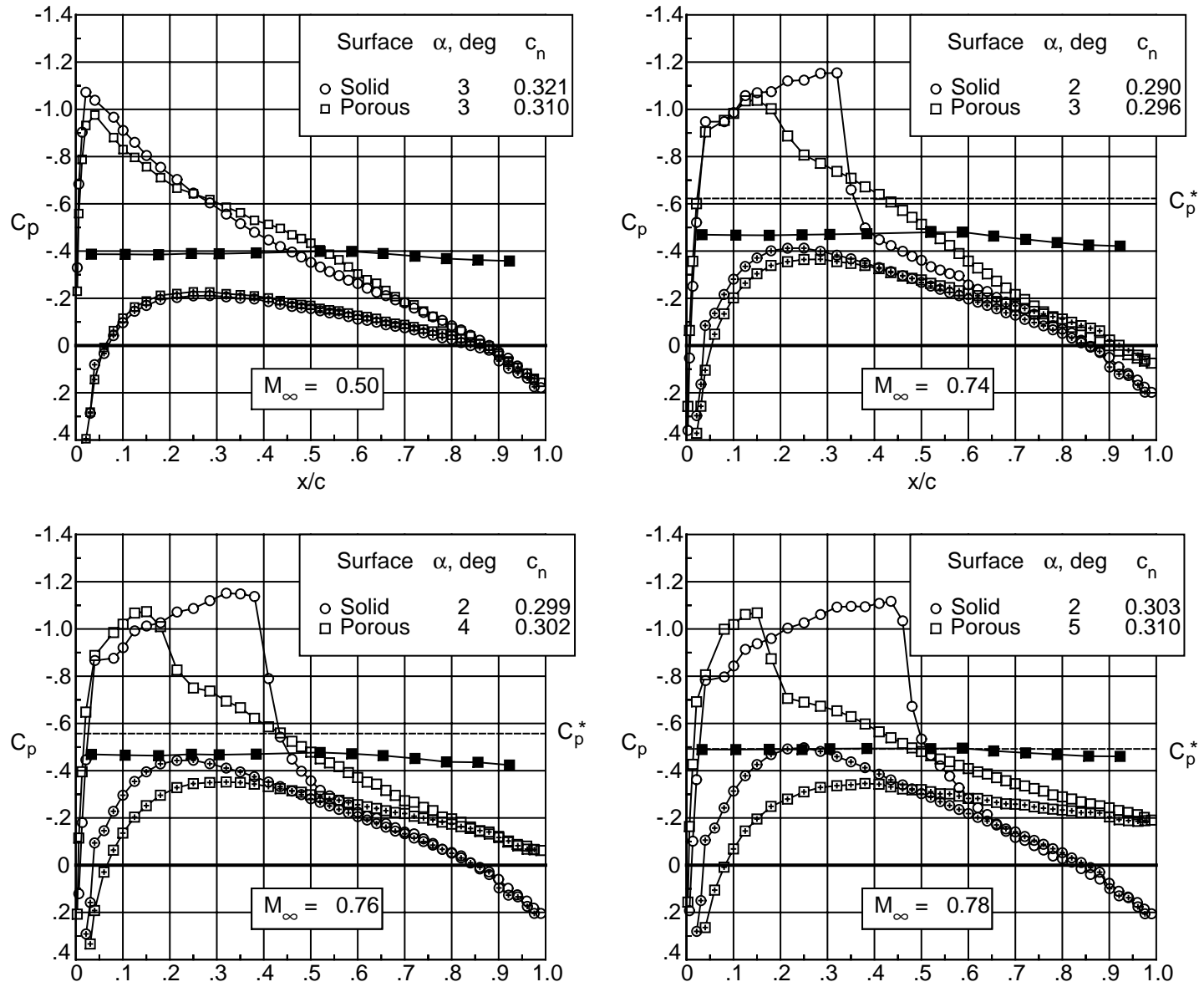
Figure 20. Effect of porosity on chordwise surface pressure coefficient distributions. $c_n \approx 0.3$; $R_c = 4 \times 10^6$. Open symbol denotes upper surface, '+' in symbol denotes lower surface, and solid symbol denotes cavity.
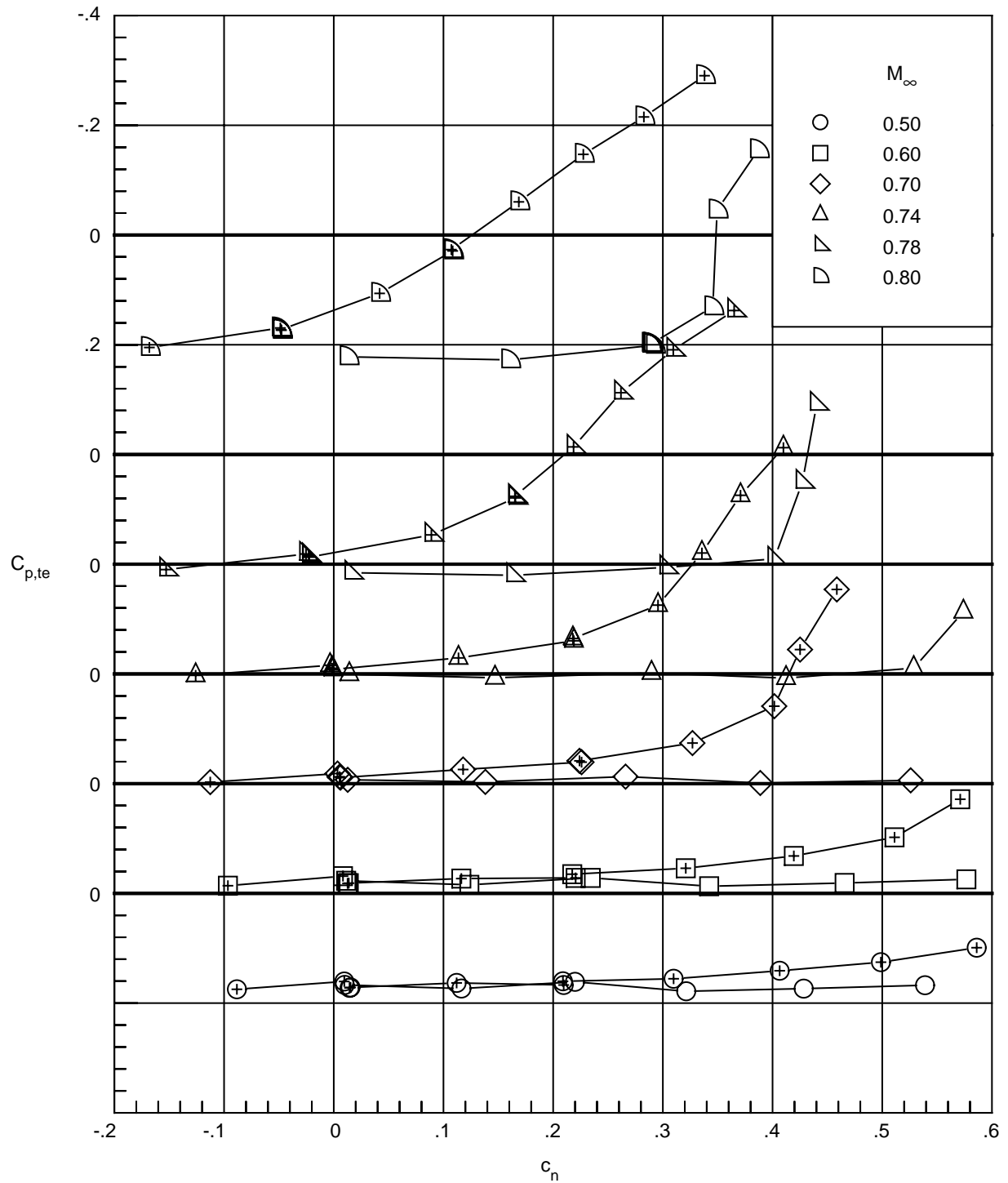
Figure 21. Effect of porosity on upper surface pressure coefficient near trailing edge. $R_c = 4 \times 10^6$. Open symbol denotes solid upper surface and '+' in symbol denotes porous upper surface.
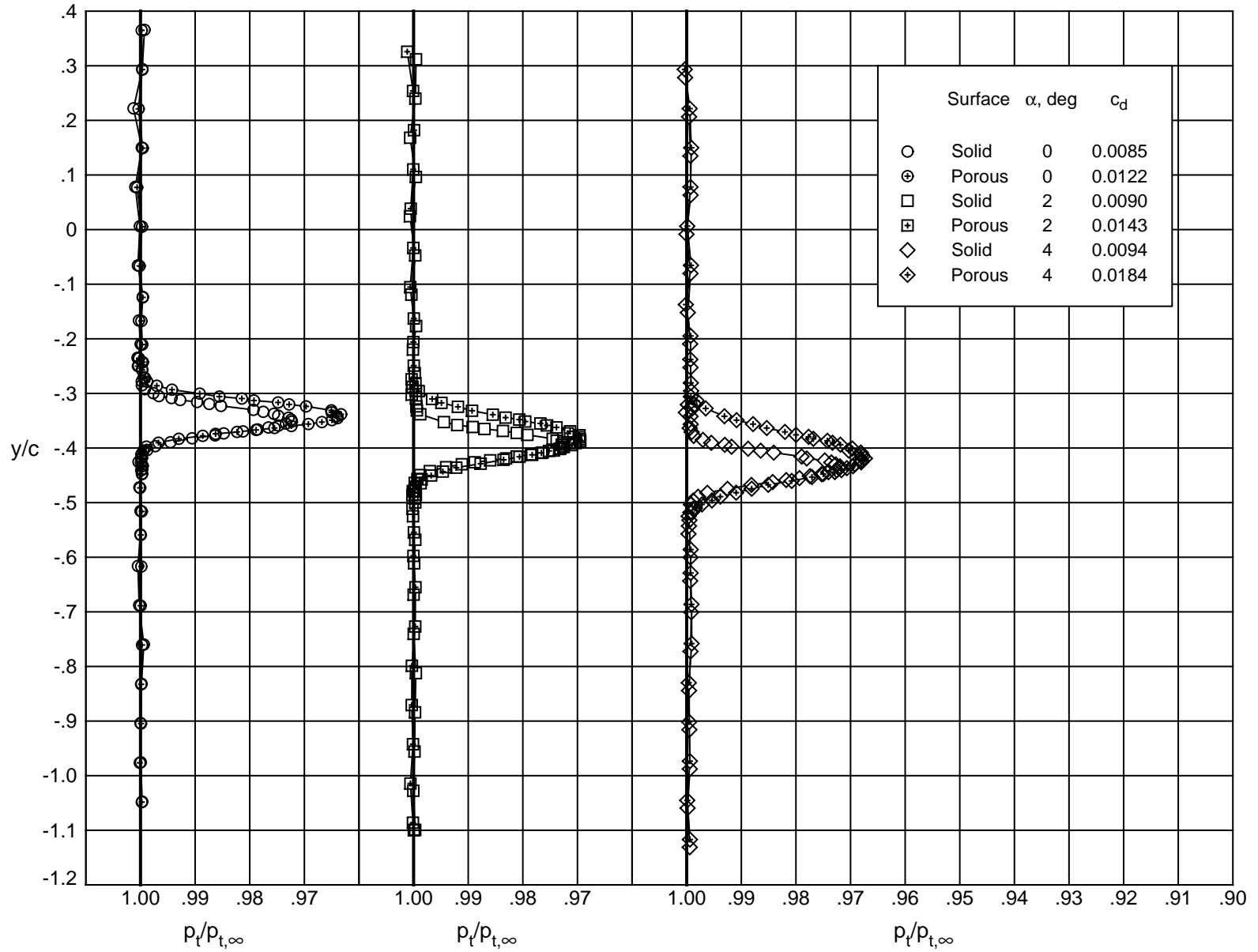
(a) $M_\infty = 0.50$.

Figure 22. Effect of porosity on total pressure profiles in airfoil wake. $R_c = 4 \times 10^6$.

Surface	α, deg	c_d
○ Solid	0	0.0087
⊕ Porous	0	0.0129
□ Solid	2	0.0092
⊞ Porous	2	0.0154
◇ Solid	4	0.0096
◈ Porous	4	0.0208

(b) $M_\infty = 0.60$.

Figure 22. Continued.
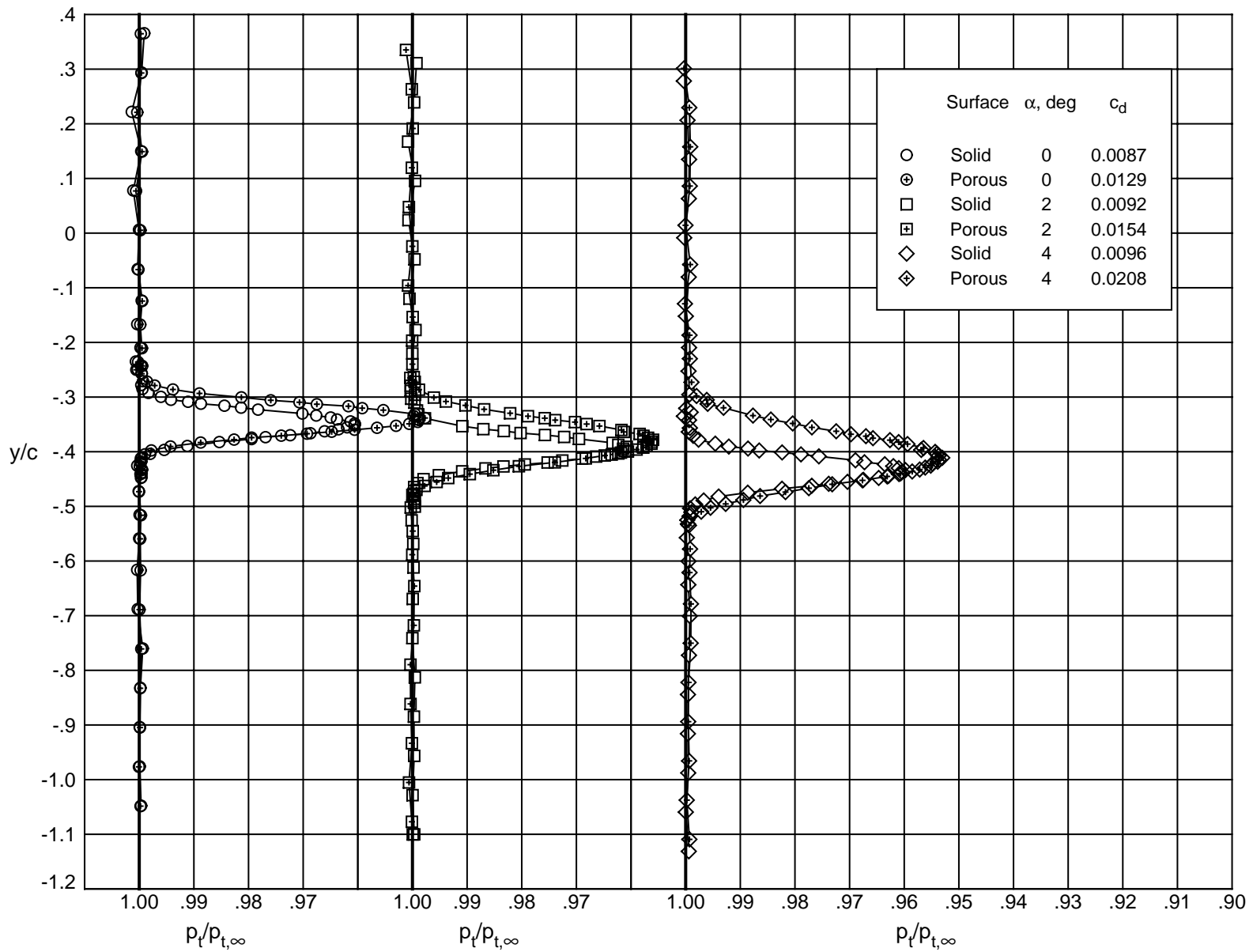
(c) $M_\infty = 0.70$.

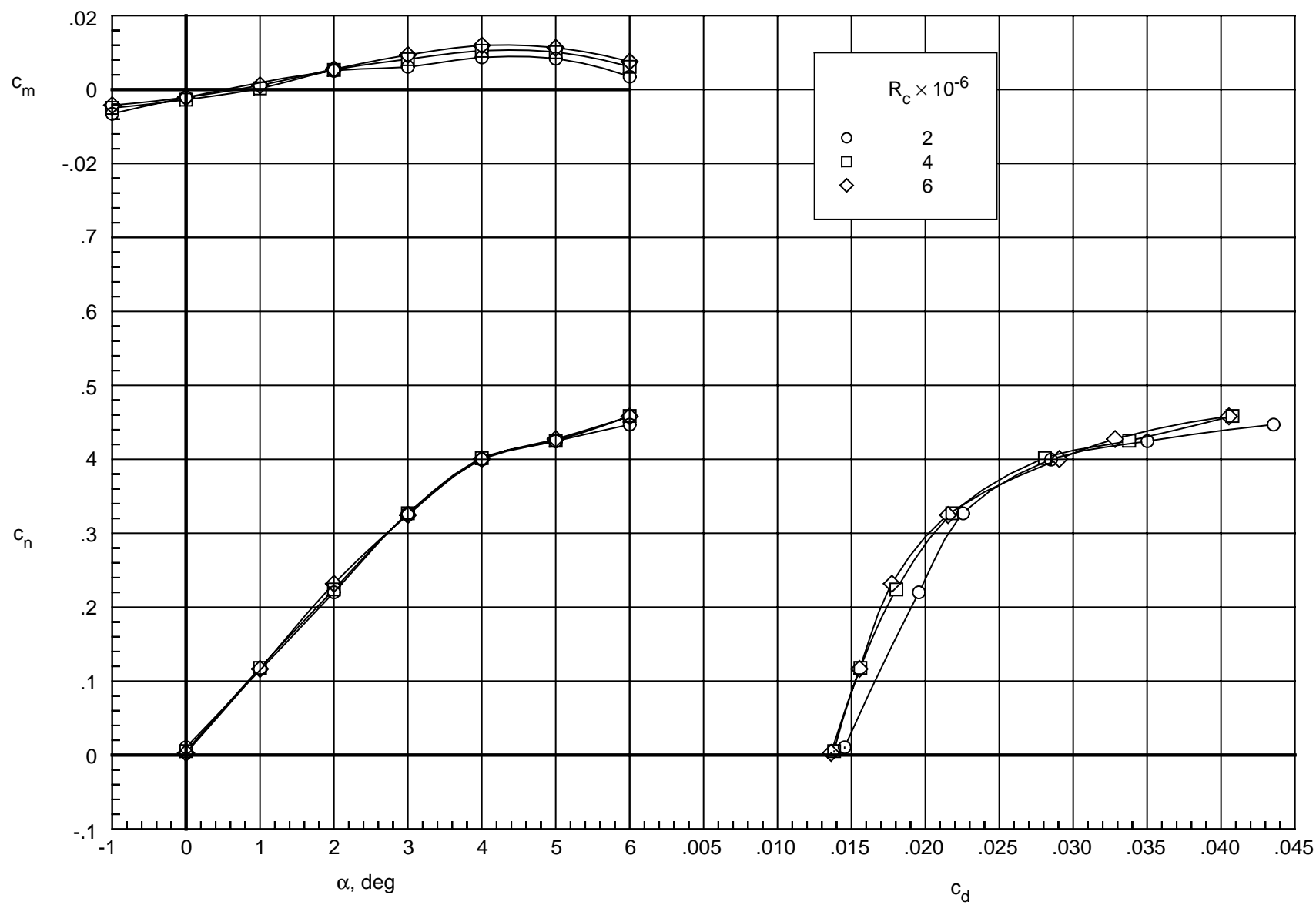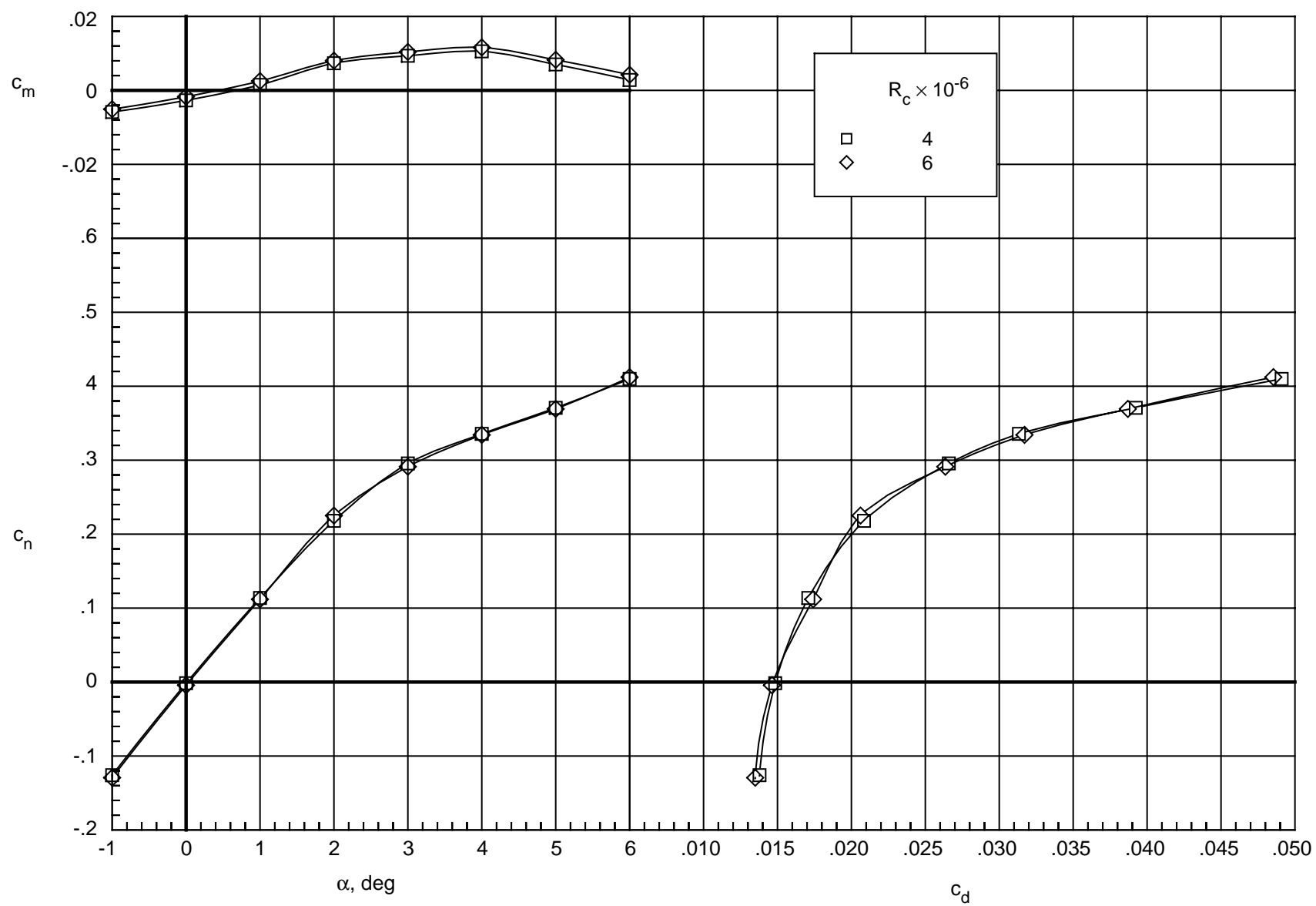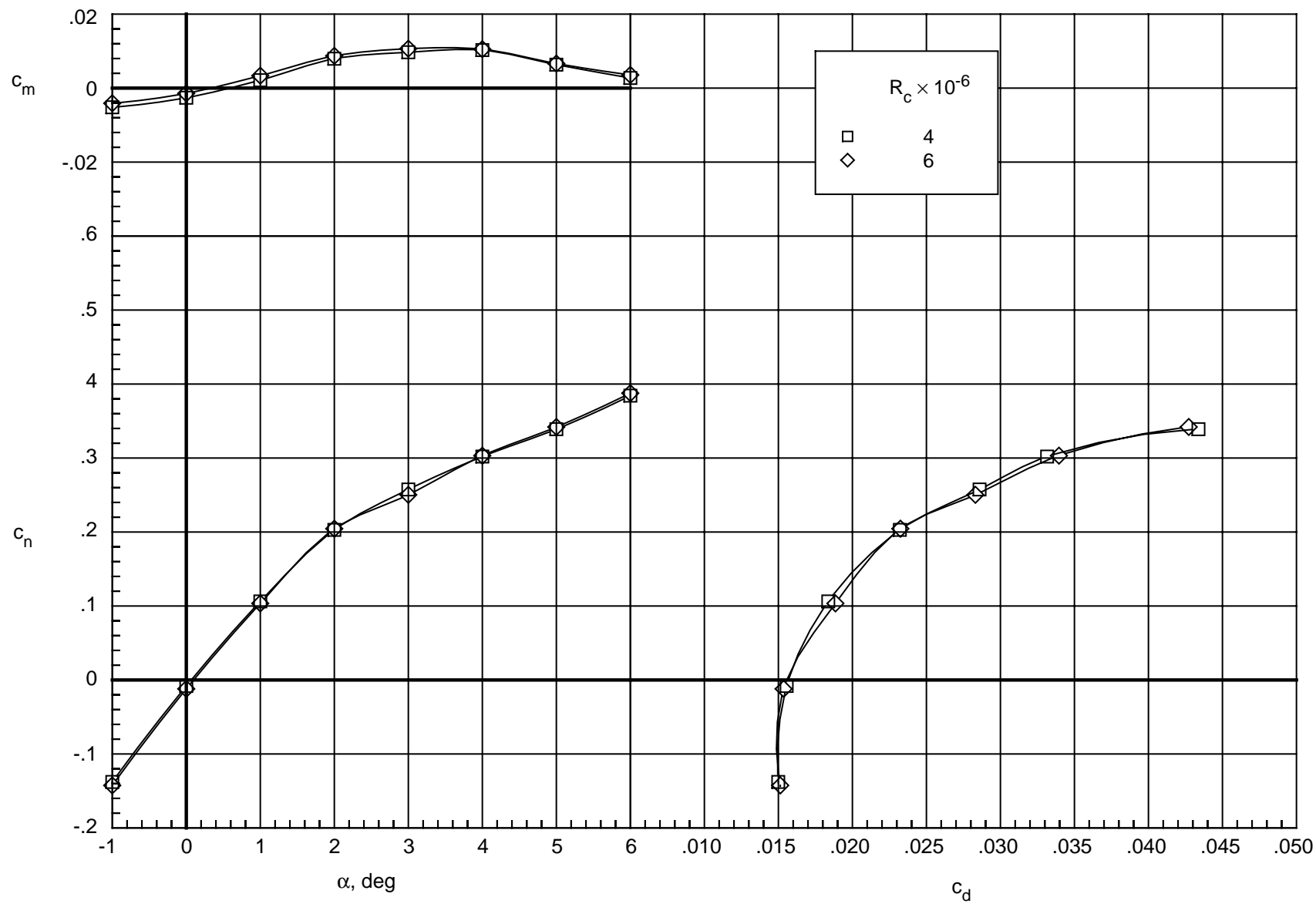Figure 22. Continued.
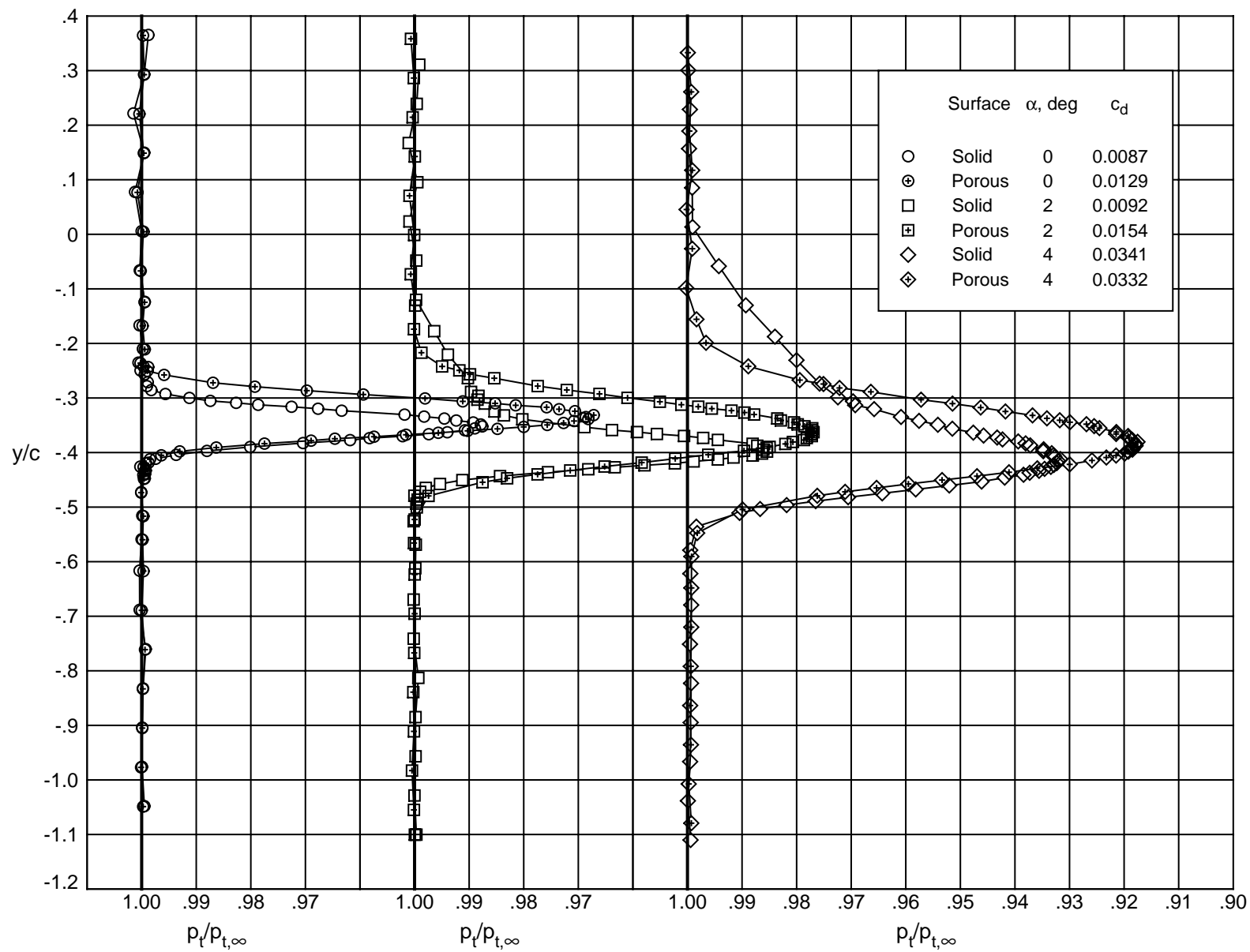
(d) $M_\infty = 0.76$.

Figure 22. Continued.
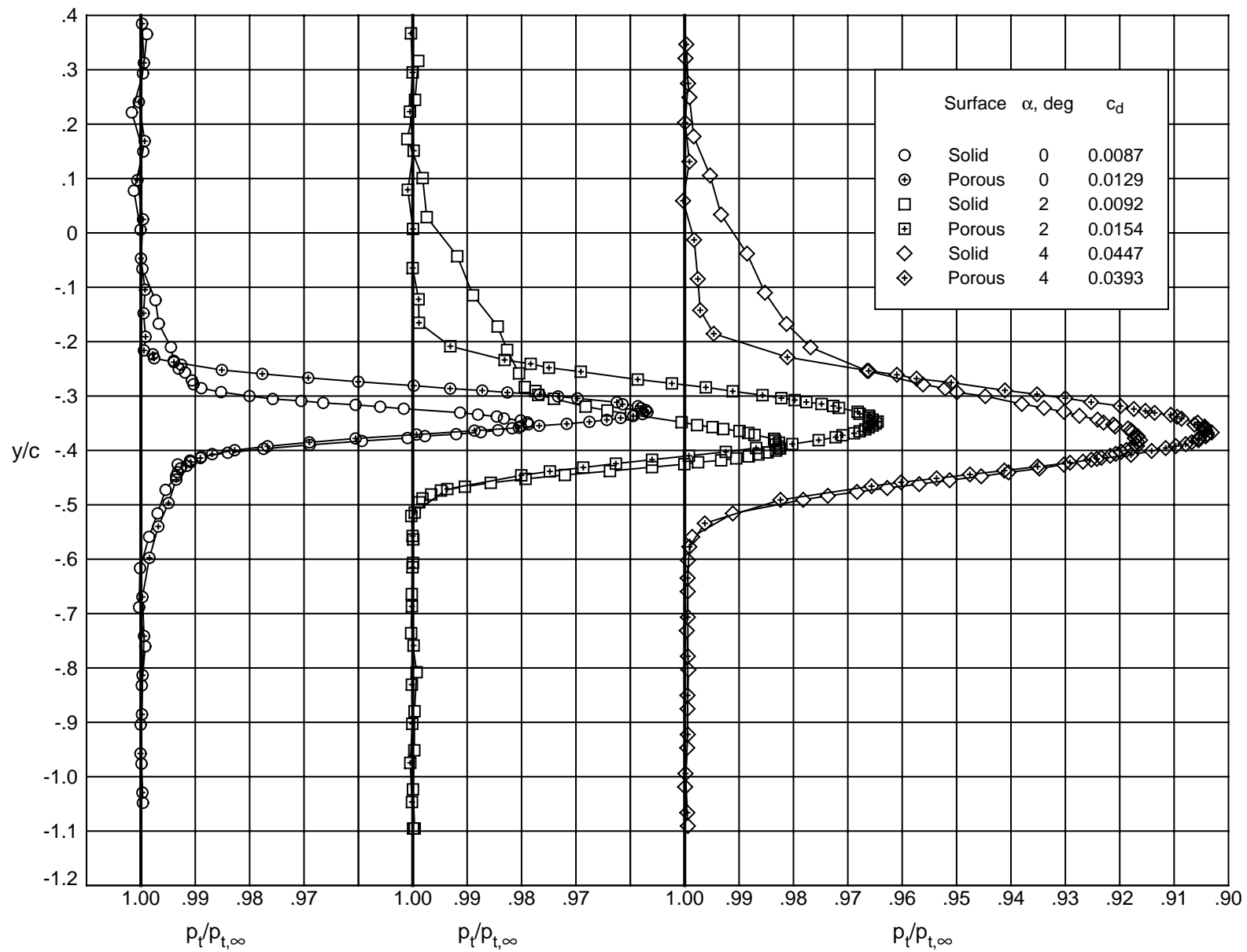
(e) $M_\infty = 0.80$.

Figure 22. Concluded.
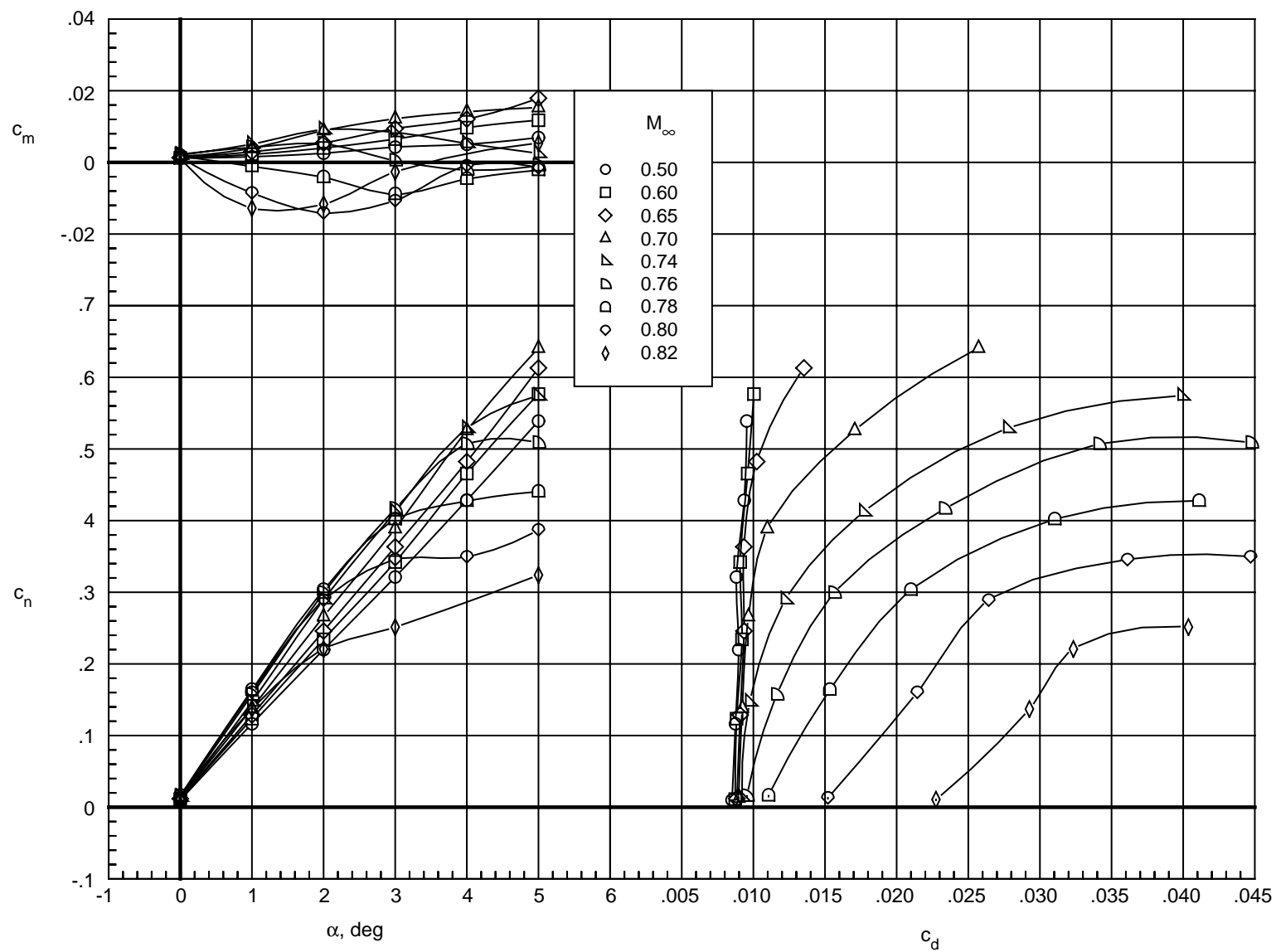
(a) Solid surface.

Figure 23. Effect of Mach number on integrated force and moment coefficients. $R_c = 4 \times 10^6$.
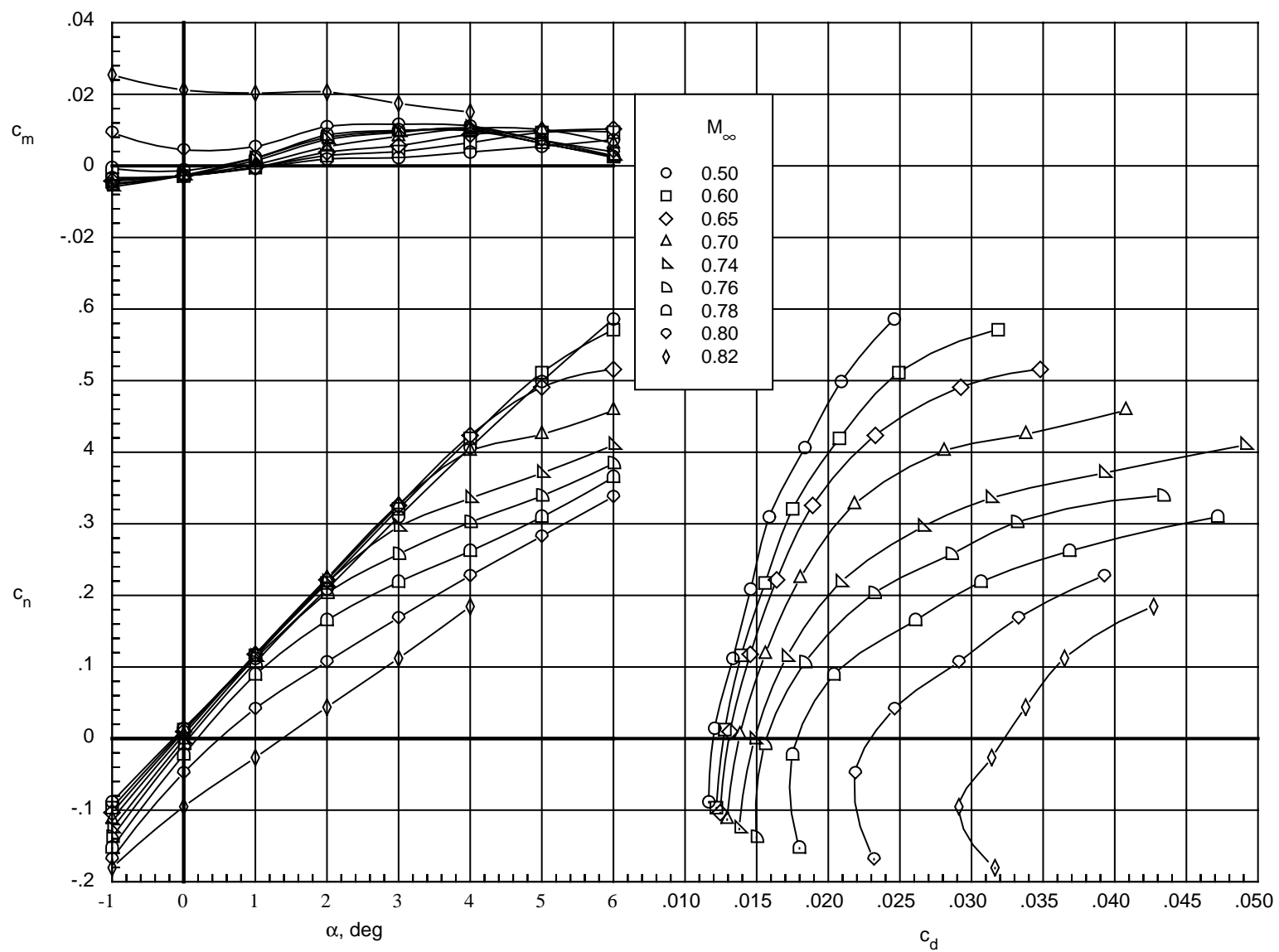
(b) Porous surface.

Figure 23. Concluded.
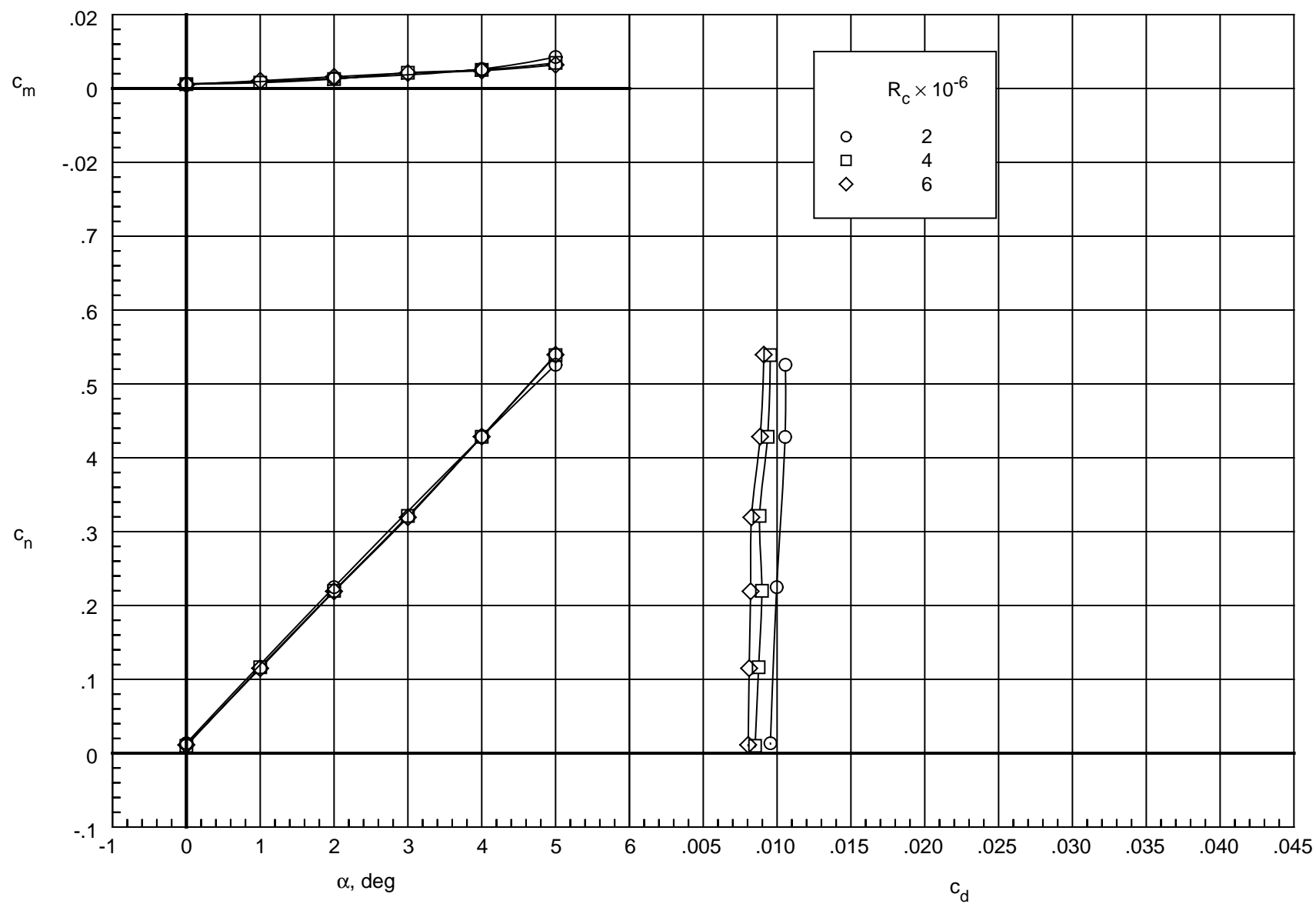
(a) $M_\infty = 0.50$.

Figure 24. Effect of Reynolds number on integrated force and moment coefficients for solid upper surface.
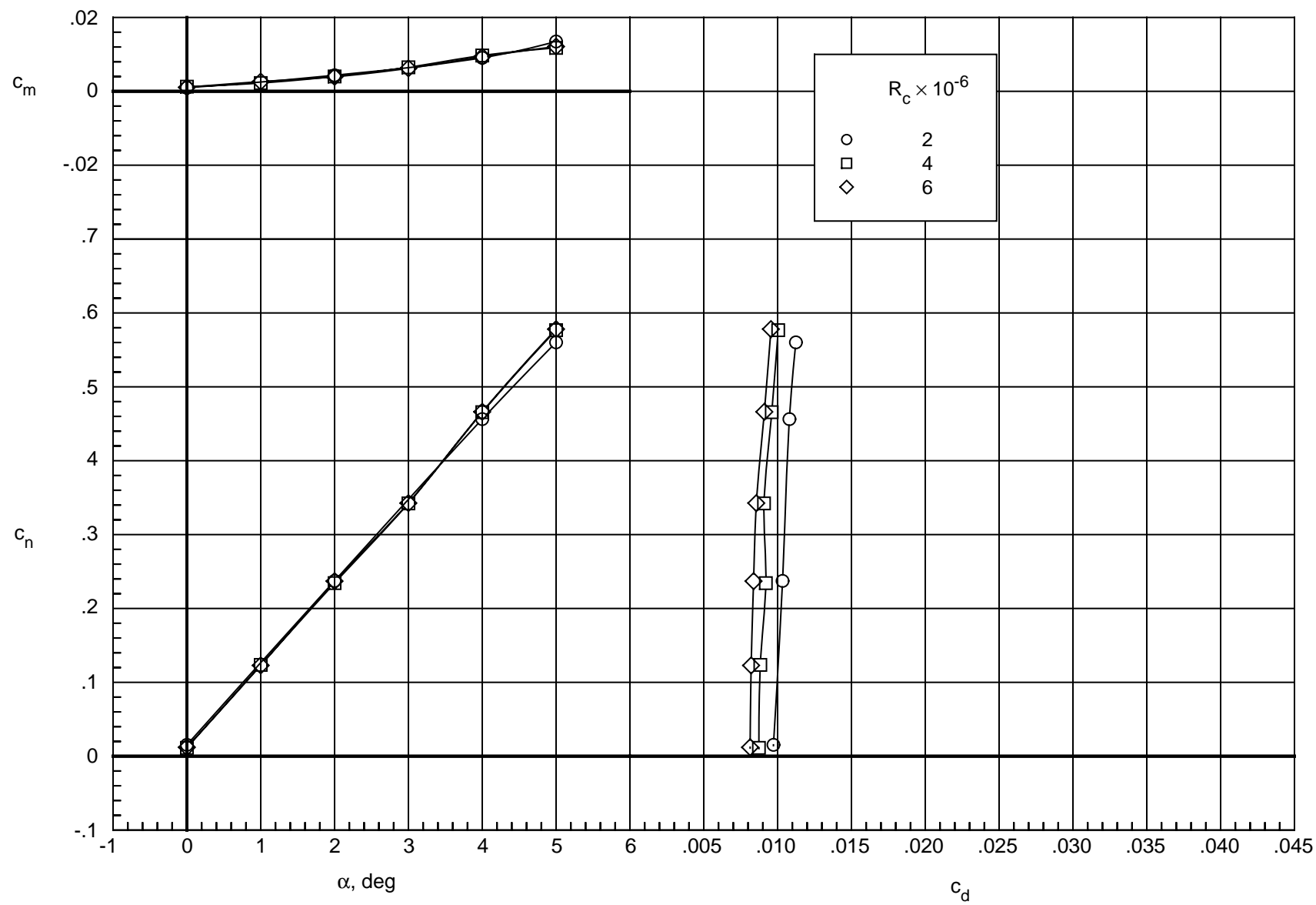
(b) $M_\infty = 0.60$.

Figure 24. Continued.
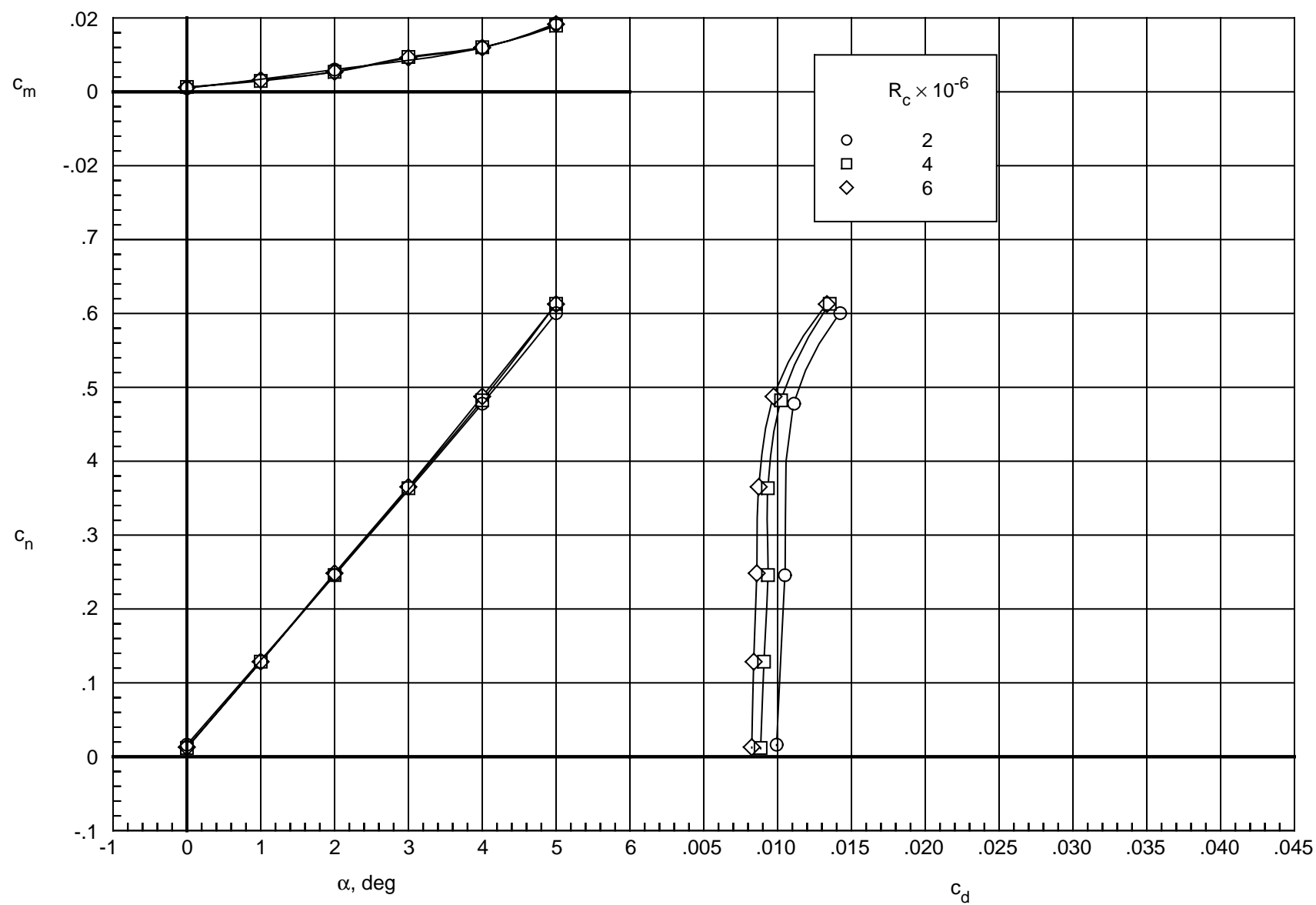
(c) $M_\infty = 0.65$.

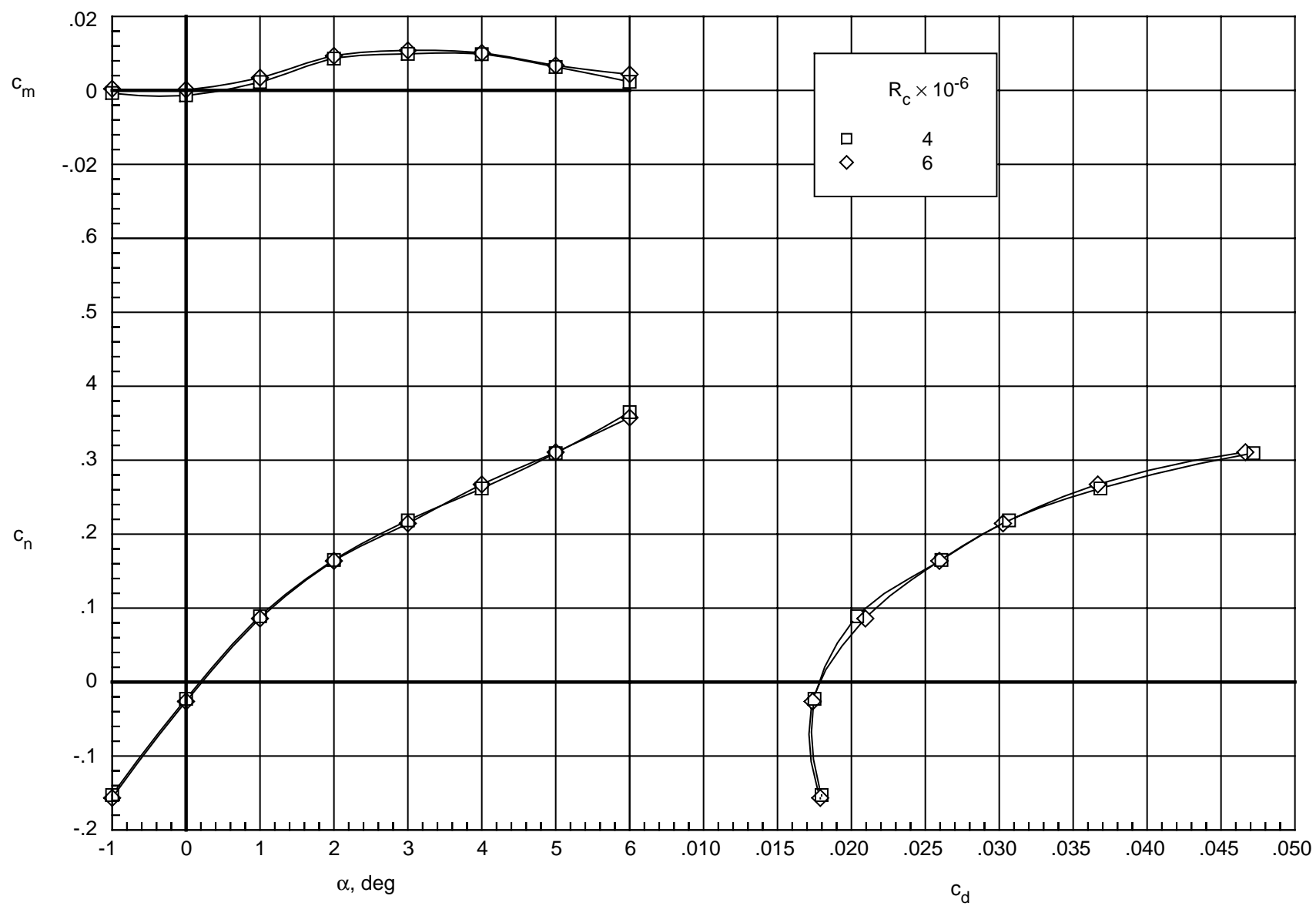Figure 24. Continued.
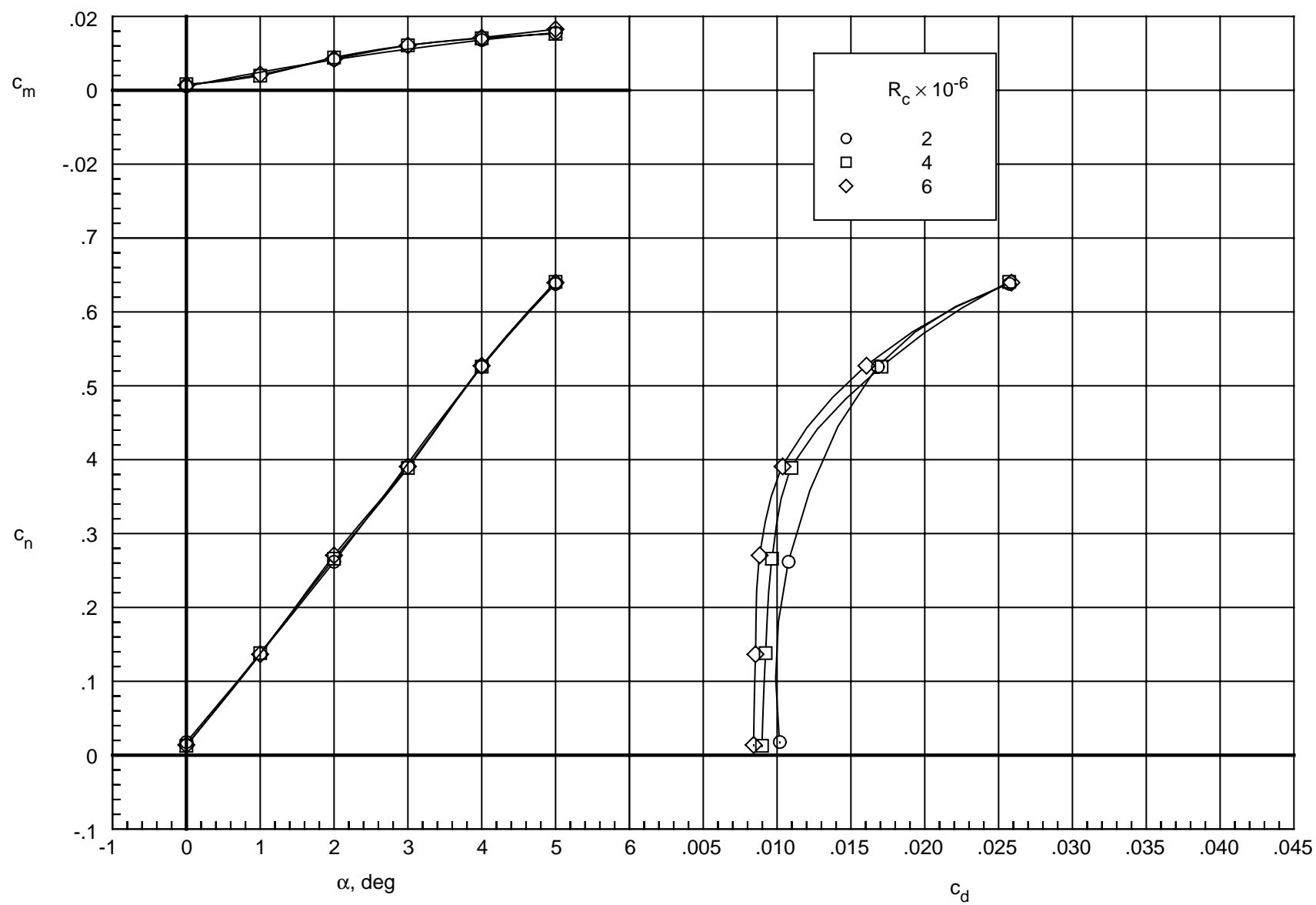
(d) $M_\infty = 0.70$.

Figure 24. Continued.
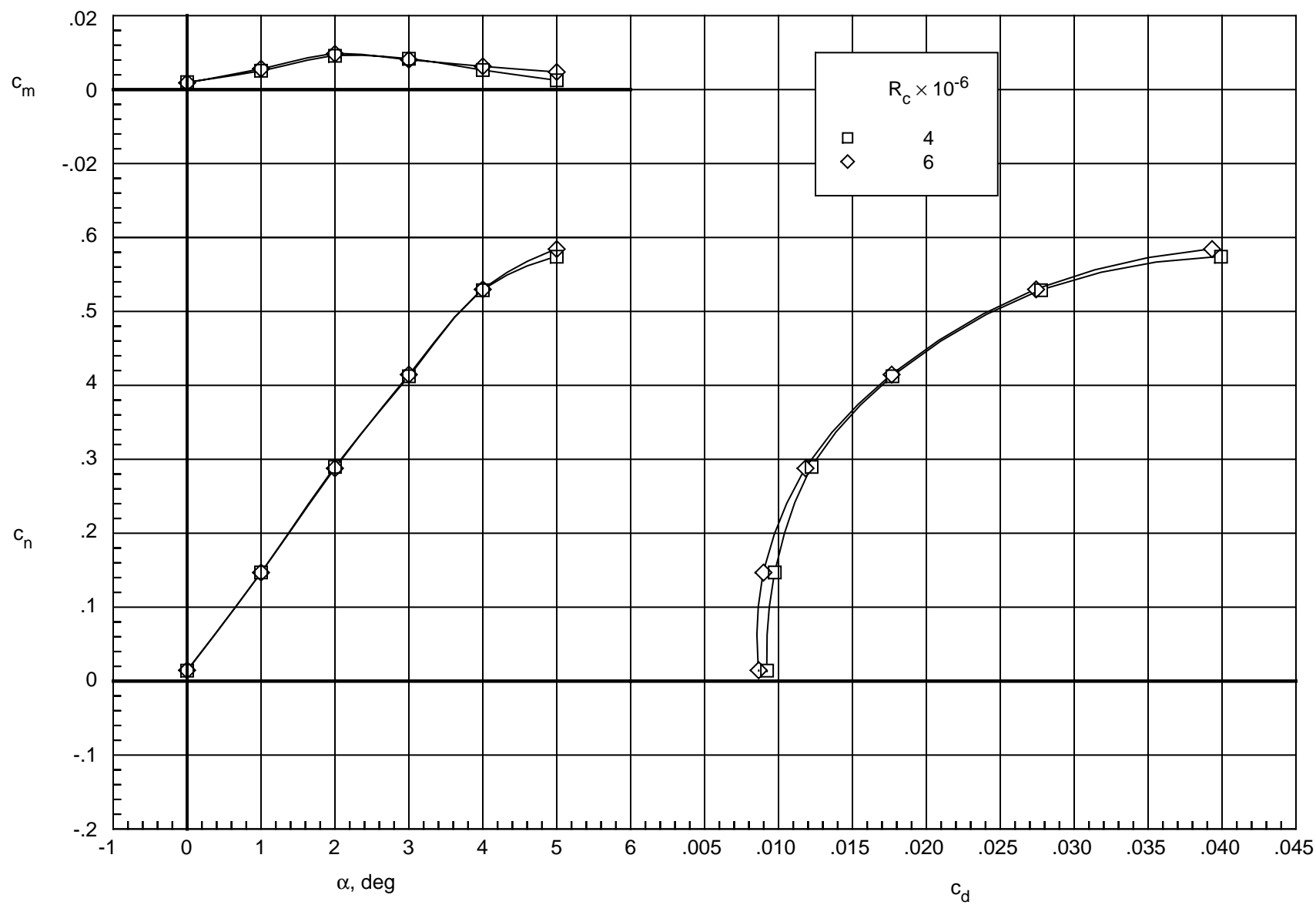
(e) $M_\infty = 0.74$.
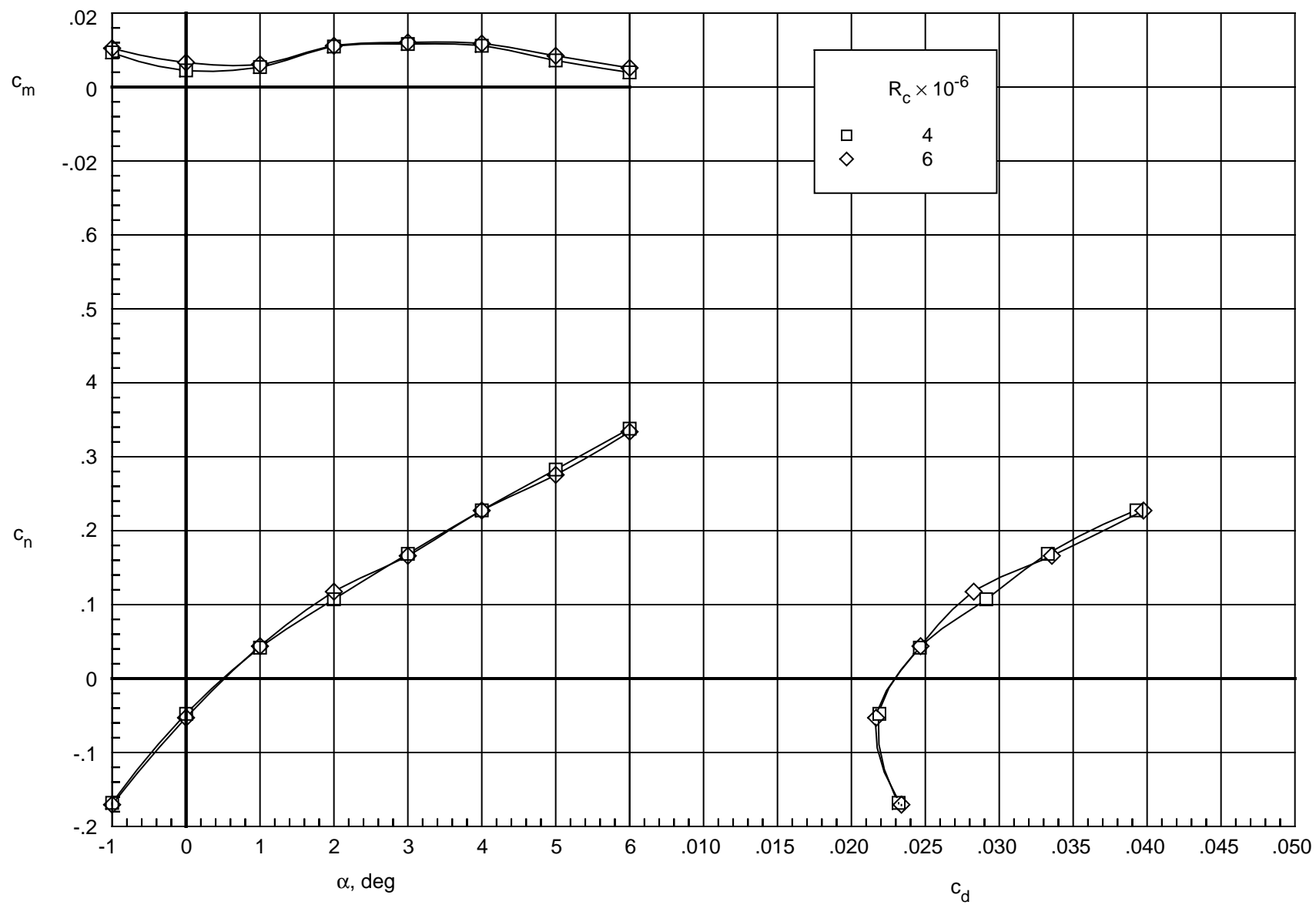
Figure 24. Continued.
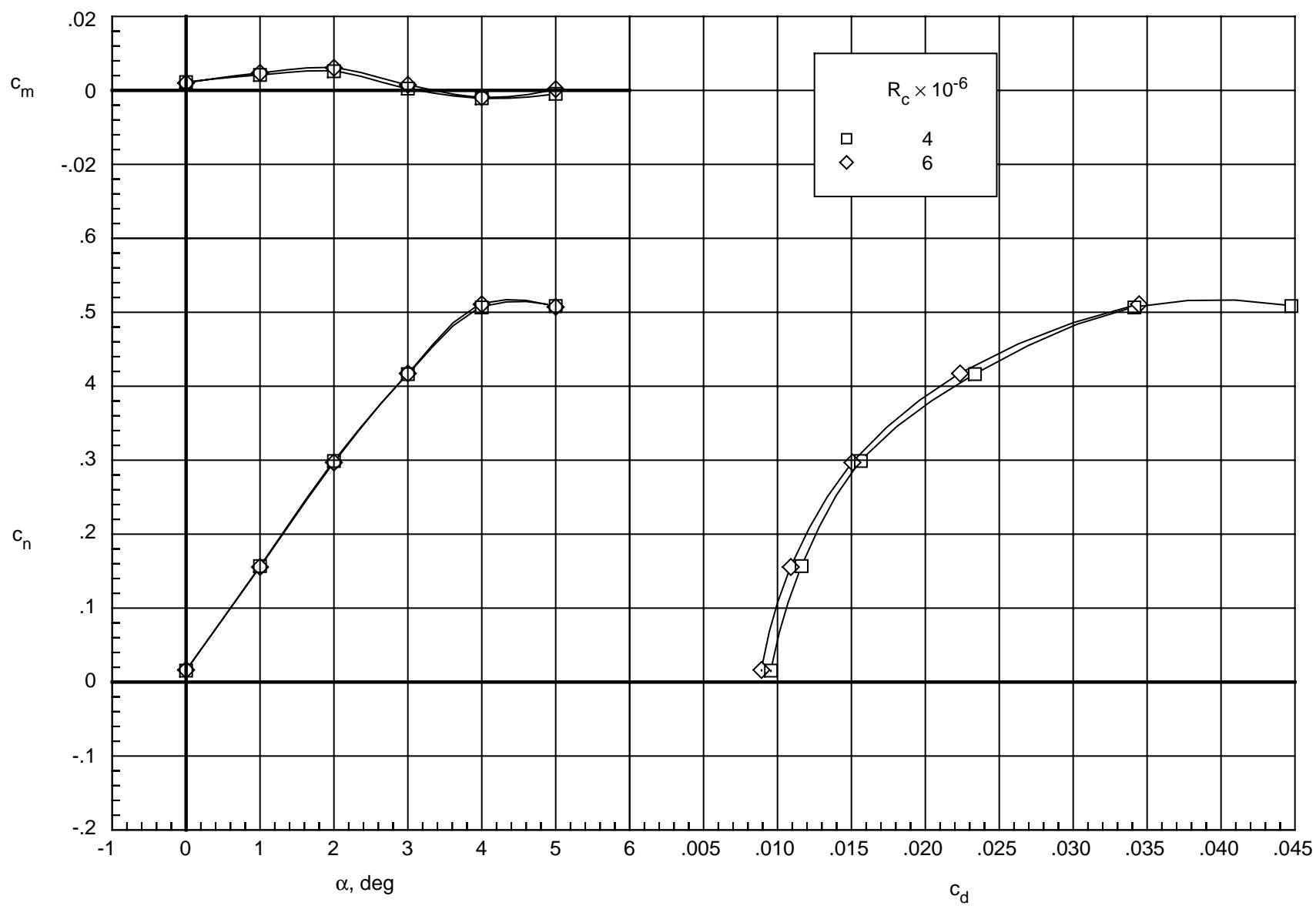
(f) $M_\infty = 0.76$.
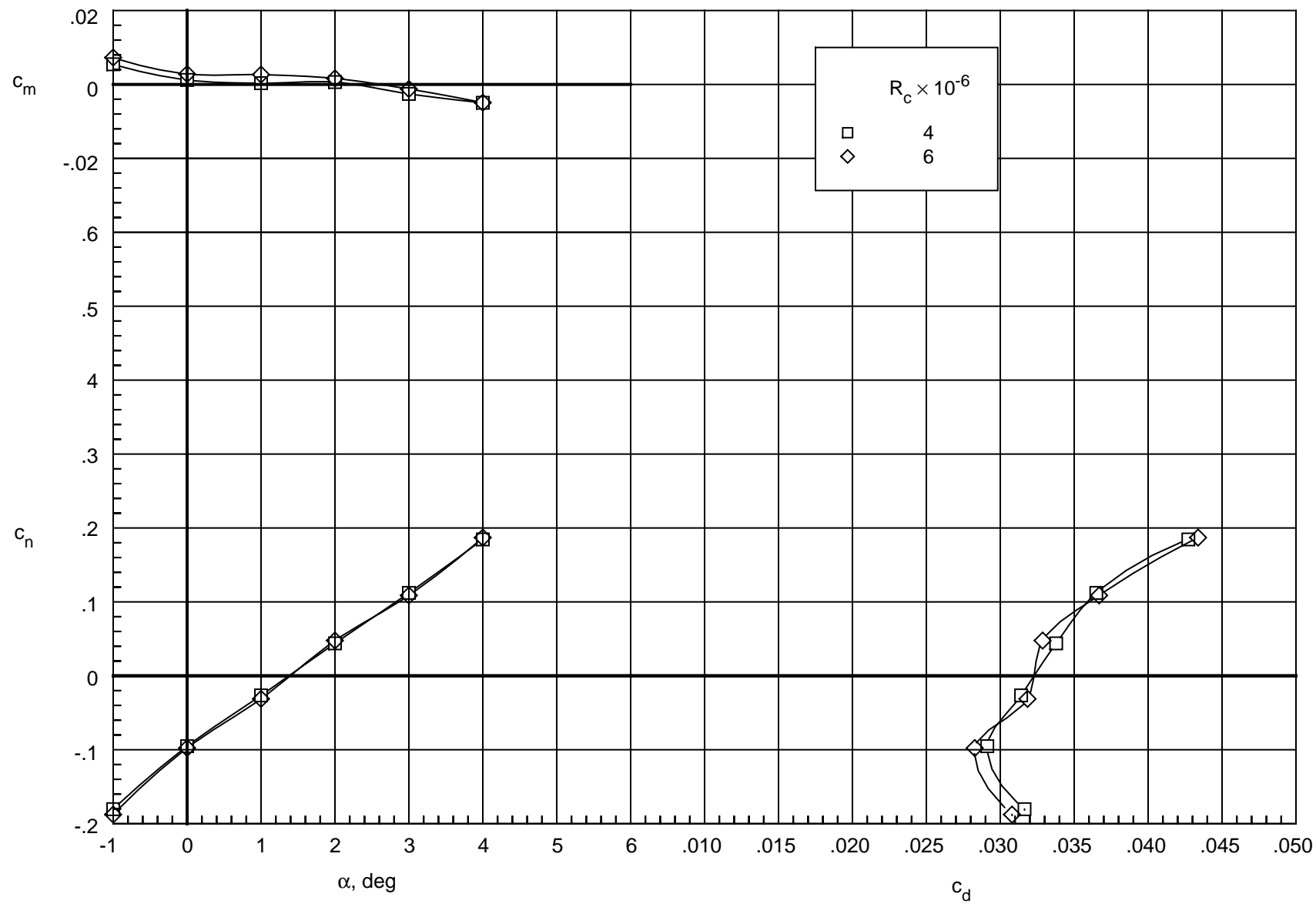
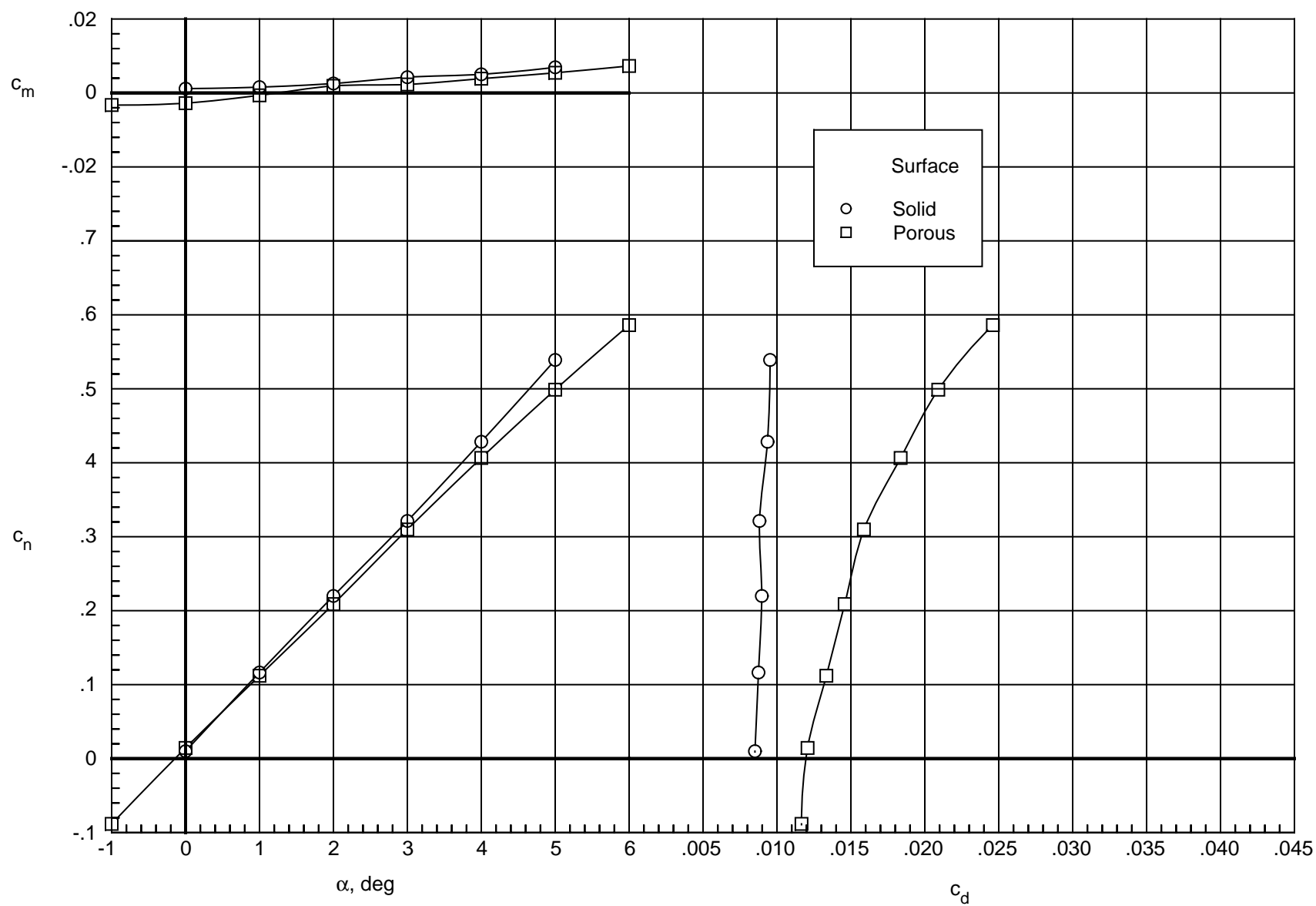Figure 24. Continued.
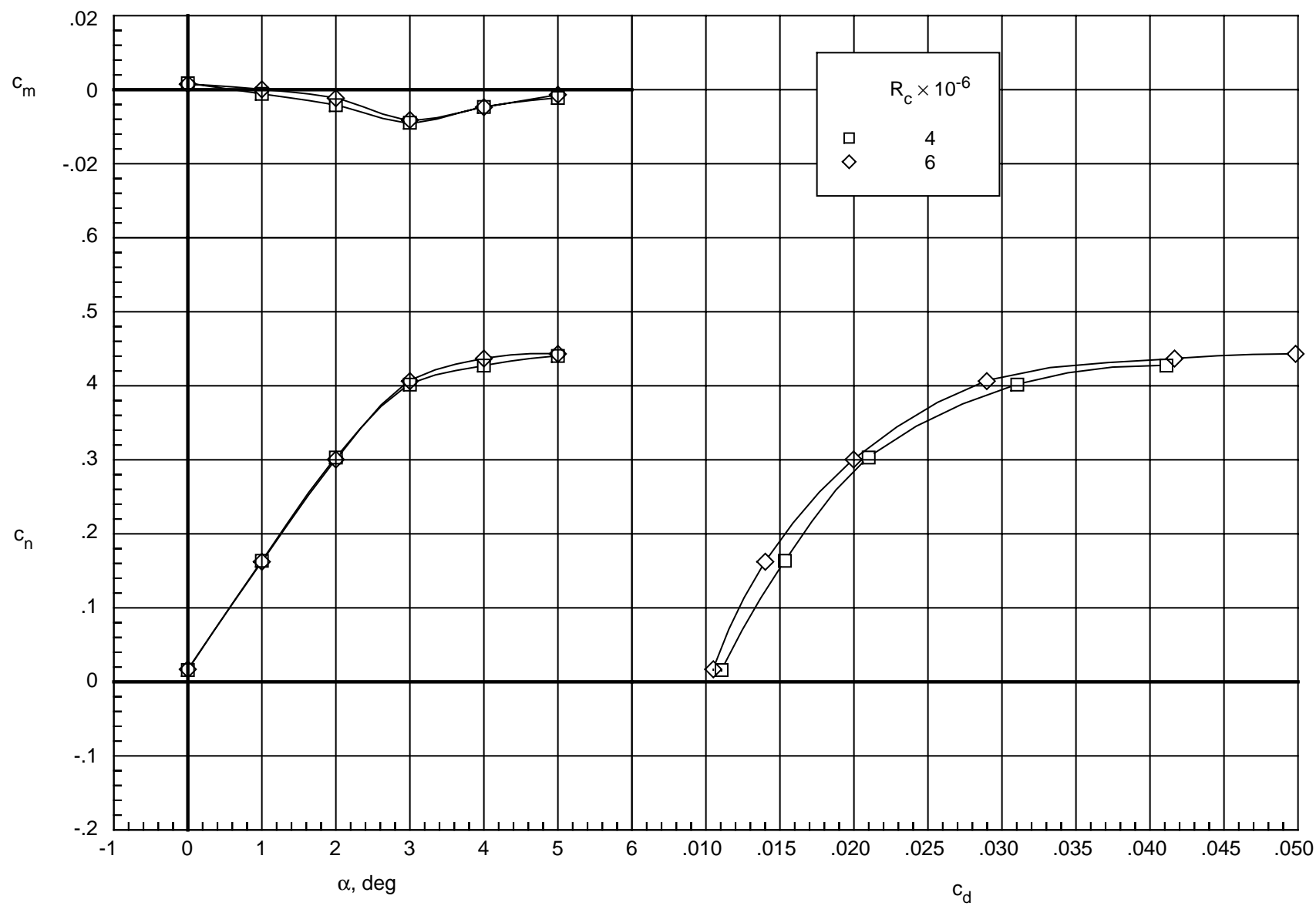
(g) $M_\infty = 0.78$.

Figure 24. Continued.
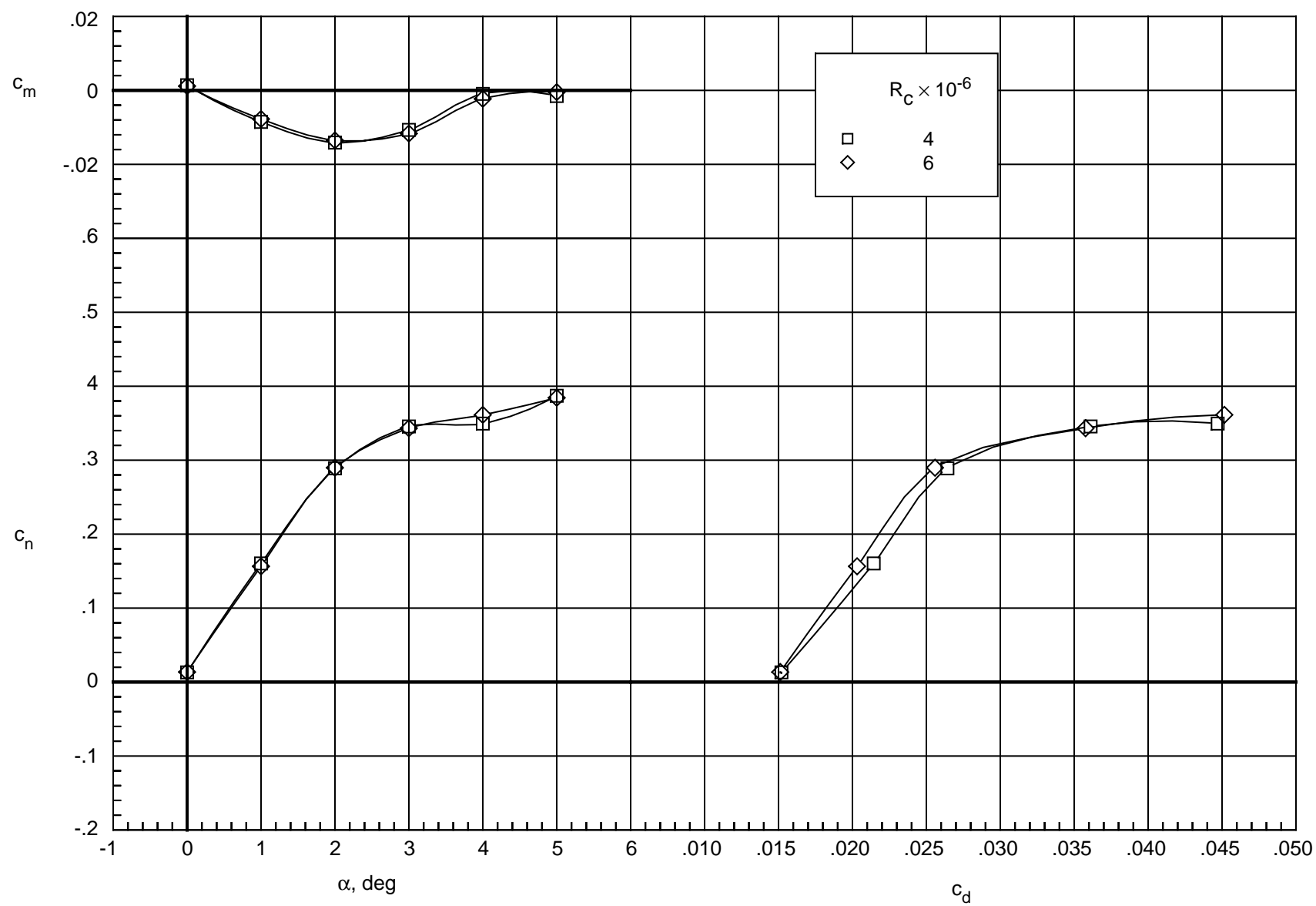
(h) $M_\infty = 0.80$.

Figure 24. Continued.
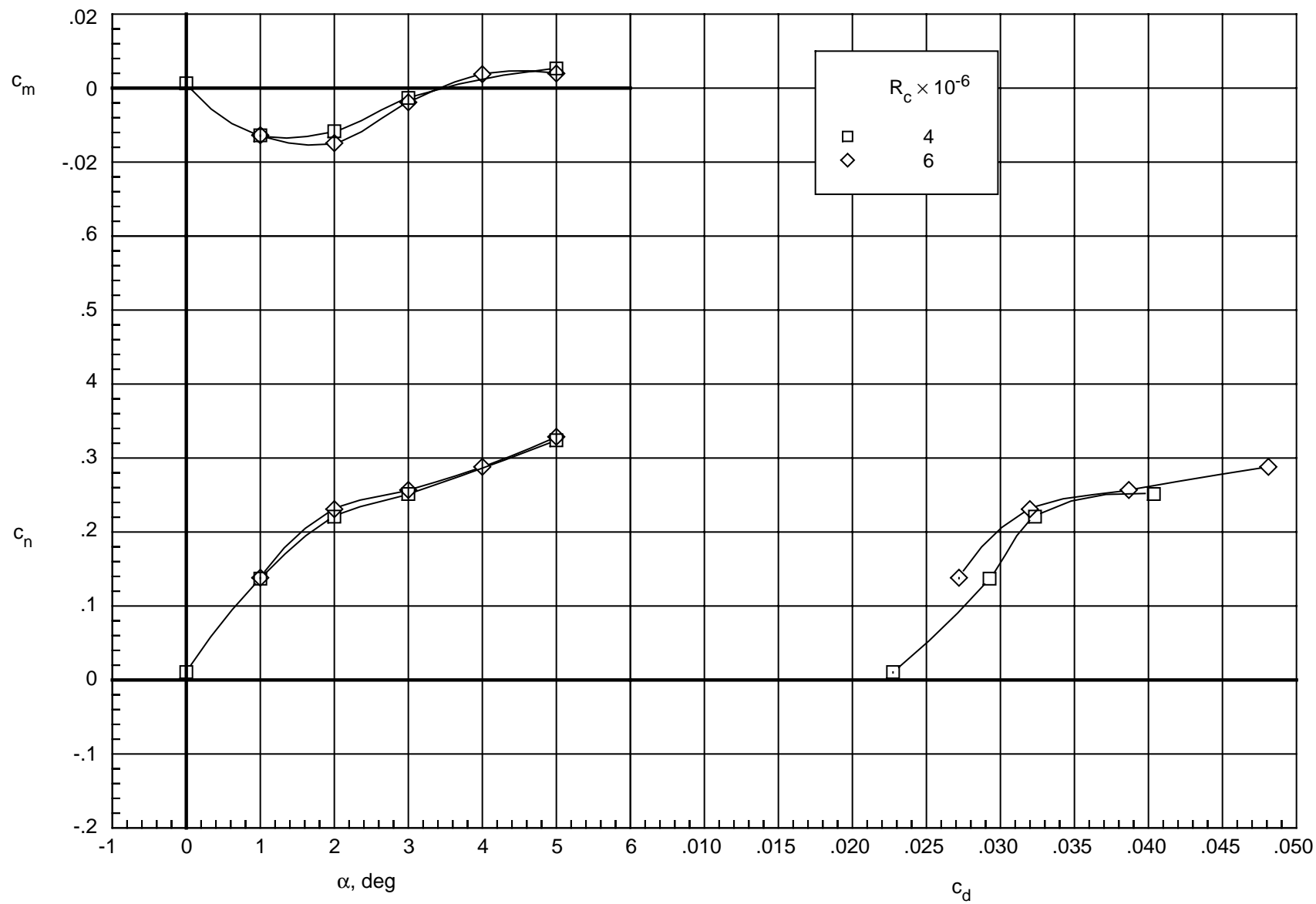
(i) $M_\infty = 0.82$.

Figure 24. Concluded.
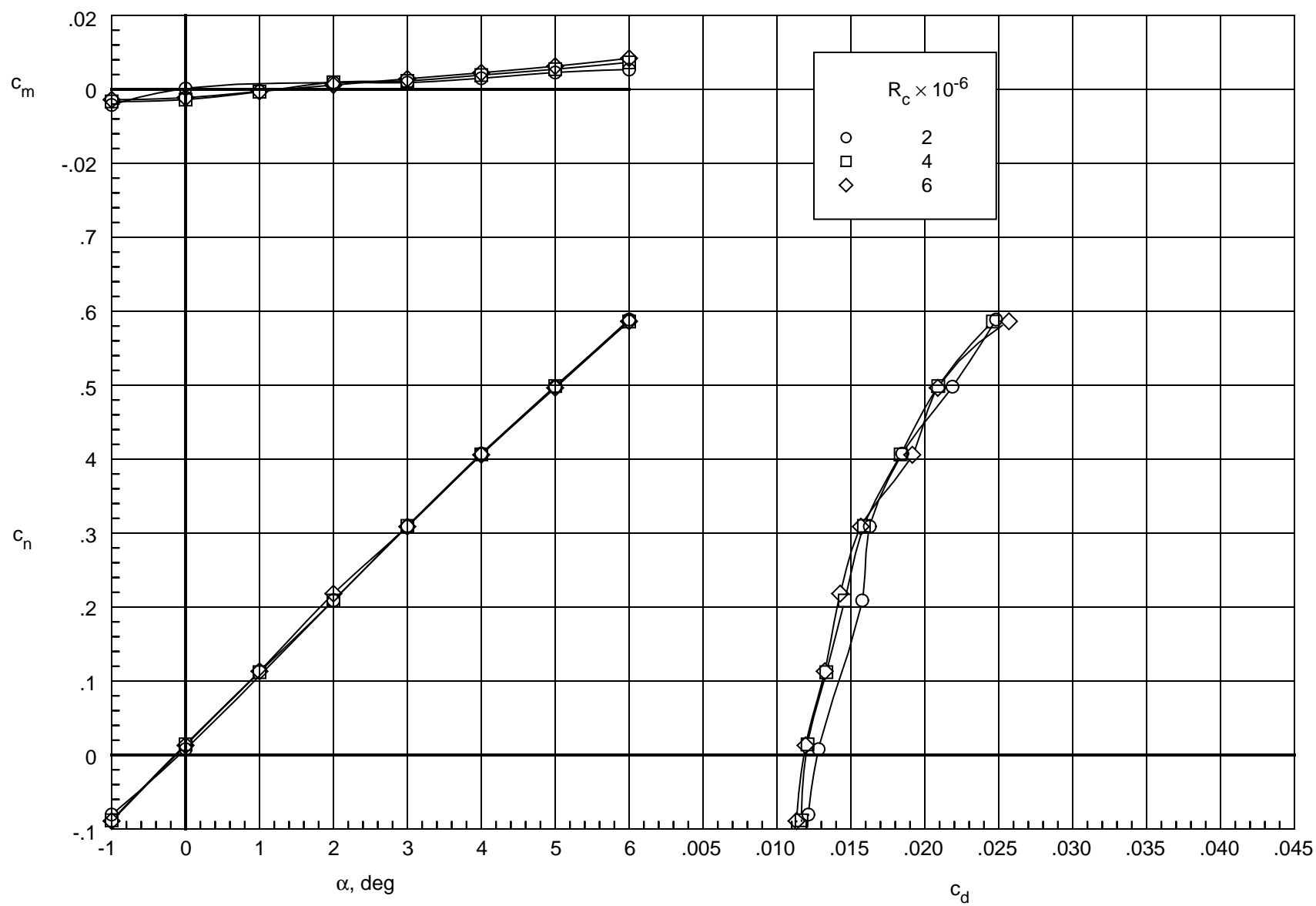
(a) $M_\infty = 0.50$.

Figure 25. Effect of Reynolds number on integrated force and moment coefficients for porous upper surface.
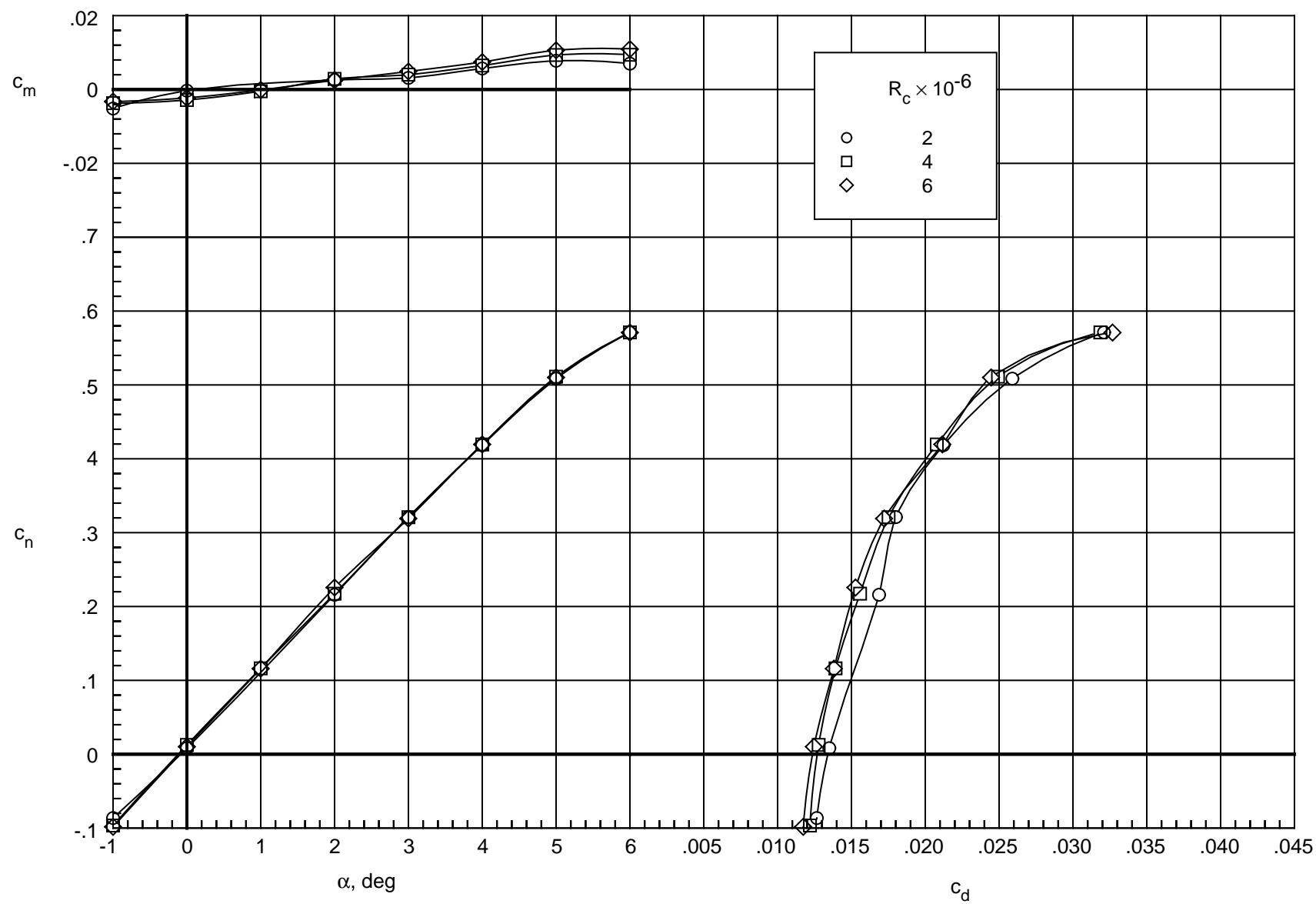
(b) $M_\infty = 0.60$.

Figure 25. Continued.
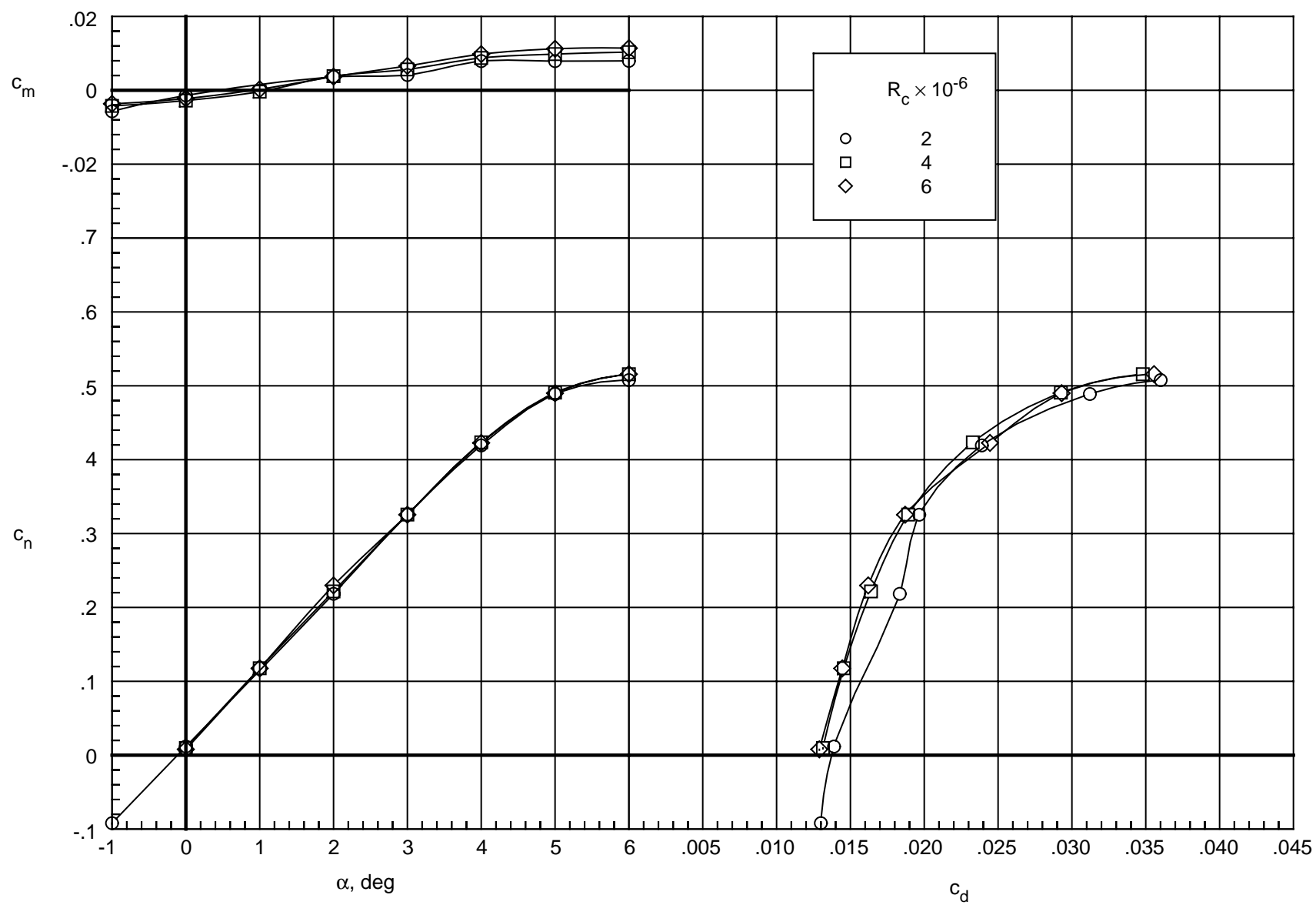
(c) $M_\infty = 0.65$.

Figure 25. Continued.

(d) $M_\infty = 0.70$.

Figure 25. Continued.

(e) $M_\infty = 0.74$.

Figure 25. Continued.

(f) $M_\infty = 0.76$.

Figure 25. Continued.

(g) $M_\infty = 0.78$.
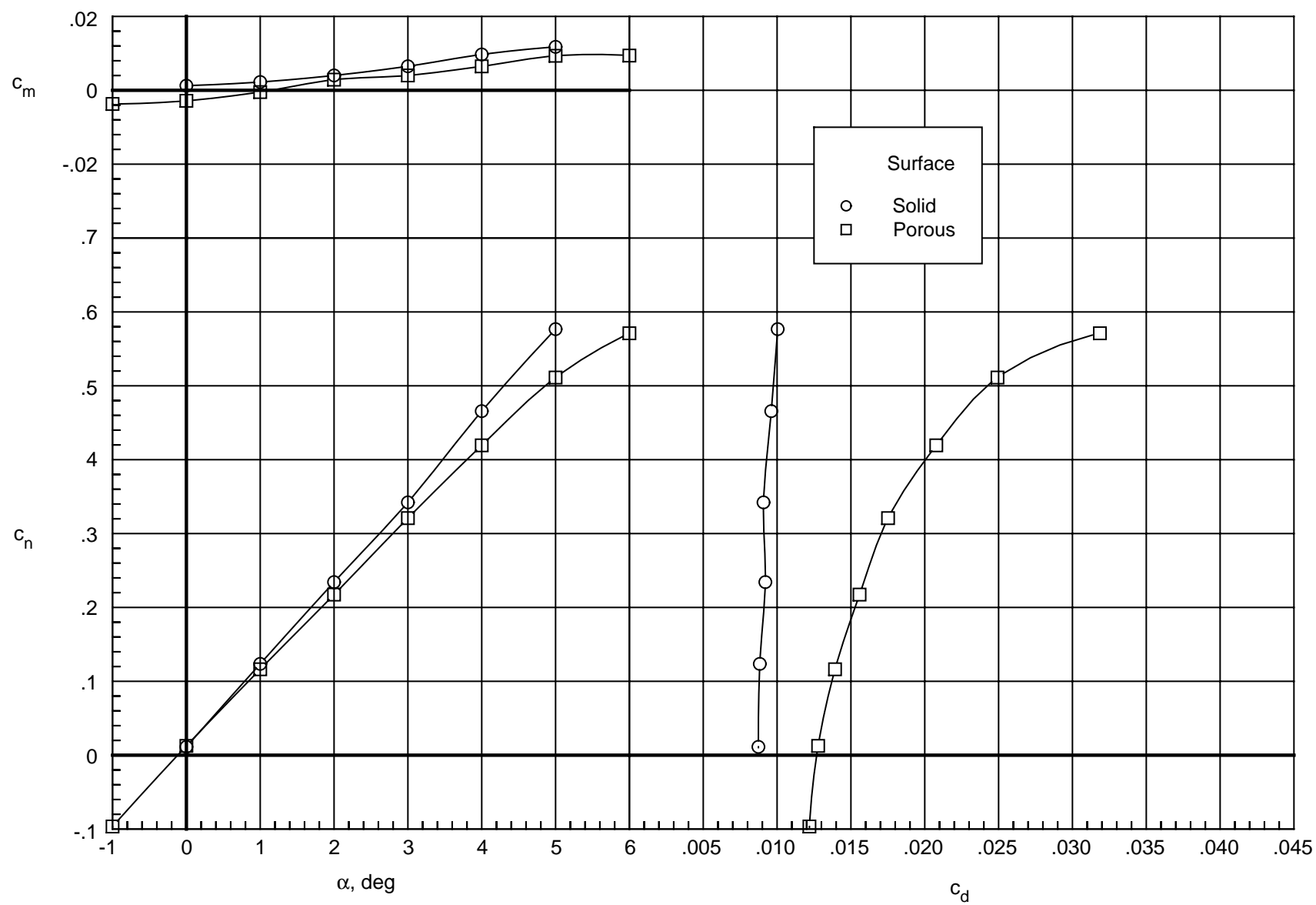
Figure 25. Continued.

(h) $M_\infty = 0.80$.

Figure 25. Continued.

(i) $M_\infty = 0.82$.

Figure 25. Concluded.

(a) $M_\infty = 0.50$.

Figure 26. Effect of porosity on integrated force and moment coefficients. $R_c = 4 \times 10^6$.
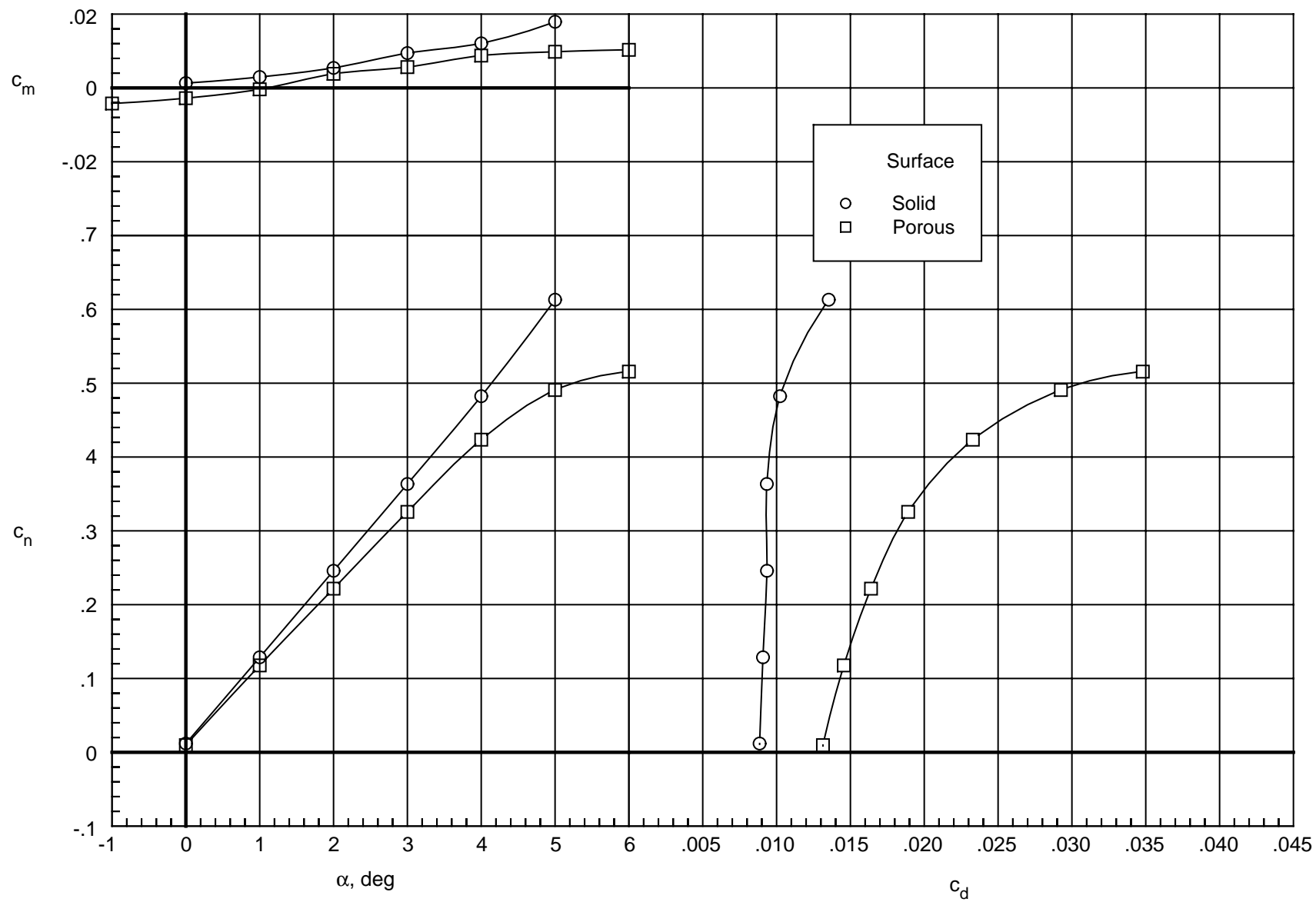
(b) $M_\infty = 0.60$.
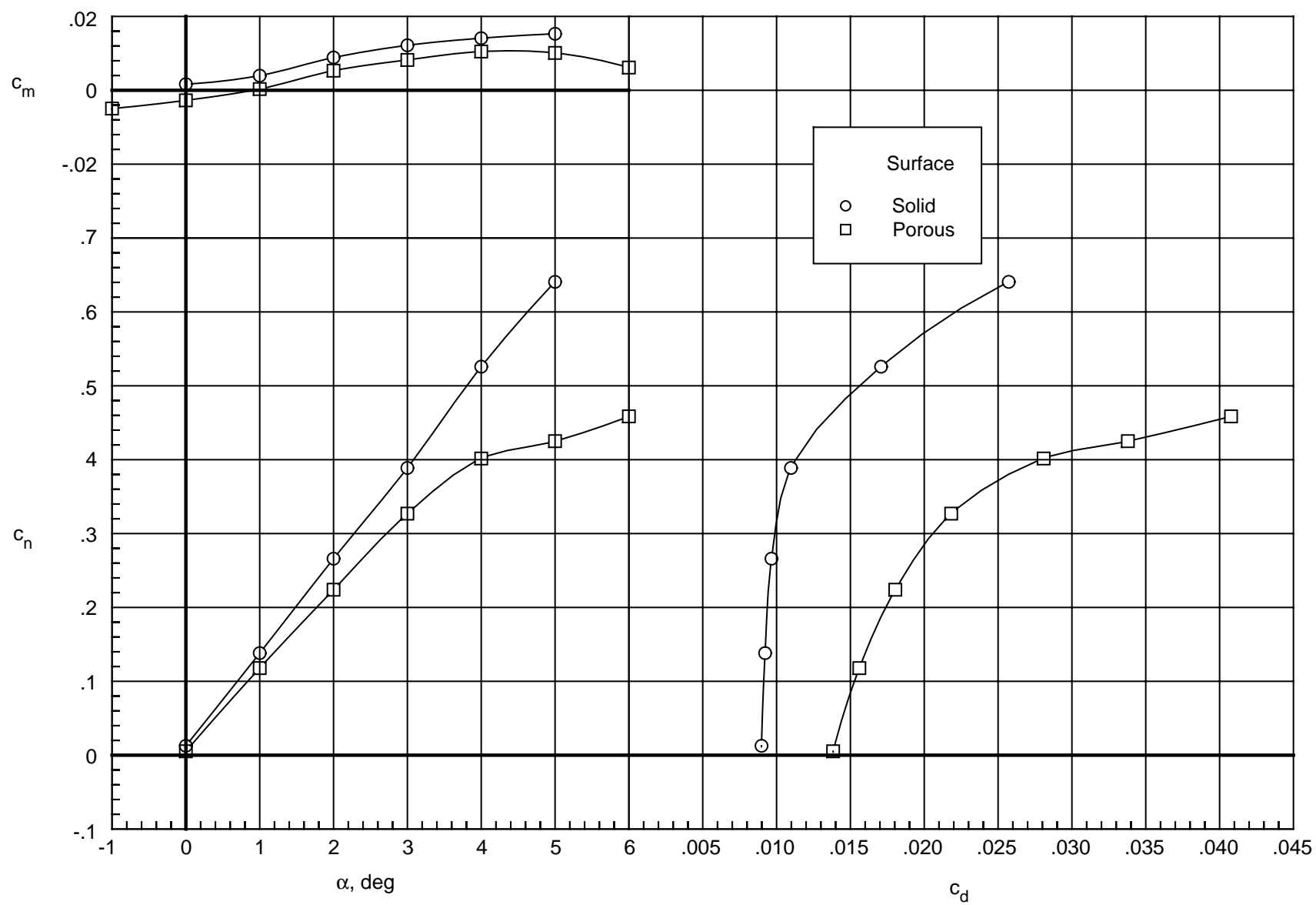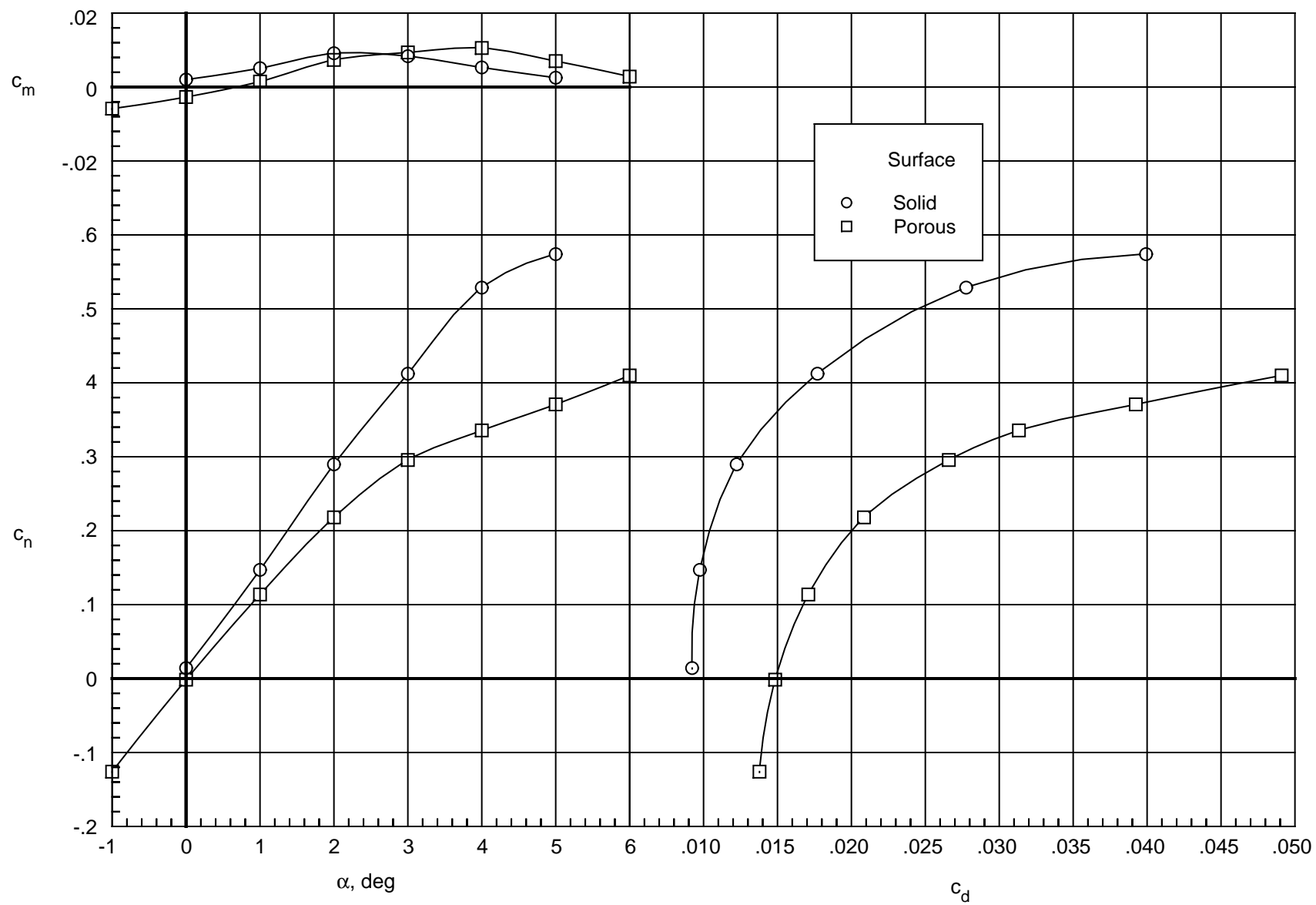
Figure 26. Continued.

(c) $M_\infty = 0.65$.
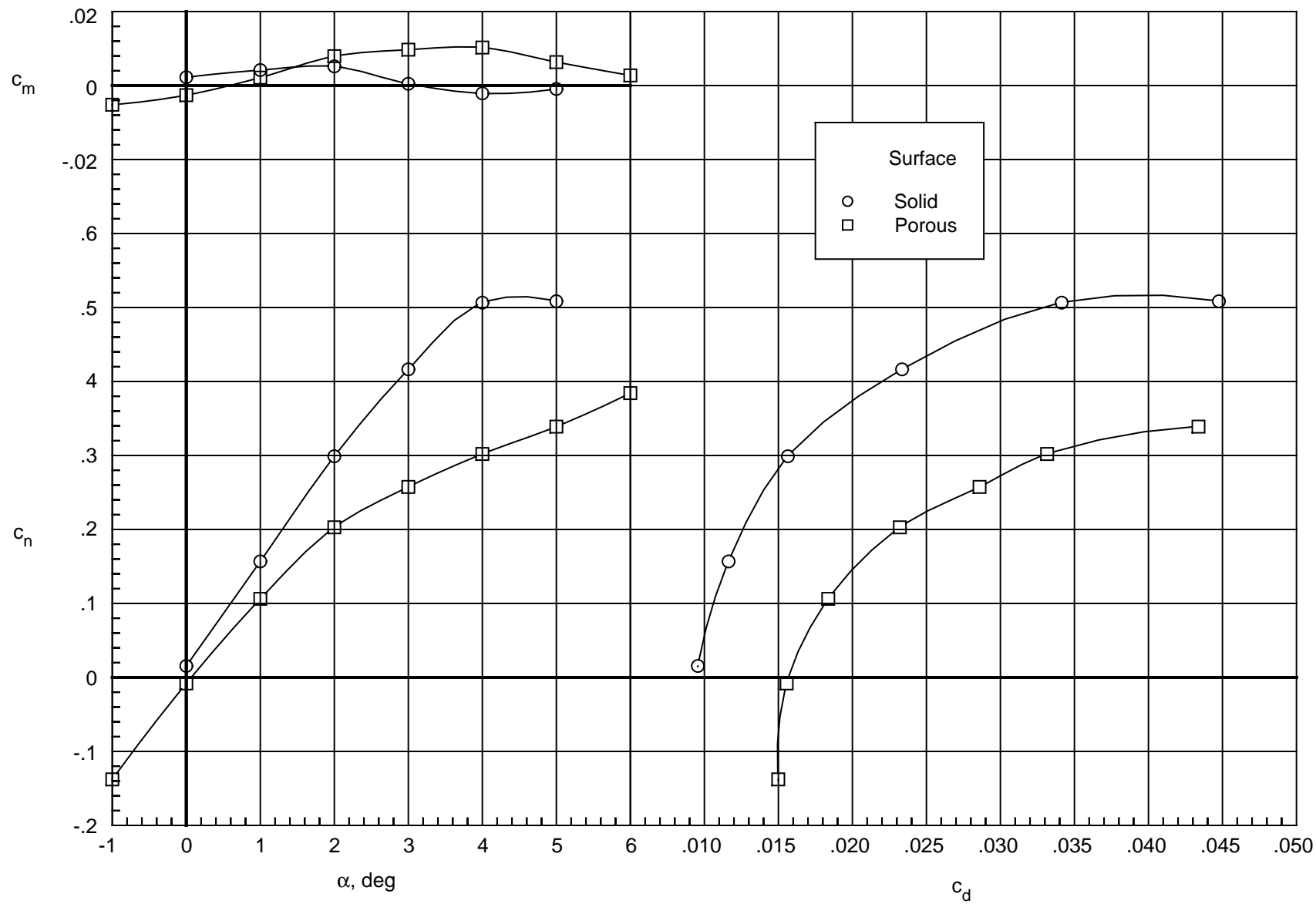
Figure 26. Continued.

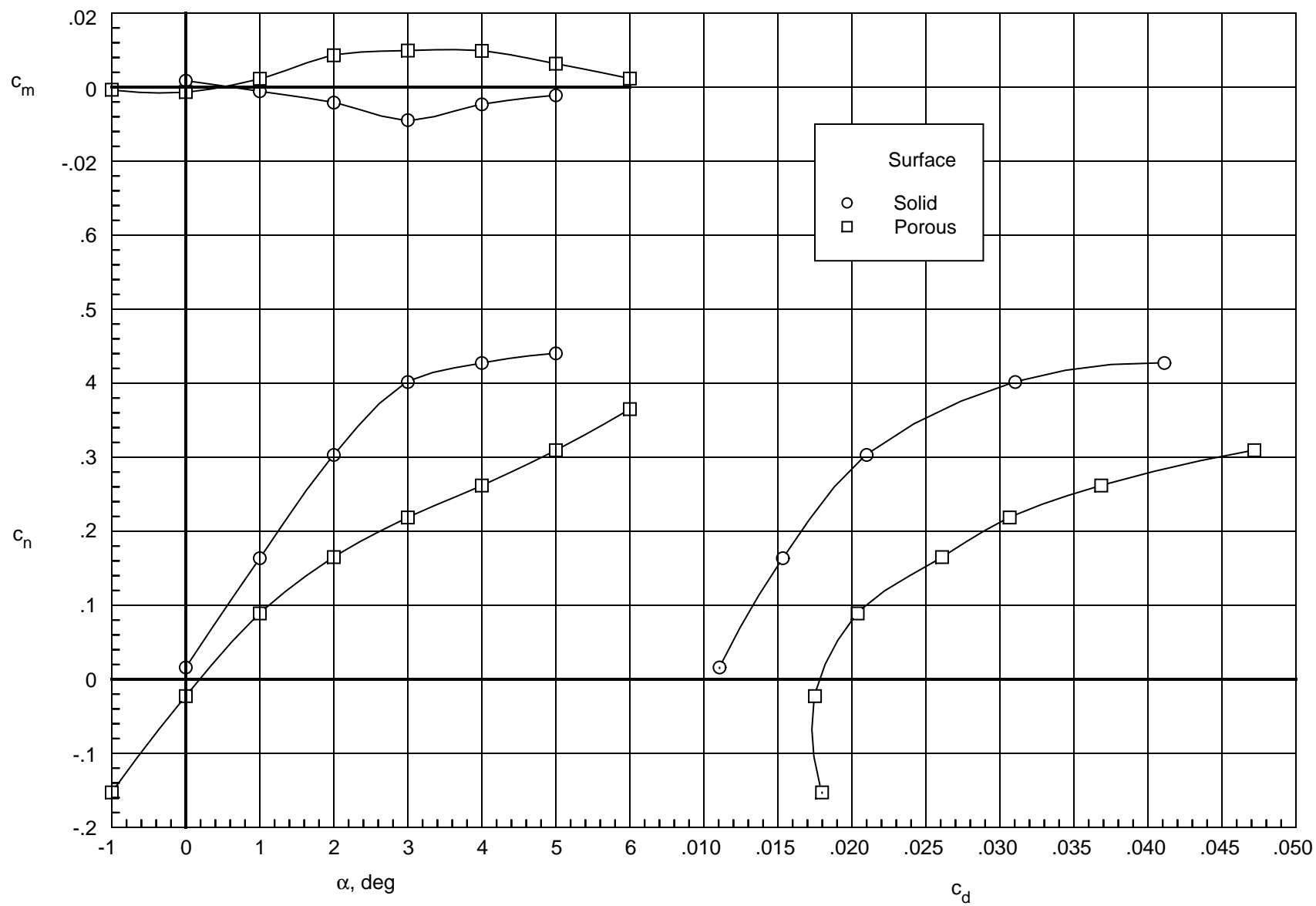(d) $M_\infty = 0.70$.

Figure 26. Continued.

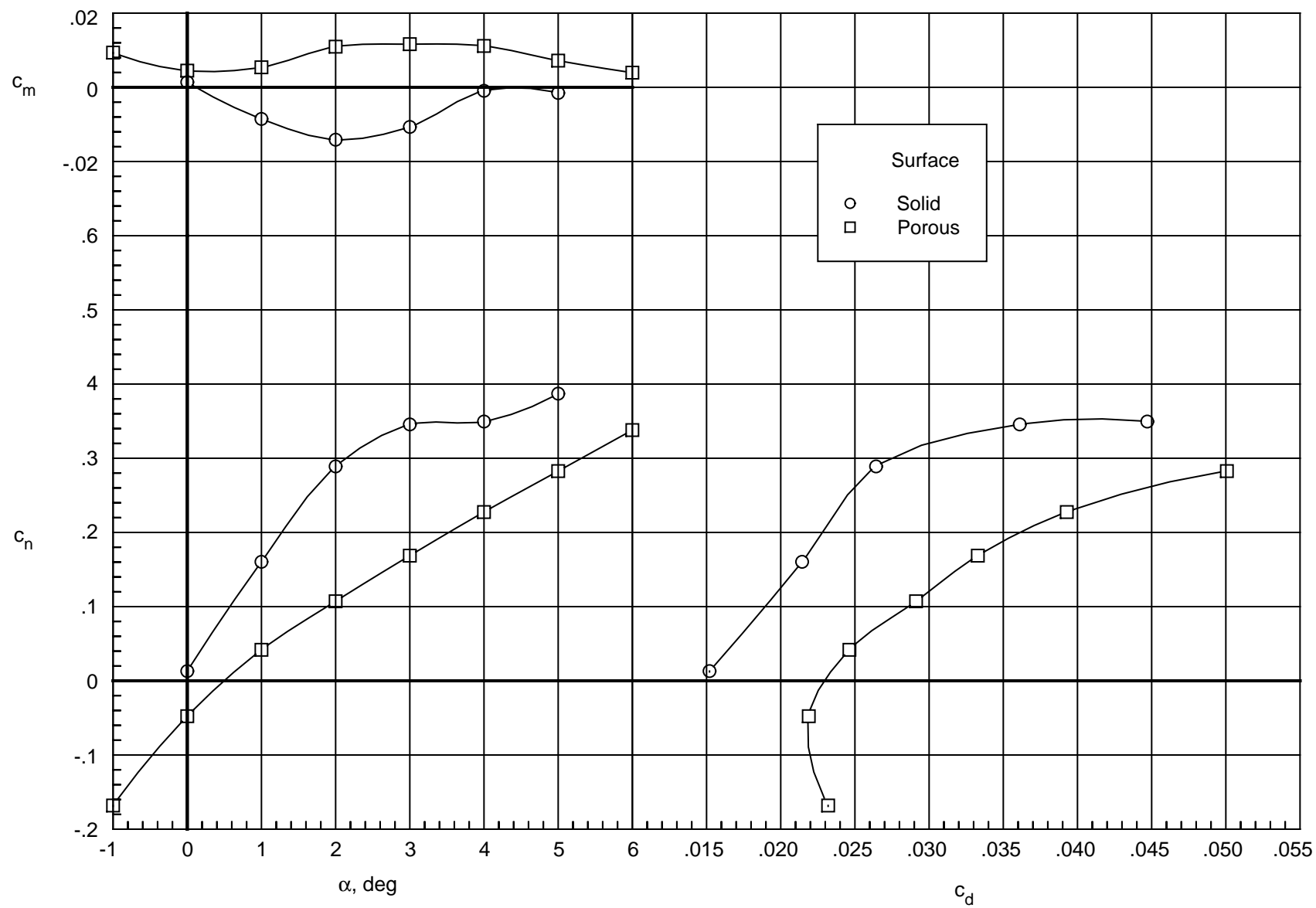(e) $M_\infty = 0.74$.

Figure 26. Continued.

(f) $M_\infty = 0.76$.

Figure 26. Continued.

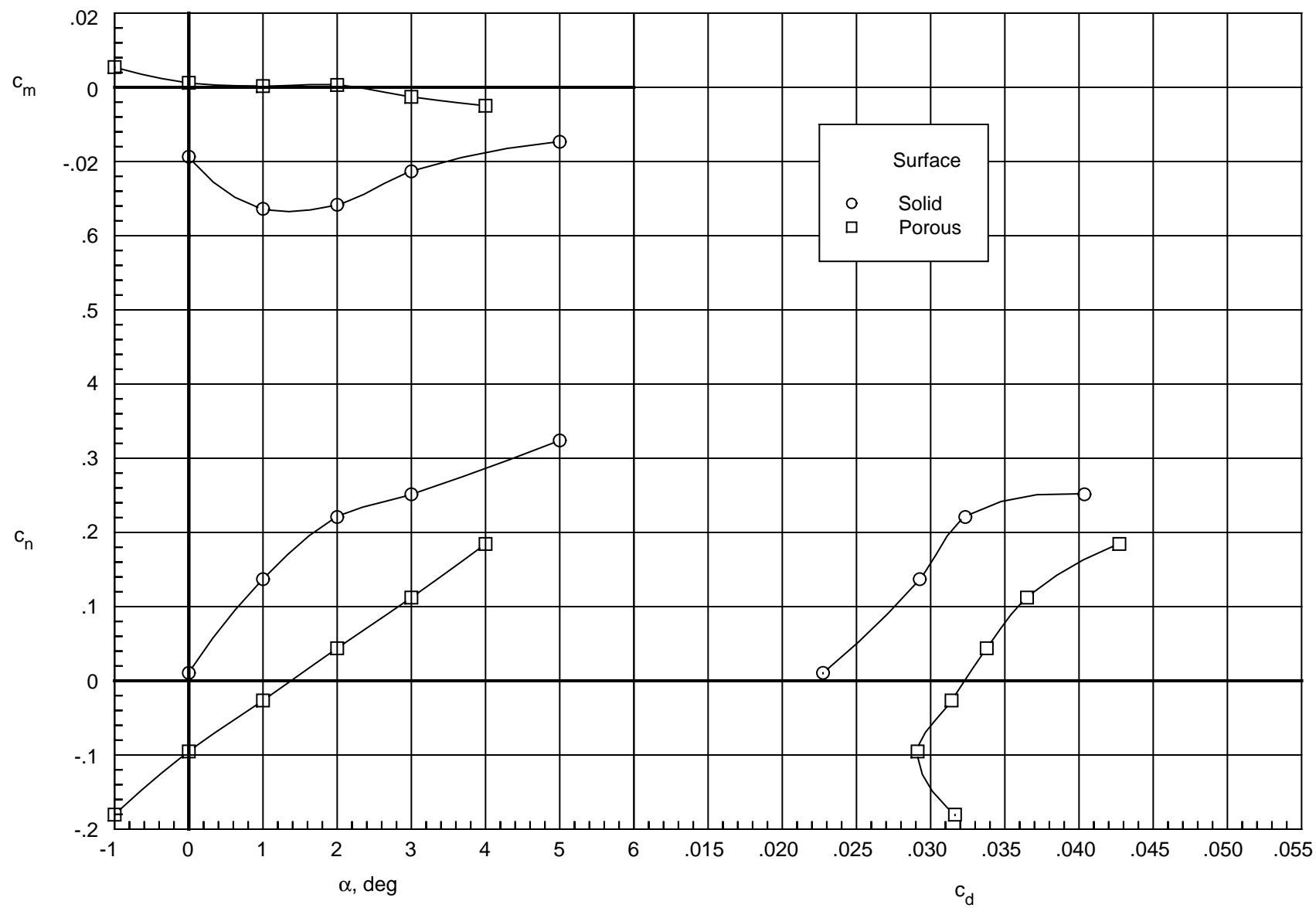(g) $M_\infty = 0.78$.

Figure 26. Continued.

(h) $M_\infty = 0.80$.

Figure 26. Continued.

(i) $M_\infty = 0.82$.

Figure 26. Concluded.
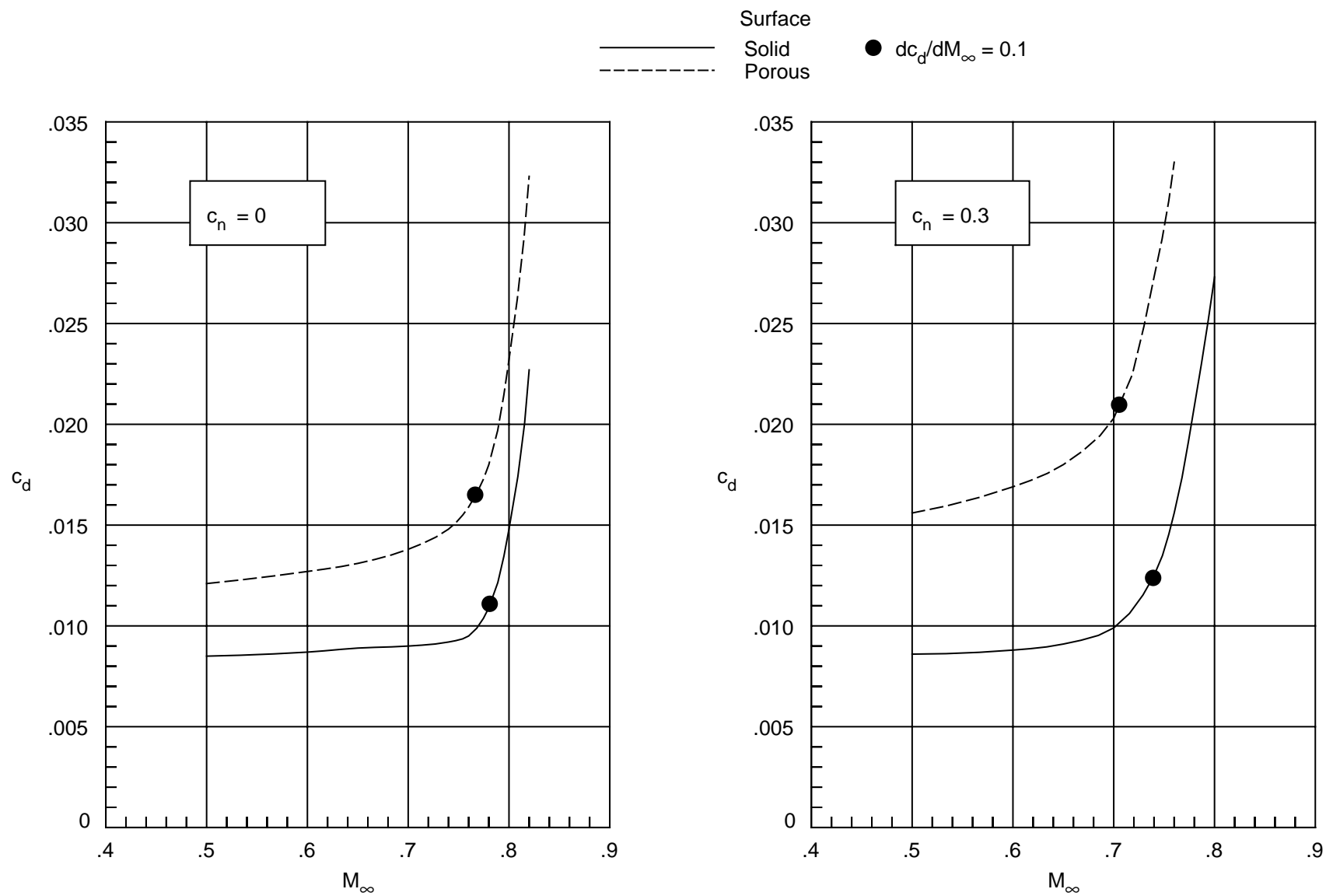
Figure 27. Variation of section drag coefficient with free-stream Mach number. $R_c = 4 \times 10^6$.
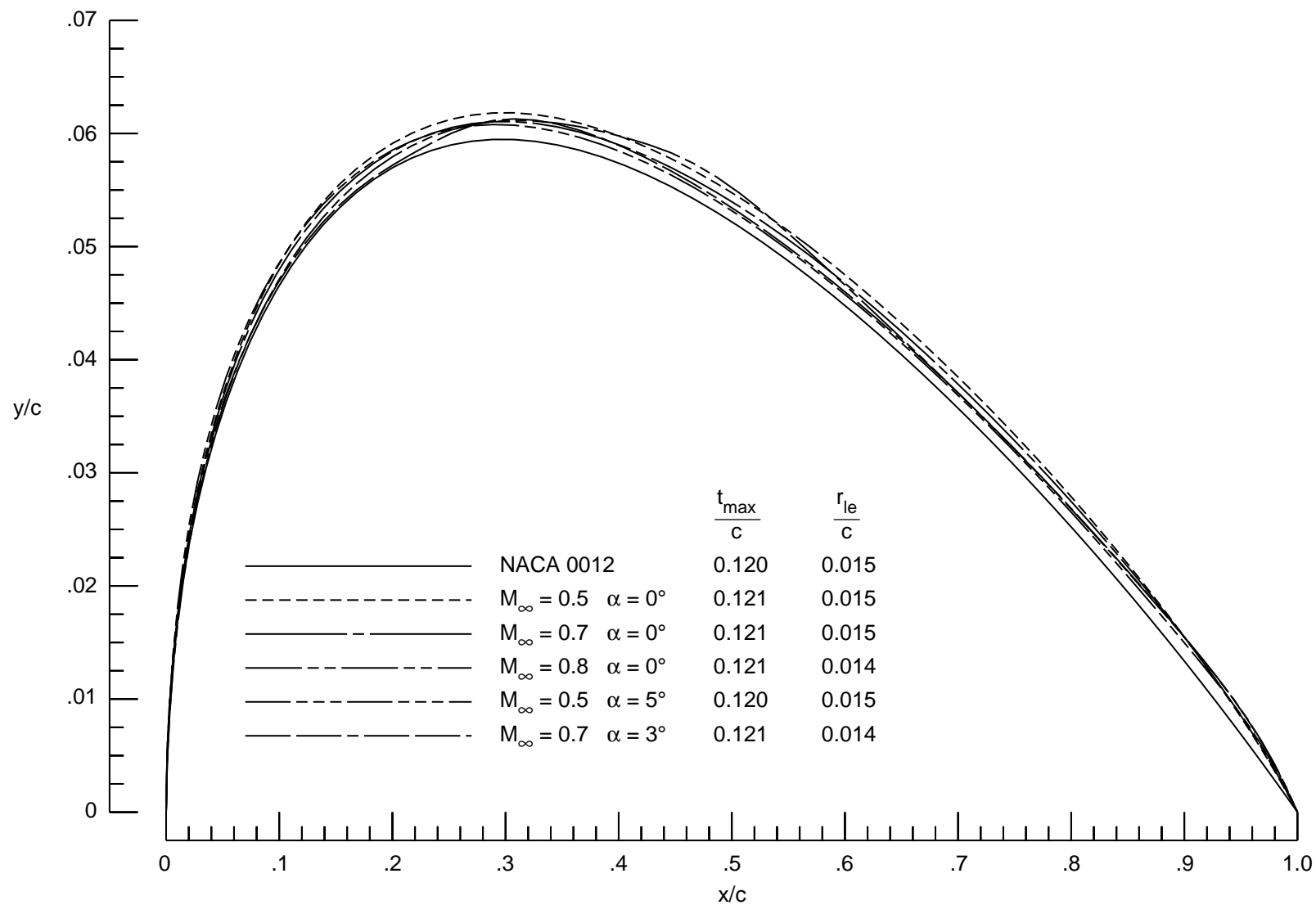
Figure 28. Comparison of baseline NACA 0012 upper surface shape and equivalent solid upper surface shapes obtained from solid surface C_p distributions.

(a) $\alpha = 0°$.

Figure 29. Comparison of baseline NACA 0012 upper surface shape and equivalent solid upper surface airfoils obtained from porous surface C_p distributions at constant α's.

	$\dfrac{t_{max}}{c}$	$\dfrac{r_{le}}{c}$
NACA 0012	0.120	0.015
$M_\infty = 0.50$	0.120	0.011
$M_\infty = 0.70$	0.119	0.011
$M_\infty = 0.74$	0.118	0.011
$M_\infty = 0.76$	0.116	0.010

(b) $\alpha = 2°$.

Figure 29. Concluded.

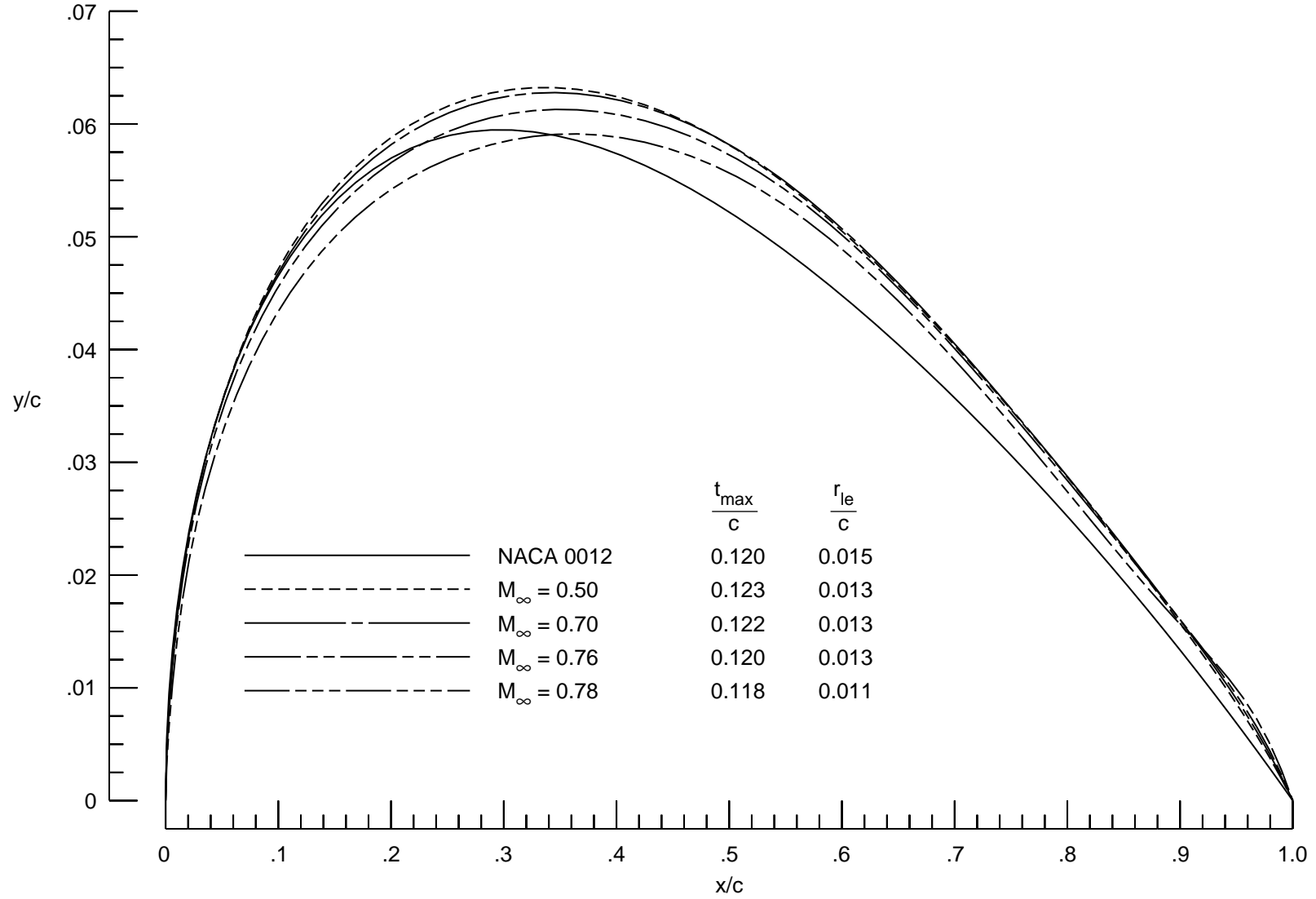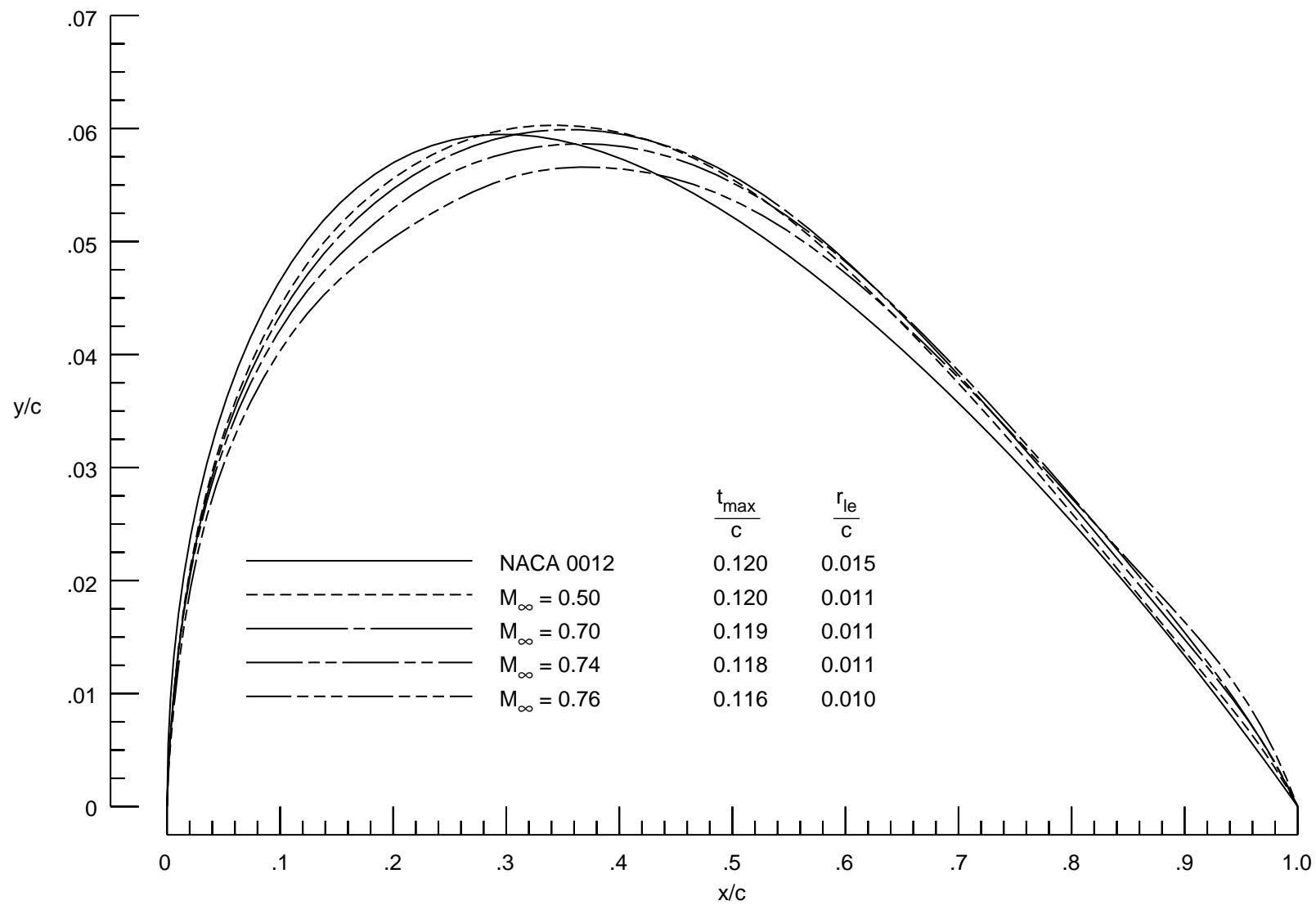|	$\dfrac{t_{max}}{c}$	$\dfrac{r_{le}}{c}$
NACA 0012	0.120	0.015
$\alpha = 0°$	0.123	0.013
$\alpha = 3°$	0.122	0.012
$\alpha = 5°$	0.121	0.011

(a) $M_\infty = 0.50$.

Figure 30. Comparison of baseline NACA 0012 upper surface shape and equivalent solid upper surface shapes obtained from porous surface C_p distributions at constant M_∞'s.
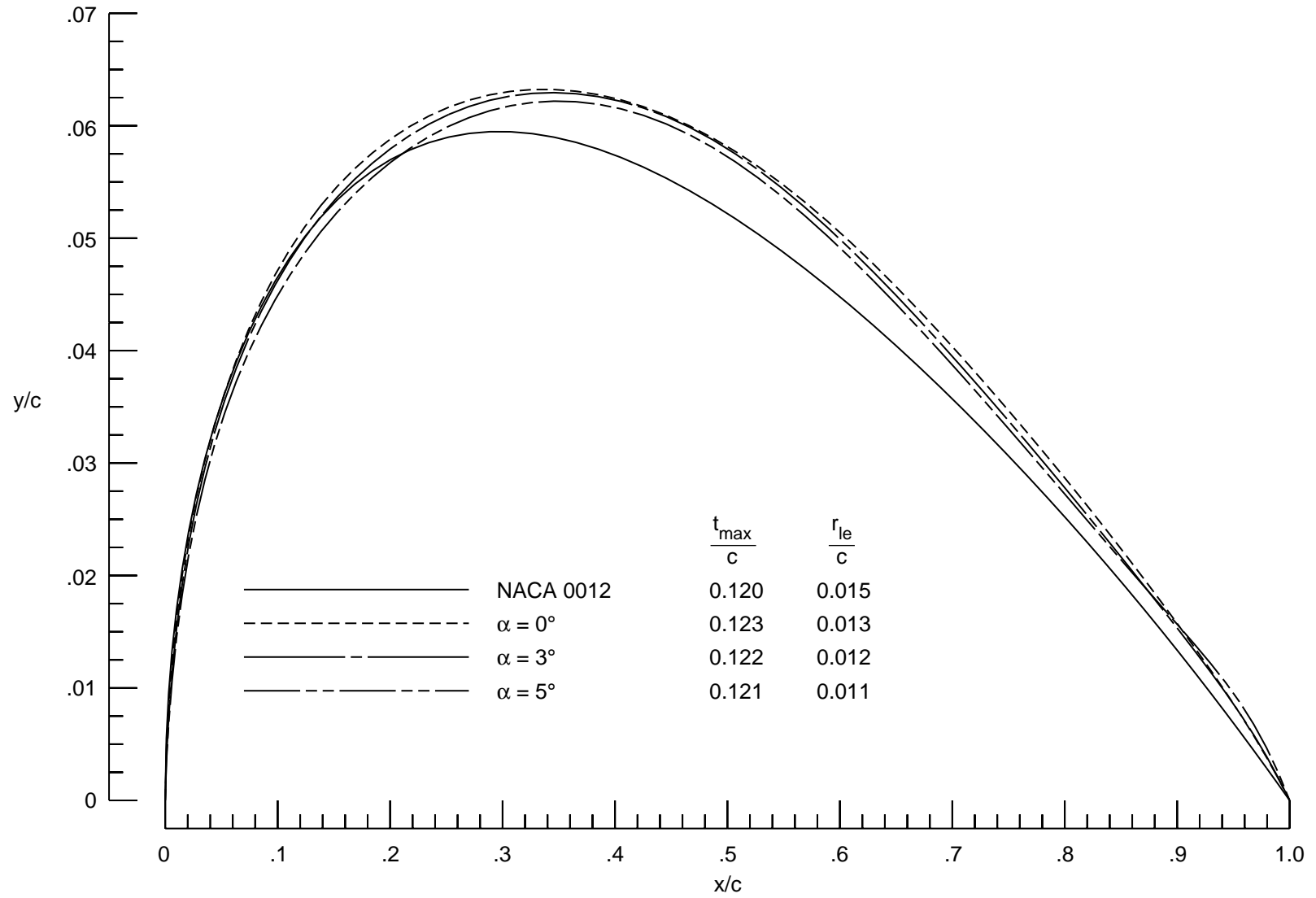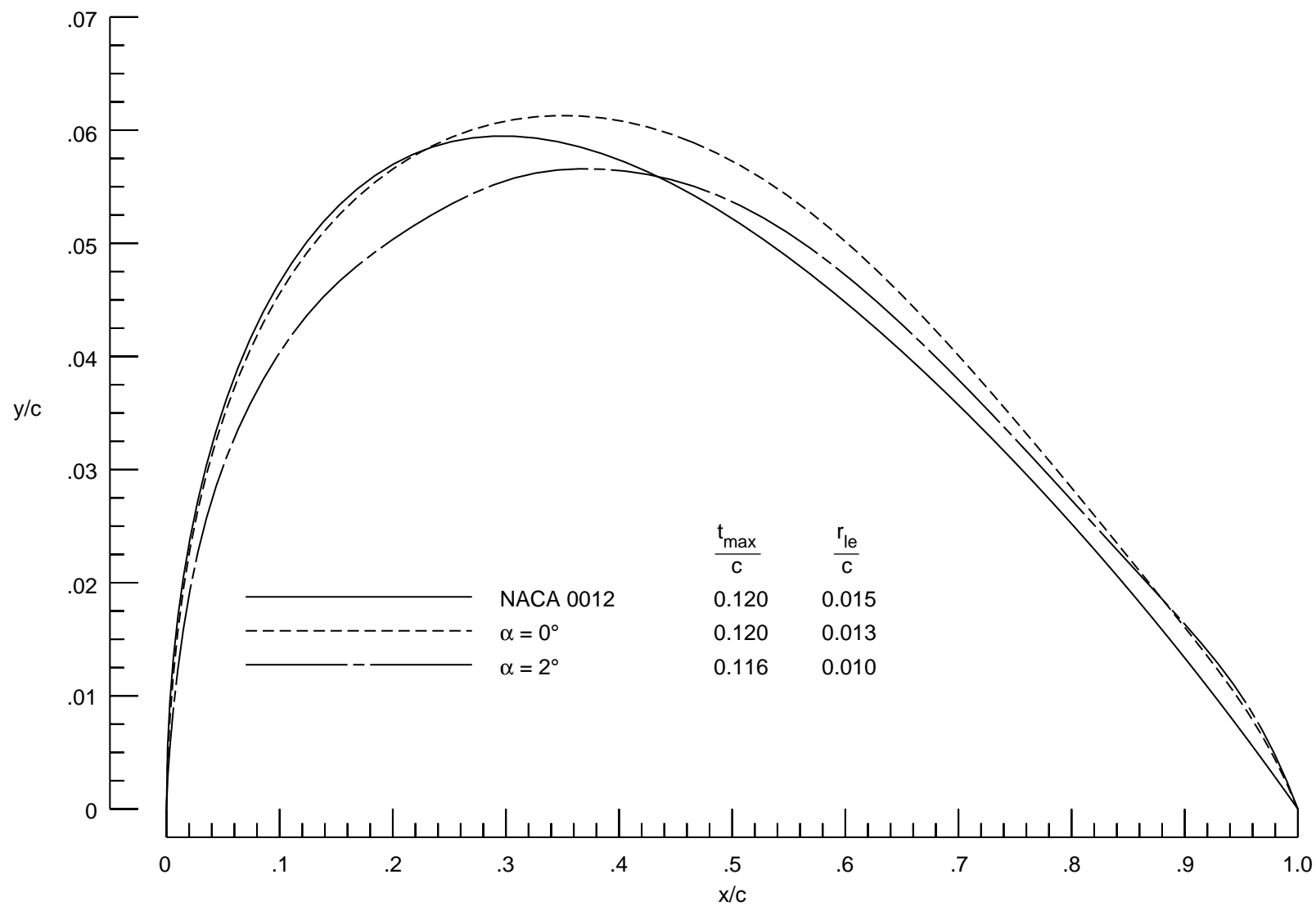
(b) $M_\infty = 0.76$.

Figure 32. Concluded.

REPORT DOCUMENTATION PAGE

Public reporting burden for this collection of information is estimated to average 1 hour per response, including the time for reviewing instructions, searching existing data sources, gathering and maintaining the data needed, and completing and reviewing the collection of information. Send comments regarding this burden estimate or any other aspect of this collection of information, including suggestions for reducing this burden, to Washington Headquarters Services, Directorate for Information Operations and Reports, 1215 Jefferson Davis Highway, Suite 1204, Arlington, VA 22202-4302, and to the Office of Management and Budget, Paperwork Reduction Project (0704-0188), Washington, DC 20503.

1. AGENCY USE ONLY *(Leave blank)*	2. REPORT DATE April 1996	3. REPORT TYPE AND DATES COVERED Technical Paper

4. TITLE AND SUBTITLE
Effect of Full-Chord Porosity on Aerodynamic Characteristics of the NACA 0012 Airfoil

5. FUNDING NUMBERS
WU 505-59-10-30

6. AUTHOR(S)
Raymond E. Mineck and Peter M. Hartwich

7. PERFORMING ORGANIZATION NAME(S) AND ADDRESS(ES)
NASA Langley Research Center
Hampton, VA 23681-0001

8. PERFORMING ORGANIZATION REPORT NUMBER
L-17492

9. SPONSORING/MONITORING AGENCY NAME(S) AND ADDRESS(ES)
National Aeronautics and Space Administration
Washington, DC 20546-0001

10. SPONSORING/MONITORING AGENCY REPORT NUMBER
NASA TP-3591

11. SUPPLEMENTARY NOTES
Mineck: Langley Research Center, Hampton, VA; Hartwich: ViGYAN Inc., Hampton, VA.

12a. DISTRIBUTION/AVAILABILITY STATEMENT
Unclassified–Unlimited
Subject Category 02
Availability: NASA CASI (301) 621-0390

12b. DISTRIBUTION CODE

13. ABSTRACT *(Maximum 200 words)*
A test was conducted on a model of the NACA 0012 airfoil section with a solid upper surface or a porous upper surface with a cavity beneath for passive venting. The purposes of the test were to investigate the aerodynamic characteristics of an airfoil with full-chord porosity and to assess the ability of porosity to provide a multipoint or self-adaptive design. The tests were conducted in the Langley 8-Foot Transonic Pressure Tunnel over a Mach number range from 0.50 to 0.82 at chord Reynolds numbers of 2×10^6, 4×10^6, and 6×10^6. The angle of attack was varied from $-1°$ to $6°$. At the lower Mach numbers, porosity leads to a dependence of the drag on the normal force. At subcritical conditions, porosity tends to flatten the pressure distribution, which reduces the suction peak near the leading edge and increases the suction over the middle of the chord. At supercritical conditions, the compression region on the porous upper surface is spread over a longer portion of the chord. In all cases, the pressure coefficient in the cavity beneath the porous surface is fairly constant with a very small increase over the rear portion. For the porous upper surface, the trailing edge pressure coefficients exhibit a creep at the lower section normal force coefficients, which suggests that the boundary layer on the rear portion of the airfoil is significantly thickening with increasing normal force coefficient.

14. SUBJECT TERMS Porous airfoils	15. NUMBER OF PAGES 89
	16. PRICE CODE A05

17. SECURITY CLASSIFICATION OF REPORT Unclassified	18. SECURITY CLASSIFICATION OF THIS PAGE Unclassified	19. SECURITY CLASSIFICATION OF ABSTRACT Unclassified	20. LIMITATION OF ABSTRACT

NSN 7540-01-280-5500

Standard Form 298 (Rev. 2-89)
Prescribed by ANSI Std. Z39-18
298-102